Performance Studies of the HERA-B Muon Detector and Pretrigger Systems

Masterarbeit
zur Erlangung des akademischen Grades
Master of Science in Physics
(M.Sc.)

dem Fachbereich Physik der
Universität Siegen

vorgelegt von
Valentin Sipică

Juni 2004

Abstract

In this Master thesis, performance studies of the muon subdetector and pretrigger systems are performed for the data recorded in the 2002/2003 data taking period of the HERA-B experiment.
The quality of the muon detector data is checked for all runs accepted for physics analysis. The study consisted of several steps in which the amount of bad readout channels and their influence on data analysis have been investigated. By studying hit distributions in all muon layers, the number of "hot" channels is determined. A simulation is employed for checking the influence of "hot" channels on the quality and quantity of reconstructed muon tracks. This influence is shown to be marginal for the observed rate of "hot" channels in the detector.
In a second study, the efficiency of the muon pretrigger is also investigated. Real pretrigger messages are compared with messages produced in a software simulation which reproduces the behavior of the hardware system. Efficiencies of single channels are computed, as well as average values. Possible sources of inefficiencies are investigated, and it is demonstrated that low efficiency optical links inside the system are the main sources of inefficiencies. Overall, the mean efficiency is larger than 0.975, and over 65.2% of all channels included in the analysis have an efficiency larger than 0.999.

Contents

Chapter 1

Scope of this Thesis

1.1 Introduction

Since the discovery of the electron, towards the end of the 19th century, the field of particle physics has constantly evolved. New particles have been discovered, mainly in experiments studying highly energetic cosmic rays. Later, in the 2nd half of the 20th century, high energy experiments could be set up by means of accelerators, which provided constant fluxes of particles. The field of high energy physics had thus been born.

The Standard Model was developed in the 1970s, as the fundamental theory on which high energy physics is based. This theory predicts that all matter is formed by elementary particles as the fundamental building blocks. There are two such types of particles, particles with half integer spin, called fermions, and particles with integer spin, called bosons.

There are two types of fermions, the leptons and the quarks, with their corresponding antiparticles, i.e. particles having the same properties as the fermions, but with opposite charge numbers. They can be seen in Table 1.1. While leptons are found as free particles, quarks exist only in bound states. Two types of particles with quark contents could be detected: mesons, whose physical properties are determined by two valence quarks, and baryons, which contain three quarks determining their properties.

Table 1.1: The elementary fermions: the quarks (in the left half) and the leptons (in the right half), as predicted by the Standard Model of particle physics.

Quarks			Leptons		
Name	Symbol	Charge	Name	Symbol	Charge
up quark	u	$+2/3$	electron	e	-1
down quark	d	$-1/3$	electron neutrino	ν_e	0
charm quark	c	$+2/3$	muon	μ	-1
strange quark	s	$-1/3$	muon neutrino	ν_μ	0
top quark	t	$+2/3$	tau	τ	-1
bottom quark	b	$-1/3$	tau neutrino	ν_τ	0

The Standard Model describes the interactions between particles from the perspective of quantum field theory. The bosons are the particles which mediate the interactions.

The Standard Model consists of two theories. Electroweak theory describes the interactions between charged particles, between leptons or between quarks and leptons. These are mediated by four types of bosons: the massless photon, and the massive Z^0 and $W^{\pm}$ particles. The strong interaction model is used to describe interactions between quarks. Gluons are the field carrier bosons in this case.

Many high energy physics experiments have been deployed for getting experimental evidence of the existence of various particles, and for studying the interactions between them. The HERA-B experiment was initially built to study CP violation in B meson decays. Since the data taking was delayed by numerous challenges, met in building the detector components and the data acquisition system, HERA-B could no longer compete in the field of study of CP violation. However, the excellent detecting capabilities of HERA-B opened new areas of research in the field of heavy flavor meson production, mainly studying mesons containing b quarks and $c\overline{c}$ bound states.

Two major channels for the decay of J/ψ mesons ($c\overline{c}$ bound states) are represented by the di-electron and the di-muon channels, each with a branching ratio of about 5.9%. Therefore a di-lepton (di-electron or di-muon) is an important signature for detecting a J/ψ candidate. To follow this line of study, HERA-B has developed a very sophisticated multi-level trigger system for selecting J/ψ candidates, which decay into the above mentioned channels.

The muon subdetector plays an important role for selecting di-muon events. Hits in individual layers of the muon subdetector are used to start the trigger chain, and also for the reconstruction of events. The muon pretrigger, a hardware system which belongs to the first level in the trigger chain, uses muon hits to compute track seeds, which are then processed by the higher level triggers.

1.2 Thesis Guide

Due to the important roles of the muon detector and the muon pretrigger in the trigger chain of HERA-B, knowledge of the performances of these systems is very important for the data analysis. The aim of this thesis is to study the overall performances of these systems, and also to identify components which showed a defective behavior.

The HERA-B experiment is presented in Chapter 2, focussing on explaining the purpose of the experiment, as well as giving a detailed description of the detector components, and of the data acquisition system. The muon subdetector system and the trigger chain are presented in detail.

In Chapter 3, a presentation of the muon pretrigger system is given. Its hardware components are described, as well as their role in the entire system.

The methods used for determining the quality of data recorded in the muon system are described in Chapter 4. For this study, the distribution of hits in the muon subdetector are analyzed, isolating components which are a possible cause of errors. Then the influence of these components on the physics analysis of the muon data is determined.

Chapter 5 is reserved for a study of the pretrigger system efficiency. Several methods of computing the efficiency are presented. The obtained results are discussed in detail, pointing out possible causes of errors. The defective components can be therefore isolated, and their influence on the mean efficiency can be determined.

The final conclusions regarding the two independent studies can be found in Chapter 6.

Chapter 2

The HERA-B Experiment

In this chapter the most important aspects of the HERA-B experiment located at DESY, Hamburg, Germany, are described. First the physics goals of the experiment are presented. Then a description of the HERA-B detector components and trigger system is given, as well as of the HERA storage ring. Special emphasis is put on the muon detector, since a data quality check of this component is part of this thesis.

2.1 The Physics Goals of the HERA-B Experiment

The HERA-B experiment was initially designed to study CP violation by investigating the "gold plated" decays of B mesons: $B^0/\overline{B^0} \to J/\psi\, K^0_S$. However, the way B mesons are produced in the HERA-B experiment imposed many challenges in the detecting techniques as well as in the triggering system. These difficult tasks delayed the commissioning of the experiment such that HERA-B could not compete with the other experiments, such as Belle and BABAR. However, the excellent capabilities of the experiment in producing and detecting heavy flavor mesons opened new possibilities in other areas of physics. In the following, a few of these new physics topics will be briefly described.

2.1.1 Heavy Quark Production

Charmonium Production and Nuclear Effects

In HERA-B, charmonium bound states J/ψ and ψ' are detected by investigating characteristic di-leptonic decay signatures. Other charmonium states, such as χ_{c1} and χ_{c2}, are observed due to their radiative decays into $l^+l^-\gamma$ final states.

Due to the different materials used in the target (see also Section 2.3.1), nuclear effects can also be investigated. This is important for other experiments, where quark gluon plasma is produced in heavy ion collisions. One of the signatures for this phenomenon is the J/ψ suppression.

$b\overline{b}$ Production Cross-Section

This is an interesting physics topic, since little is known about the $b\overline{b}$ production cross-section in hadronic collisions. In HERA-B this cross-section is measured analyzing the decay $b\overline{b} \to J/\psi X \to l^+l^- X$.

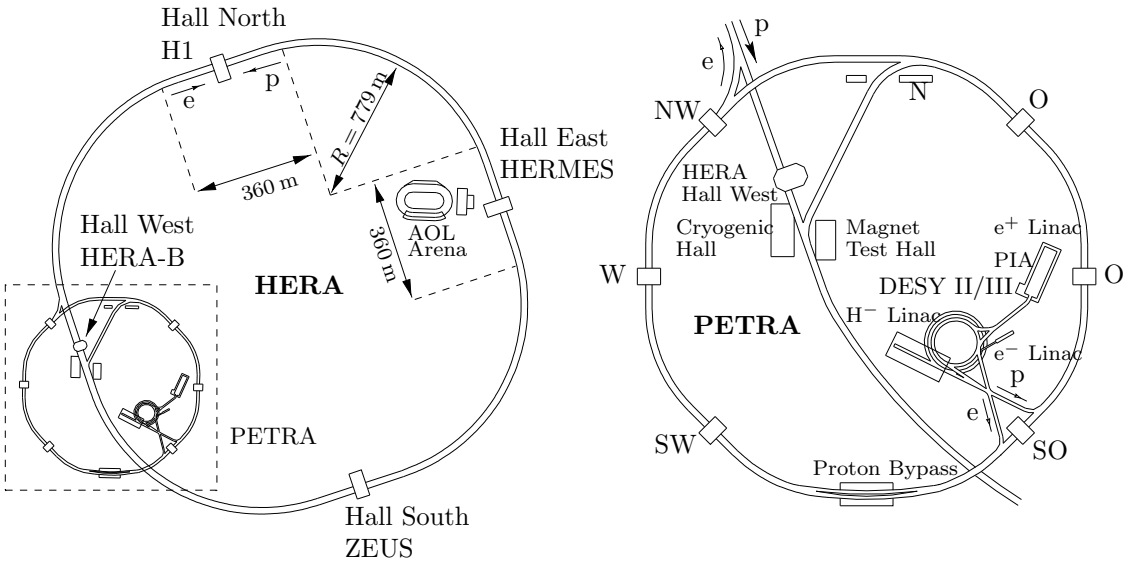

Figure 2.1: View of the HERA storage ring (left) and of the PETRA ring (right) (after [DES00]). In the latter the HERA-B hall (Hall West) can be identified.

2.1.2 QCD Studies

Strangeness Production

Strange flavored mesons are produced in large numbers in proton nucleus interactions. One of them, the K^0_S meson, has a high branching ratio for decays into two pions of opposite charge (approximately 69%). Other strange mesons, which decay into pions and protons are Λ and $\overline{\Lambda}$, $\Lambda(\overline{\Lambda}) \rightarrow p\pi^-(\overline{p}\pi^+)$. Production cross-sections for these particles have been investigated by the HERA-B collaboration.

Another field of study in HERA-B are the polarizations of Λ and $\overline{\Lambda}$ hyperons. The polarization models predict the transverse polarization of the Λ, while there is no polarization for the $\overline{\Lambda}$. Several studies investigating these aspects are performed in HERA-B.

2.2 The HERA Storage Ring

The HERA storage ring is located at DESY, Hamburg, Germany. Here protons are accelerated and stored at an energy of 920 GeV. In a second ring, electrons or positrons are accelerated in the opposite direction to an energy of 27.5 GeV. In the following the term "electron" will be used for both electrons and positrons. A schematic view of the layout of the accelerator can be seen in Fig. 2.1.

Electrons and protons are collided at two interaction points, in the H1 and ZEUS experiments, designed to study the proton structure with high energy electron-proton inelastic scattering. In another experiment the electrons are longitudinally polarized and directed onto a gas target. This experiment, HERMES, studies the spin structure of nucleons.

The protons are not injected into HERA as a continuous flux, but in bunches. Taking into account the storage ring circumference of 6335.8 km, there is space for 220 bunches, with 96 ns time intervals between adjacent bunches. Only 180 of the proton bunches are normally filled with protons.

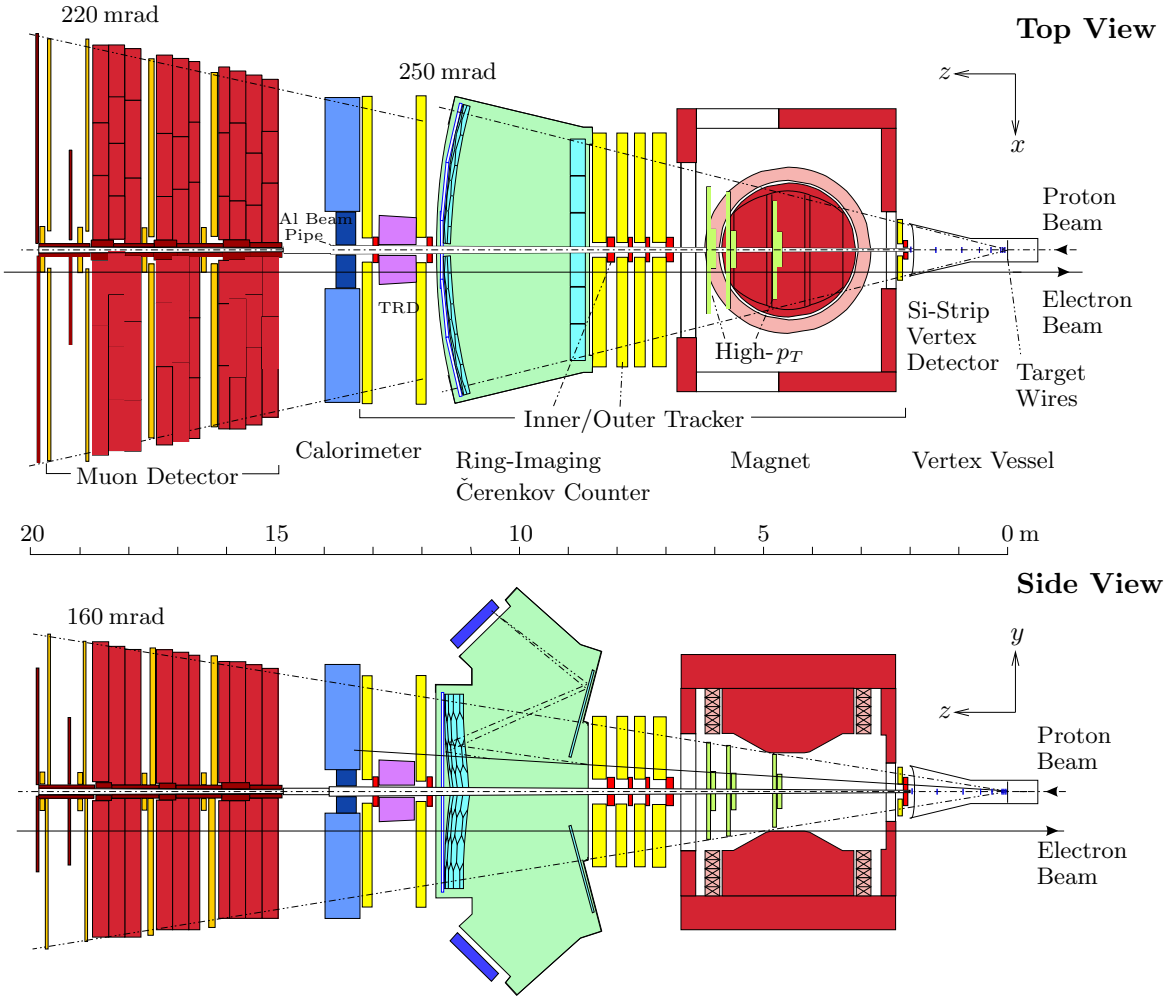

Figure 2.2: Top and side view of the HERA-B detector (after [Spe02]).

2.3 The HERA-B Detector and Trigger

The HERA-B detector is designed as a fixed target spectrometer. A schematic view is presented in Fig. 2.2. The convention, which defines the coordinate system and which will be used throughout this thesis, defines the z axis as the direction of the incoming proton beam. The x axis is the horizontal line, perpendicular to the z axis and having the direction towards the center of the ring, and the y axis is the corresponding vertical line. The angular acceptance of the detector covers the range 15 to 220 mrad in x and 15 to 160 mrad in y.

2.3.1 The Subdetectors

The HERA-B detector consists of several subdetectors designed for particle identification, determining track and vertex parameters and particle energy measurement. The subdetectors can be classified accordingly. The vertex detector system (VDS) is used to identify primary and secondary vertices. The tracking is done by the main tracker which consists of two parts: the outer tracker (OTR) and the inner tracker (ITR). The high-p_T chambers are also used in the track reconstruction. The ring imaging Čerenkov counter (RICH) is used for particle identification. The electromagnetic calorimeter

(ECAL) measures the energy deposited by electrons and photons. The muon detector is used to identify muon tracks.

Target

The HERA-B experiment features a multi-wire target [Ehr00], with which the 920 GeV protons from the HERA storage ring collide. It consists of two stations, each containing four wires placed in the proton beam halo. The dimensions of the wires vary from circular wires of 50 μm diameter to 50 μm $\times$ 500 μm ribbons. The wires of Station I are made of tungsten, titanium, aluminum and carbon, while the wires in Station II are carbon, palladium and titanium wires. The interaction rate, which depends on the atomic number A of the material, can be adjusted by moving each wire independently. Several configurations of wires were used during the 2002/2003 run period. Most of the data were taken with carbon and tungsten targets, while a smaller sample used a titanium target.

Vertex Detector System

The vertex detector system (VDS) in HERA-B [Bau03] is composed of eight superlayers of double-sided silicon strip detectors, perpendicular to the beam axis and integrated into a Roman pot system. The VDS covers an acceptance region from 10 to 250 mrad in the horizontal and vertical planes.

The VDS is designed to allow accurate measurements of tracks produced in the collision of protons with the target nuclei and also tracks of secondary particles produced in the subsequent decays. The track information is used for primary and secondary vertex identification. The vertex resolution in reconstructing $J/\psi \to l^+l^-$ decays corresponds to 30 μm in the transversal and 700 μm in the longitudinal direction. The information from the VDS is also used at the second trigger level to reject track pairs without a common vertex.

Inner Tracker

The inner tracker [Zeu00] covers the high occupancy region close to the proton beam pipe. This corresponds to a radial distance of 6 to 30 cm from the beam pipe, covering the acceptance region of 10 to 100 mrad. It is composed of 7 detector stations placed at different positions along the beam line: one before the magnet, four between the magnet and the RICH and two between the RICH and the ECAL. Each contains several layers of micro-strip gaseous chambers with three stereo orientations, 0° and $\pm$5° relative to the y axis.

The electron amplification is enhanced by using a gas electron multiplier foil situated between the microstrip plane and the drift electrode (MSGC-GEM). The major advantage of introducing this additional amplification step is the protection from discharges in the amplification gas and from short circuits between microstrips. The microstrips have a pitch of 300 μm with anodes of 10 μm width and gap between anode and cathode of 60 μm. This, together with the stereo orientations, results in a resolution of 100 μm in the horizontal plane and 1 mm in the vertical plane. The information from the ITR is used in the track reconstruction.

Outer Tracker

The outer tracker (OTR) [Hoh01, Ste00] is designed to cover the region outside the ITR, i.e. starting as close as 20 cm from the beam axis up to the outer acceptance limit of the experiment. It comprises 7 superlayers disposed along the z axis following a conical layout: one before the magnet, four between the bending magnet and the RICH and two between RICH and ECAL, used by the first level trigger (FLT). The sensitive areas of the superlayers differ in size from $1 \times 1.2\,\mathrm{m}^2$ to $6 \times 4.5\,\mathrm{m}^2$, the largest chambers being most downstream from the interaction point.

Each superlayer contains three stereo layers of honeycomb drift chambers oriented with $0°$ and $\pm 5°$ towards the y axis. This feature enables the OTR to measure space points used for track reconstruction as well as for the FLT. Due to the $1/R$ dependence of the particle flux on the radial distance R from the beam pipe, the cells closer to the beam pipe require a finer granularity. Therefore the diameter of these cells is 5 mm, compared to 10 mm of the outermost cells. The hit resolution resulting in the 5 mm cells is 350 μm. The two superlayers used by the FLT are equipped with double layers of drift chambers, and a logical OR is performed between cells with the same x position. This ensures high efficiency for the FLT.

High-p_T Chambers

The high-p_T chamber system [Bea00] is composed of six chambers grouped in three layers inside the bending magnet. The chambers are composed of gas-pixel chambers in the inner part, with an acceptance in the range of 10 to 58 mrad in the x direction and 10 to 44 mrad in the y direction. The outer part comprises straw-tube chambers with cathode pad readout, covering the region of 38 to 250 mrad in x and 44 to 133 mrad in y.

Initially designed to be used in the pretrigger of hadrons with high transverse momenta, their purpose in the 2002/2003 data taking was to allow the matching of track segments inside and outside the magnet.

Ring-imaging Čerenkov Counter

The ring-imaging Čerenkov counter (RICH) [Ari04] allows hadron identification in the momentum range up to 50 GeV/c, making use of the Čerenkov effect.

Its vessel is filled with perfluorobutane gas (C_4F_{10}), which has the advantages, that it provides both a high refractive index, $n = 1.00137$, and low dispersion of 5% variation in $n - 1$ for photons with wavelengths in the range of 300 nm to 600 nm. At the transition of a particle through the radiator medium, Čerenkov photons are produced, which are focussed through four systems of mirrors (two spherical and two planar) onto two photon detector planes, composed of multi-anode photomultiplier tubes. The projections of these photons on the detector plane have the shape of rings. Since particles of different masses with the same momentum produce rings of different radii, particle species can be identified by measuring the pattern of the rings. The momentum thresholds for producing rings from pions and kaons are 2.7 GeV/c and 9.6 GeV/c. In addition to particle identification, the RICH also provides tracking information from the shape of the rings.

Electromagnetic Calorimeter

The electromagnetic calorimeter (ECAL) [Avo01] allows energy as well as position measurements of electrons and photons.

It is positioned at a distance of about 13.5 m from the target. The ECAL is structured as a matrix of modules formed of alternating layers of scintillator and absorber materials. The light is read out by photomultipliers through wavelength shifter fibers. These modules are grouped in sections with different granularities, following the $1/R$ dependence of the particle flux on the radial distance from the beam pipe. In each section the corresponding modules have different sizes and are made of different materials, but present the same basic structure as described above.
The ECAL is also used for photon/electron identification. In addition it provides fast information to the pretrigger, for finding electron candidates, e.g. of the decay $J/\psi \rightarrow e^+e^-$.

Muon Detector

The muon detector [Eig01] in HERA-B is composed of four superlayers of multiwire proportional counters (MU1–MU4) with interleaving thick absorber material (concrete and iron absorber). There are three layers armored concrete shield and iron absorber, one before MU1, MU2 and MU3. Between MU3 and MU4 there is less absorber (only an iron shield), causing only little absorption and backscattering. The last two superlayers are used in the muon pretrigger. Due to the low energy loss of muons in media, they can penetrate the thick absorber. In this way the hadron/muon separation is ensured, and the muon detector provides a relatively low background from other particles.

Different detector techniques have been chosen according to the radial distance from the beam pipe (which determines the expected hit occupancies in the detectors). In the high occupancy region in the vicinity of the beam pipe, the detector is composed of gas pixel chambers. Each cell has a size of $9 \times 9\,\mathrm{mm}^2$ in MU1–MU3 and of $9.4 \times 9.4\,\mathrm{mm}^2$ in MU4.

In the outer region, the muon superlayers consist of distinct layers of tube chambers. In MU1 and MU2 there are three stereo layers of tube chambers with orientations of $0°$ and $\pm 20°$ with respect to the y axis. In MU3 and MU4 there exists only one vertical layer of such tube chambers. Each tube chamber consists of proportional counters with a cross section of $14 \times 12\,\mathrm{mm}^2$, filled with a fast $Ar/CF_4/CO_2$ - gas mixture. The chambers are composed of two profiles made of 16 cells each (i.e. 16 anode wires), with one of the profiles shifted by half a cell. The tube chambers in MU3 and MU4 provide additional cathode pad readout. They are also called pad chambers. A cross section of the structure can be seen in Fig. 2.3.

For each profile there are two pads. Since a logical OR is performed on the signals coming from opposite pads, the notation "pad" will refer to the combined information of two opposite pads, no matter which of them actually received a hit. The pads are grouped in two columns of 30 pads in MU3 and 29 pads in MU4. Since the pad chambers are vertical, anode wire hits offer information only on the x and z positions of the track. The pads extend the track information by offering also a y position estimate.

The analog signals are processed by ASD-8 cards. Here these signals are amplified, shaped, in order to be digitized, and, in a discriminator step, a threshold is applied to reduce the influence of noise. Therefore only those signals are accepted, which have amplitudes higher than the threshold.

Coincidences of hits in the pad system (hits in both MU3 and MU4) are used by the

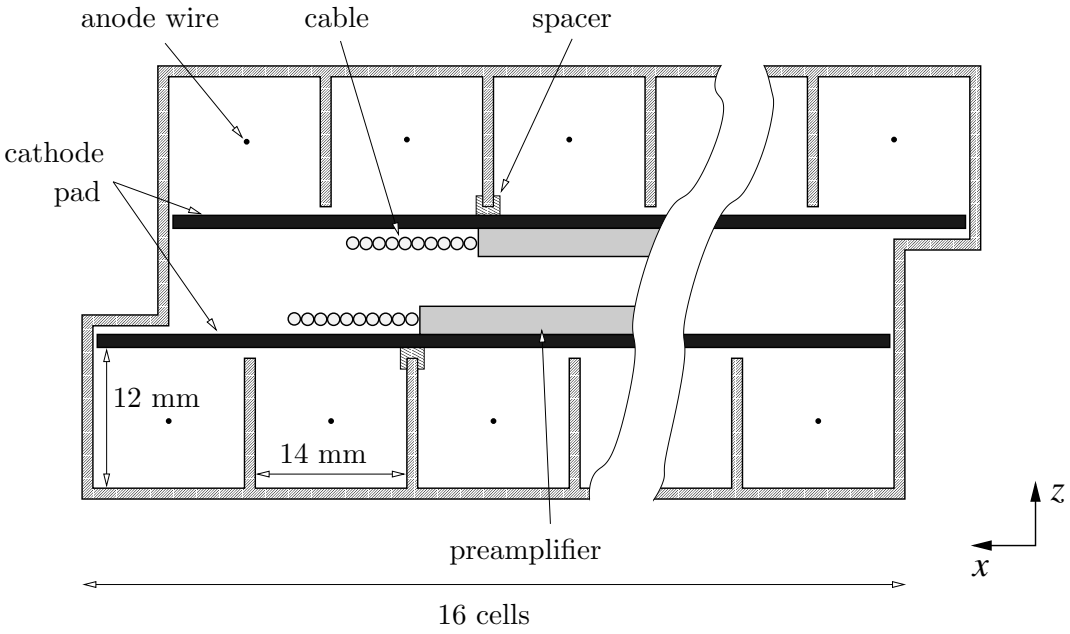

Figure 2.3: Cross section through one of the pad chambers (after [Sch01]). For each profile there are two pads (i.e. for each pad there are eight corresponding cells) which are grouped in two columns stretching on the entire length of the chamber. The tube chambers have a similar layout, the differences being the absence of the cathode pads, as well as the fact that the two profiles are closely joined without any interleaving space.

muon pretrigger to select muon candidates, e.g. for the decay channel $J/\psi \to \mu^+\mu^-$. In the same way coincidences between hits in the pixel cells are used. The muon detector is also used for muon track identification. A reconstructed muon track can be extrapolated to the muon detector and the hits in the tube chambers are compared with the extrapolated hits of the track. Hence the muon likelihood is a measure of how well the hits in the muon superlayers fit the reconstructed track.

The following notations [Har99] will be used throughout this thesis. As mentioned above, the four superlayers are denoted MU1–MU4. In addition, according to the muon tube and pad chamber numbering conventions, the tube chambers in each of the four superlayers of the muon detector are named Mt1, Mt2, Mt3 and Mt4. Here the "t" refers to the tube chamber, and the indices denote the superlayers. However, the chambers in MU3 and MU4 are also denoted as Mp3 and Mp4, the "p" referring to the pad system. While the chambers are the same, the different notations refer to the different detecting techniques and the different readouts, i.e. cathode walls (pads), and anode wires (tubes).

In MU1 and MU2, there are three stereo layers, which are also divided into upper and lower halves of the detector, resulting in six layers. They are denoted as follows: the first two layers (0° orientation with respect to y) are named Mt1.1 (upper) and Mt1.2 (lower), the layers with $-20°$ orientation are denoted Mt1.3 (upper) and Mt1.4 (lower) and the layers with $+20°$ orientation are Mt1.5 (upper) and Mt1.6 (lower). The same notations are used for the layers in MU2, i.e. Mt2.1 to Mt2.6. They can be found in Table 2.1.

In the case of MU3 and MU4, there are only two vertically oriented layers, one in the upper and one in the lower half of the detector. The corresponding notations are

Mt3.1 (upper) and Mt3.2 (lower) for MU3, while Mt4.1 (upper) and Mt4.2 (lower) are used for MU4. The notations Mp3.1 Mp3.2, Mp4.1, Mp4.2 are the equivalent notations for the pad system.

To address a chamber in each of the above mentioned layers, the name has to contain also the index of the chamber. The numbers of tube chambers in each layer vary, and can be found in table 2.1. By convention, the chamber number increases with increasing $+x$ position for all layers in the upper or lower half.

Table 2.1: Conventions used for the numbering of tube chambers in the muon detector.

Layer	orientation	y location	number of chambers in layer
Mt1.1	0°	upper	27
Mt1.2	0°	lower	27
Mt1.3	−20°	upper	28
Mt1.4	−20°	lower	28
Mt1.5	+20°	upper	28
Mt1.6	+20°	lower	28
Mt2.1	0°	upper	29
Mt2.2	0°	lower	29
Mt2.3	−20°	upper	28
Mt2.4	−20°	lower	28
Mt2.5	+20°	upper	28
Mt2.6	+20°	lower	28
Mt3.1	0°	upper	33
Mt3.2	0°	lower	33
Mt4.1	0°	upper	33
Mt4.2	0°	lower	33

2.3.2 The Trigger System

Since the data acquisition system in HERA-B cannot record every single information (more than 600,000 readout channels and more than 5 Tbit/s to be read at each bunch crossing), an elaborate trigger system has been developed to select only those events, which are interesting for the physics analysis.

The trigger is structured in four levels. The low levels use custom-built hardware components to reduce the data flow and the high levels allow software reconstruction on PC farms. A fast pre-selection of events is achieved by two different pretriggers, which use input data only from part of the detector components. They select muon (electron) candidates for the decay $J/\psi \to \mu^+\mu^-(e^+e^-)$, reducing the data rate from the initial rate of approximately 5 MHz to 3 MHz. At the same time they provide "Regions of Interest" (RoIs) as input for the First Level Trigger (FLT). The FLT extrapolates the tracks of the pretrigger candidates and matches them with hits in other subdetectors. In this way it selects only those tracks, which can be reconstructed, reducing the data rate by a factor of 200, the output rate being about 3 KHz. In the next step, the events accepted by the FLT are passed as input to the Second Level Trigger (SLT), which confirms the FLT tracks, extrapolates them to the VDS and applies a vertex cut. In this way the data rate is reduced even more, to approximately 100 Hz. There is also a Third Level

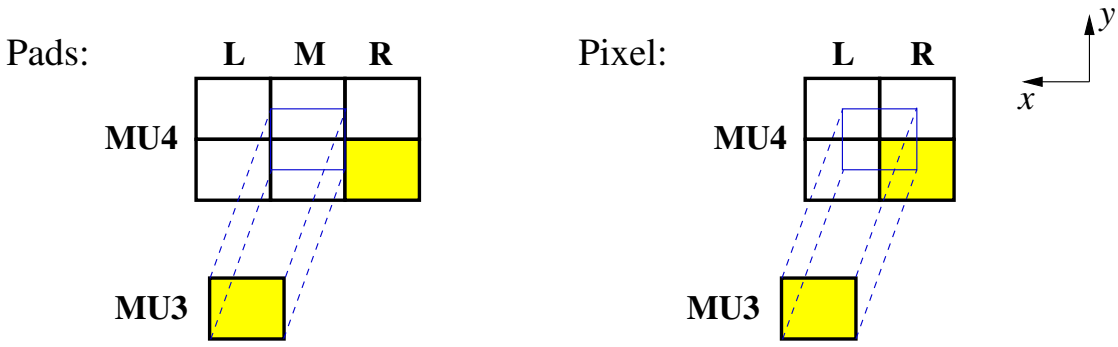

Figure 2.4: The coincidence scheme used in the pad and pixel systems(after [Sch01]). A muon hit in a MU3 pad must match at least one hit in the corresponding MU4 pads.

Trigger (TLT), but it was not used in the 2002/2003 data taking period. The Fourth Level Trigger (4LT) is used for a full online reconstruction of the triggered events and for the monitoring of the data quality.

The Pretriggers

Two types of pretriggers were used during the 2002/2003 HERA-B data taking:

- The ECAL pretrigger [Fla01] searches for electron candidates, e.g. from decays of J/ψ or Υ particles into e^+e^- pairs, or for photon candidates with high transverse energies E_T. It seaches for cells showing local maxima of deposited energy and constructs clusters of 3×3 cells around them. The algorithm computes the total energy deposited in the clusters and the center of gravity in the xy plane. Correcting in addition the energy losses by bremsstrahlung before the magnet, it provides energy and position measurements for electrons which become seeds for higher trigger levels. The ECAL pretrigger messages are interpreted as regions of interest in the last OTR superlayer (TC2) by the FLT and SLT.

- The muon pretrigger [Ada99, Sch00, Böc01] is used as a starting point of the HERA-B trigger chain for events containing J/ψ decays into the di-muon channel. It receives as input muon hits from the pad and pixel systems of both MU3 and MU4. The pretrigger algorithm searches for coincidences between hits in both superlayers as shown in Fig. 2.4.

  In the outer region (i.e. the pad system) a hit in one of the pads of the MU3 is projected on a 3×2 matrix of pads in MU4. These pads are combined in a logical OR. If at least one of the pads in the MU4 matrix contains a hit, a track candidate is generated and its parameters are computed.

  In the inner region, covered by the pixel system, pseudo pads are constructed from 6×4 pixel cells, by performing a logical OR between them. Then a hit in a pseudo pad in MU3 is projected on a 2×2 matrix of pseudo pads in MU4 and the same operations as in the case of the pad system are performed. The track seeds are passed as input to the FLT, which interprets the pretrigger messages as RoIs.

  The muon pretrigger system will be described in more detail in Chapter 3, where its hardware components and their functionalities will be presented.

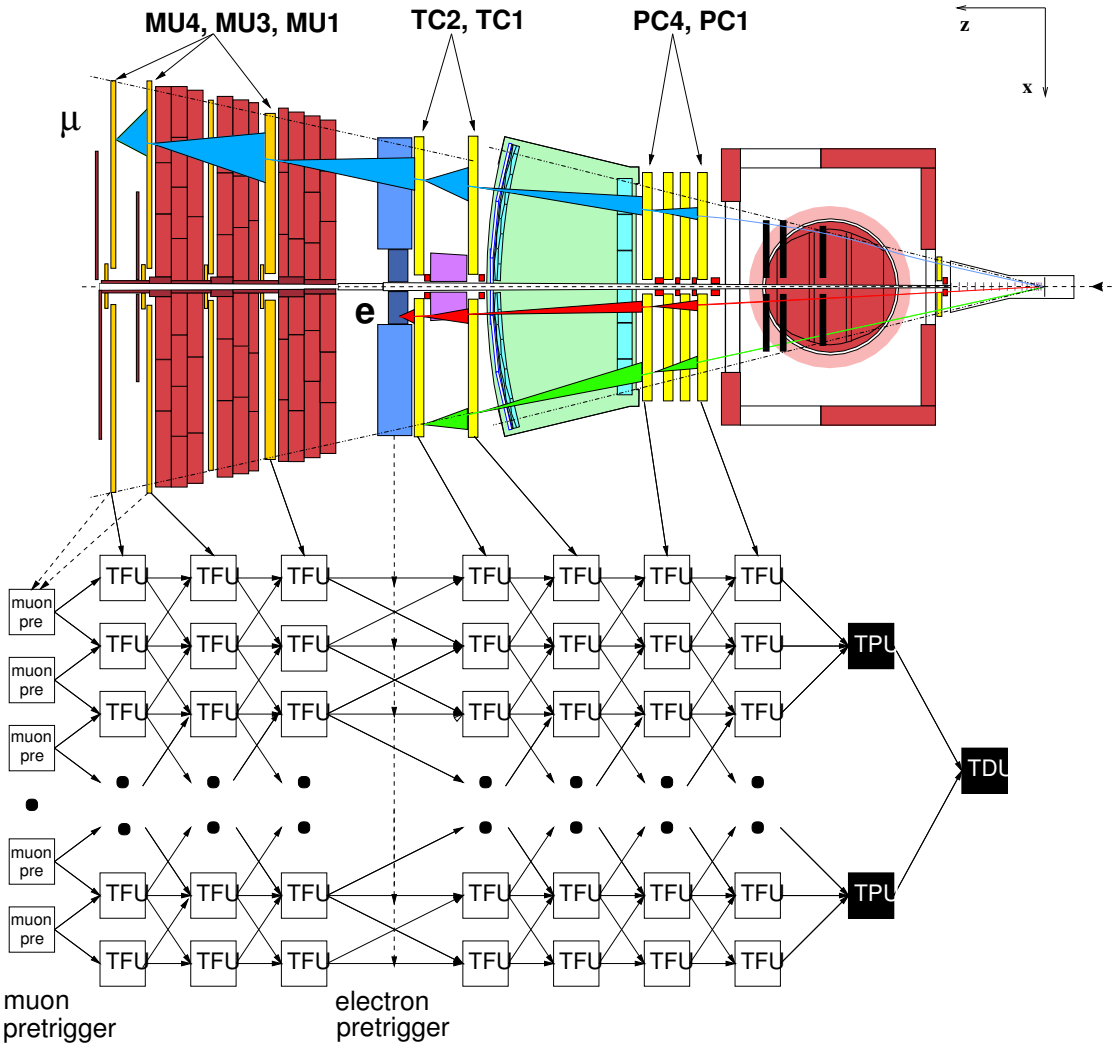

Figure 2.5: Schematic description of the FLT network of modules and working principle (after [Sch01]).

First Level Trigger

The FLT [Bal02] is used for tracking the lepton seeds provided by the pretrigger through the tracking detectors (OTR and ITR). It receives as input the muon and electron track canditates found by the muon and ECAL pretrigger. The pretrigger messages, which contain also position estimates, are interpreted as RoIs in MU4 (for muons) or in TC2 (for electrons). The search for hits is performed in four layers of the main tracker (TC2, TC1, PC4 and PC1) as well as in three muon superlayers (MU4, MU3 and MU1) in the case of muons. A schematic view can be seen in Fig. 2.5.

The FLT uses a network of pipelined specialized hardware boards to perform the online tracking and event selection. There are three types of such boards, each with its own specific function. Track finding units (TFUs) are used in parallel for the extrapolation and reconstruction of tracks.

The FLT algorithm stores the wire information of all superlayers used in the process in the so-called wire memory on TFUs. It starts with a track seed (a hit inside the RoI of the last superlayer) and searches the RoI in the next superlayer for hits. The direction is

always from the last superlayer (MU4 in case of the muon pretrigger and TC2 in case of the electron pretrigger) to the first superlayer of the tracking detector (PC1). The wire memory is used to extrapolate the track to the next superlayer. If a hit is found, it uses this information to recalculate the parameters of the track and to generate a new RoI for the next step. This process is repeated until the track is successfully reconstructed up to PC1. With each iteration the track becomes more accurate, so that the RoI in the next superlayer will be smaller.

Track parameter units (TPUs) are used for determining the track parameters, including momentum at the end of the tracking process. The track momentum is computed, taking into account the bending of the trajectory in the magnet and that the track should originate in the vicinity of the target.

The last of the FLT modules is the trigger decision unit (TDU), where the final trigger decision is taken. In the original design, the event selection is achieved based on invariant mass calculations of $e^+ e^-$ and $\mu^+\mu^-$. In the 2002/2003 data taking, an event was accepted, if at least one track was successfully reconstructed.

Second Level Trigger

The SLT is implemented in software, running on a farm of 240 Linux PCs. Provided that the event is accepted by the FLT, the entire data is written to the Second Level Buffer (SLB). From here it is passed as input to the SLT, together with the pretrigger messages. The SLT algorithm refits the tracks of lepton candidates through the main tracker and extends this procedure through the VDS up to the interaction point. It uses the hit information from the VDS to apply a vertex fit to the tracks and cut on the fit probability, ensuring that the lepton candidates come from a common vertex. For the fitting procedures it uses methods based on the Kalman filter algorithm. More information on Kalman filtering can be found in [Boc00].

Fourth Level Trigger

In the 4LT, the ARTE software [HER03a] (the reconstruction software of the HERA-B experiment) is used on a farm of 100 Linux PCs for a full online reconstruction of events accepted in the previous triggering steps. The ARTE software is also used for the offline analysis. The 4LT also manages the archiving of data to tape and the monitoring of data, for which ROOT files containing data quality information are produced. They will be further used in the study of the muon data quality (see Chapter 4).

Chapter 3

Muon Pretrigger

In this chapter the hardware modules of the muon pretrigger are described, as well as the functionalities of each component. A good understanding of these is important for the determination of the pretrigger efficiency.

The muon pretrigger [Ada99, Sch00, Böc01, Ada01a, Sch01] has the role of finding muon candidates as input for the First Level Trigger (FLT). Hits from the muon superlayers MU3 and MU4 are read out and processed by the pretrigger hardware. A search for hit coincidences between the two superlayers is performed. For each coincidence a message is constructed, which is then passed as input to the FLT. The messages contain various parameters, such as position and slope, which are used in the track reconstruction.

The data rate processed by the muon pretrigger amounts to 17.9 GB/s in the pad system, determined by the number of readout channels and by the readout frequency. Therefore the pretrigger must be fast and highly parallelized to be able to process such a large amount of data.

In the pretrigger, a message is generated only if a coincidence has been found. After this "zero-suppression" step, the entire system of the pretriggers and the FLT are message driven, not driven by a reference clock.

3.1 The Electronics of the Muon Pretrigger

The muon pretrigger hardware implementation involves three main electronics components as can be seen in Fig. 3.1: the pretrigger link board (PLB), the pretrigger coincidence unit (PCU) and the pretrigger message generator (PMG). The PLB receives digitized detector data from the front-end driver (FED) and also from the fast control system (FCS). The data are then serialized and transmitted to the PCU via the 58 m long fibers of the pretrigger optical links (POLs). In the PCU the data are processed, and coincidences are determined. They are transmitted to the PMG, where trigger messages suitable as input for the FLT are created. While for the outer detector area, corresponding to the pad system, the input of the PLB comes from the FED, in case of the inner detector area, i.e. the pixel system, it is produced by the pixel mapping boards (PMBs). The PLBs and PMBs are placed together in the FED crates, below the muon detector. The PCUs and the PMGs are located in the muon pretrigger crates in the electronics trailer.

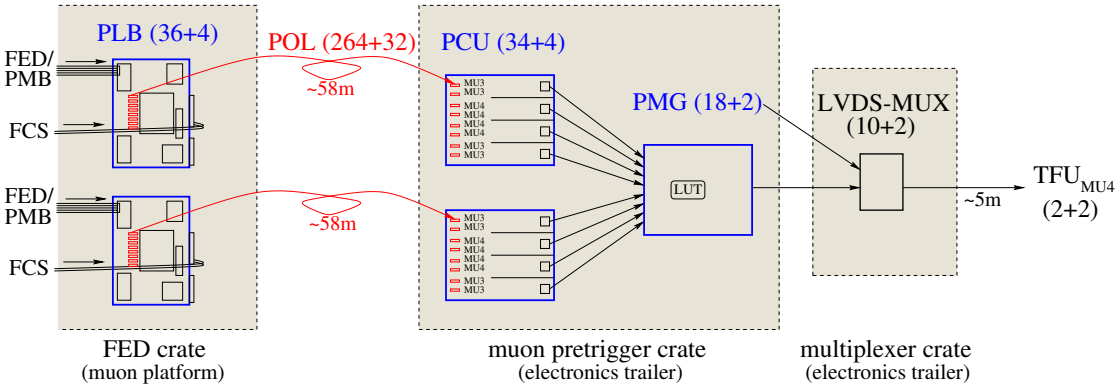

Figure 3.1: The basic hardware components of the muon pretrigger (after [Sch01]). The PLB receives the input data from the FED in the case of the pad system, and from the PMB in case of the pixel system. The number of the electronics boards are given in parentheses.

3.2 The Pretrigger Link Boards

The muon pretrigger receives as input digitized data coming from the muon detector (MU3 and MU4). The pretrigger link boards, which are the first components in the pretrigger chain, are used to prepare the digitized data coming from the muon detector and send it to the PCU. The input data arrives via flat cables from the FED. The boards also receive information from the FCS, i.e. the bunch crossing number BX, which represents an ID stamp for each event, and the bunch crossing clock used as a time reference for synchronizing the data read out from the FED. A schematic view of a PLB board can be seen in Fig. 3.2.

The input channels receive data streams of 32 bits, corresponding to a map of hits from one column, such that each pad in the column has a corresponding bit in the data stream.

The PLB splits the data from each channel in two cycles, such that the effective data rate doubles. One bit is added to each cycle, i.e. the cycle number CN, in order to differentiate the two cycles. Then the eight bits corresponding to the BX number are added, and also four additional external synchronization bits. In the case of MU3, the rest of 15 bits are occupied by half of the bits of the original data format from one channel. Since one channel corresponds to one pad column, each newly formed cycle corresponds to a half column. As the columns of pads in MU4 have only 29 pads, when the splitting in two cycles takes place, bit 15 is copied in both cycles such that they have the same length.

The data of the two columns is then serialized using special modules, and the data stream is sent to the PCUs via POLs, which are realized as piggy back cards mounted on both the PLB and the PCU.

3.3 The Pretrigger Coincidence Units

The pretrigger coincidence unit performs the search for coincidences according to the scheme described in Fig. 2.4. 34 PCUs are used for processing data coming from the pad system. Each board has eight POL receivers, four of them corresponding to MU3 columns and four to MU4 columns. The coincidence scheme requires that hits in one

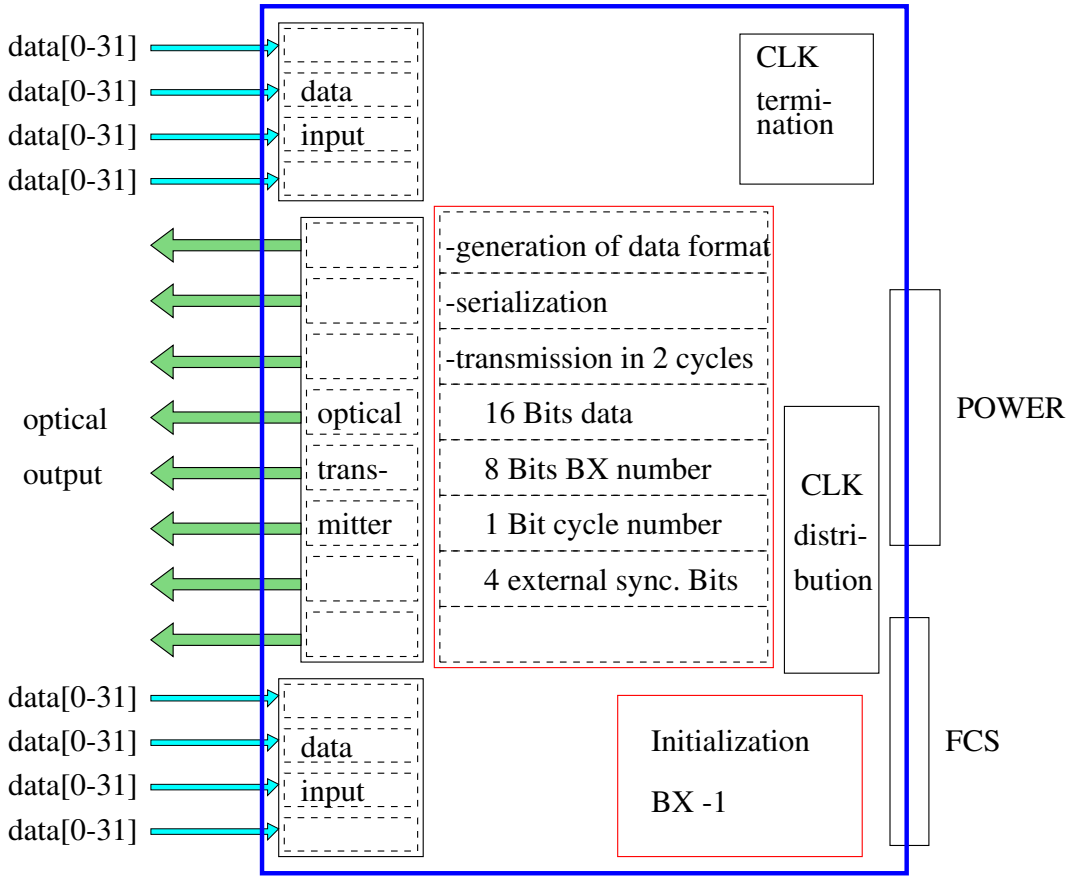

Figure 3.2: Schematic view of the pretrigger link board (after [Sch01]).

MU3 pad column are matched to hits in three corresponding MU4 columns. Therefore, two more MU4 data strings are transmitted to and received from neighboring PCUs via cables. The PCU is divided into three main parts: the data input interface, the complex programmable logic device (CPLD), which performs the search for hit coincidences, and the interface to the PMG.

The data input interface

Eight piggy back cards mounted on the board are used to receive the data transmitted by the POLs and to transform them into electrical signals. Then the data streams are parallelized, using the same modules as for the serialization on the PLBs.

Since the transmission of data through different POLs is not synchronized, and due to the fact that MU3 and the corresponding MU4 data are required to be synchronous when the coincidence search is realized, they are initially written to dual ported random access memories (DPRAM). Short delays in the transmission over the POLs can be overcome by reading the DPRAMs corresponding to MU3 and MU4 at the same time, once that data from all links (both MU3 and MU4) have been received. Since for each MU3 column three MU4 columns are needed, the data from the four MU4 channels are each written to three different DPRAMs, for different MU3 columns. The subsequent connections are schematically shown in Fig. 3.3. Two of the DPRAMs corresponding to MU4 receive data from neighboring PCUs. Moreover, two MU4 streams are written

to neighboring PCUs' DPRAMs. Hence, for each MU3 column a pattern of three MU4 columns is constructed. According to the convention used, this pattern is denoted as LMR, where L denotes the least significant bit, and it will be part of the coincidence data stream.

The data written to each DPRAM corresponds to the data of a cycle transmitted by the PLB (one bit for cycle number CN, 8 bits for the bunch crossing number BX and 16 data bits). In a next step they are further transferred to the input register of the CPLD.

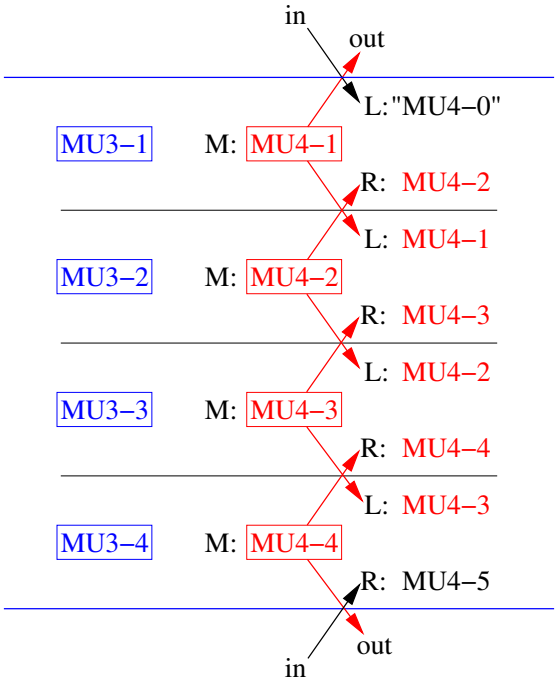

Figure 3.3: Schematic view of the distribution of input data inside the PCU (after [Sch99]).

The complex programmable logic device

The complex programmable logic device has a pipelined architecture, as shown in Fig. 3.4. On every PCU there are four CPLDs, each corresponding to one coincidence channel associated to one MU3 pad column.

The data coming from one MU3 cycle and three MU4 cycles are first written to an input register. In a second step the masking of bad readout channels is realized by applying a logical AND between the data streams and a mask stream. In this way every bit corresponding to pads with a problematic readout is set to "0".

In the next step, pairs of neighboring bits in each MU4 column are logically ORed (i.e. bit0 OR bit1, bit1 OR bit2 and so forth). The resulting patterns replace the original MU4 patterns. Then the coincidences are determined according to the previously described scheme, by applying a logical AND between the MU3 and MU4 data strings. The resulting coincidence string replaces the MU3 string. In the next pipeline stage, the addresses of coincidences are encoded by using look-up tables (LUTs). Then the coincidence string is divided into four substrings, each containing four bits. For each of the substrings, two address strings are formed, either one being composed of four address bits plus one valid bit. The valid bit indicates whether a coincidence is present and the address bits contain the address of the coincidence. The addresses are used to

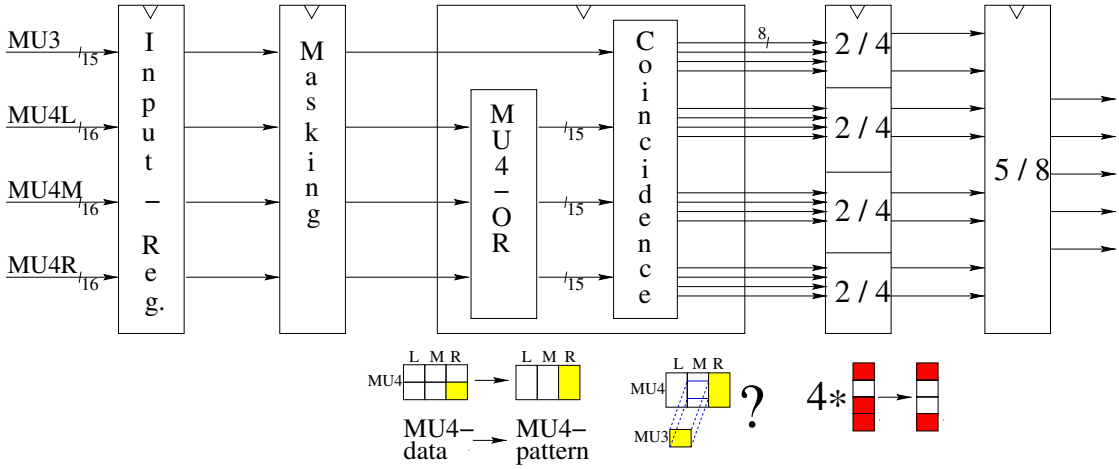

Figure 3.4: Schematic view of the pipeline architecture of the CPLD inside the PCU (after [Sch01]).

determine the three bits in the MU4 pattern, which belong to the MU3 coincidence. Eight output addresses are produced, each containing the four address bits, three bits of the MU4 pattern and one valid bit. This process is also named the "2/4" selection and applied for those coincidences farthest apart. Due to the fact that the CPLD has only 5 output pins, an additional selection has to be performed (called the "5/8" selection) of the coincidences closest to the beam pipe. The address streams are written to five FIFOs together with the BX bits and the CN bit.

The interface to the PMG

Before sending the data streams to the PMG, as mentioned above, they are written to five FIFOs. The first FIFO enables the other four in case it receives data, i.e. data is written to them only if the stream corresponding to the first FIFO represents a valid coincidence. Before the data streams are sent to the PMG, they need first to be serialized. The serialized coincidence data are then transmitted to the PMG. A handshake protocol controls the transfer of each data stream to the PMG.

3.4 The Pretrigger Message Generators

The main purpose of the pretrigger message generator is the translation of coincidence data streams received from the PCU into messages which can be handled by the FLT. These messages have to contain various parameters needed for determining the regions of interest (RoIs) as starting points for the FLT (see also Section 2.3.2).

Each PMG contains several building blocks with different functions, as can be seen in Fig. 3.5. One of these is the interface, which ensures data communication between the PMG and PCUs. Two PCUs, handling eight MU3 columns in total, are connected to one PMG. The handshake protocol controls the data transfer between them, ensuring that only one coincidence channel has access to the data interface at a given moment.

The data stream, which contains eight bits for the BX number, one bit for the cycle number CN, three bits describing the MU4 pattern and four bits determining the MU3 coincidence address, is first split, such that the BX bits are written directly to the output FIFO.

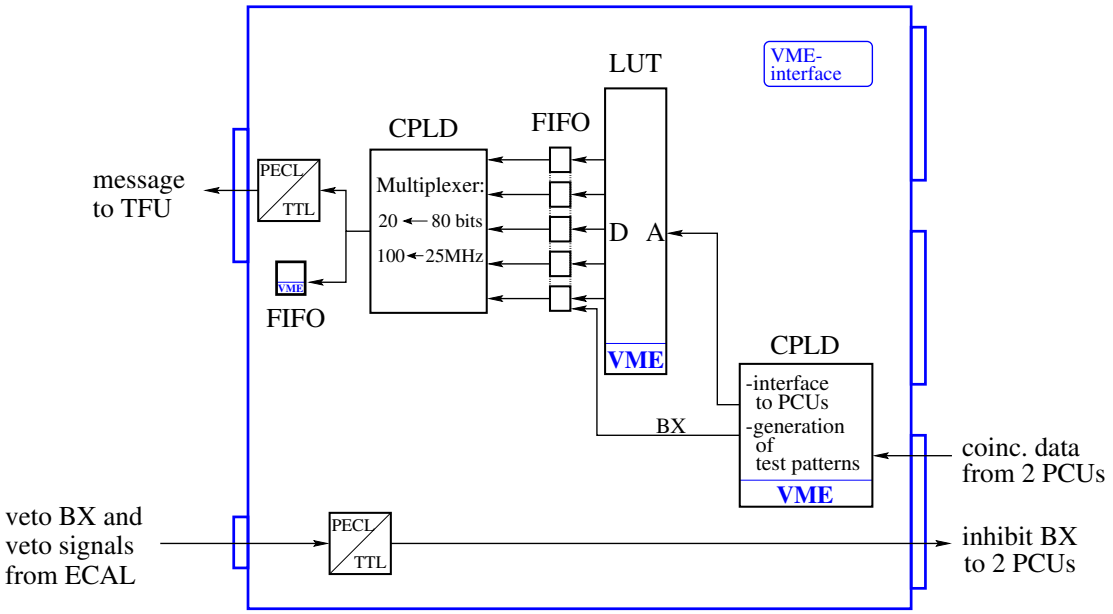

Figure 3.5: Schematic description of the PMG (after [Sch01]).

The remaining eight bits, together with three control bits and five "0" bits added for compatibility with the high-p_T version of the PMG, are sent to a LUT which is loaded into a RAM during the initialization process. The LUT is a table of pre-calculated message parameters. It is used for generating the messages to the FLT. The address streams are employed to retrieve the corresponding values of the parameters which are added to the messages. In total an FLT message contains 80 bits, out of which 57 bits are produced in the LUT, eight bits correspond to the BX number, and the remaining 15 bits are provided for parameters coming from electron pretrigger messages.

The messages obtained from the LUT are first written to the output FIFO, and then split by means of a multiplexer into four messages of 20 bits each, which are sent to the TFU of MU4 in the FLT as well as to the 2nd TDU. The message is also saved in a test FIFO which can store up to 128 messages. A test FIFO exists also in the PCU, and they are both used by the muon pretrigger online software for monitoring the system performance.

Besides the above described function, the PMG also has the purpose of transmitting veto (inhibit) signals to the two corresponding PCUs. These signals are generated by boards belonging to the ECAL or RICH subdetectors, and are meant to suppress events with a too large track multiplicity. They are forwarded to the PCU where they inhibit the transmission of data to the PMG.

Chapter 4

Data Quality Check for the Muon Subdetector

In this chapter a data quality check of the data recorded with the muon system is presented. As mentioned in the previous chapters, the muon subdetector plays an important role in the trigger chain of the HERA-B detector. Hits in the muon pad chambers are used in the muon pretrigger. Together with the electron pretrigger, it is used for initiating the selection of events featuring leptonic decays of J/ψ particles. In the next steps, the first and the second level triggers use the hits recorded in the muon tube chambers for the reconstruction of tracks, starting from the muon subdetector. The muon tracks are then extrapolated using hits in other detector components. Therefore a good knowledge of the quality of the muon data is important.

The main sources of low data quality are the electronics components, which are part of the readout of each channel. Several readout channels have been observed, which show a much higher average number of hits than the expected value. This is mainly solved by masking these "hot" channels. Since the masks are only updated approximately once a month, additional unmasked hot channels remain. A stable method of counting the hot readout channels of the muon subdetector is presented in this chapter, as well as a study of their influence on the physics analysis.

4.1 Analysis Tools and Strategy

The run list, for which this study has been performed, consists of 294 runs, selected among the runs accepted for physics analysis [HER04a, HER04b], which involve data from the muon detector. Data quality information is recorded during the monitoring of each run and stored in ROOT files. They contain a collection of data quality histograms, filled at the end of each run and every 30 minutes throughout the duration of a run. For the analysis only the summary ROOT files, produced at the end of each run, are relevant, since only total occupancies were studied and not the variations within runs. Each file includes histograms containing data quality information. Here only the occupancy plots (i.e. showing the hit occupancies of readout channels) for each layer are relevant. They are recorded both for the tube and the pad chamber readout. The total muon pretrigger coincidence rate distribution has also been studied.

ROOT version 3.03_09 [Bru97] has been used to extract histograms from the data quality ROOT files corresponding to each run. ROOT has also been employed to build an analysis tool to interpret these histograms. There are 16 histograms for the muon

tube chambers (Mt1.1 to Mt1.6, Mt2.1 to Mt2.6, Mt3.1, Mt3.2, Mt4.1 and Mt4.2) that show the hit occupancy of each channel as a function of its x position at the end of a run. There are also two histograms showing the x-y hit distributions in the pad chambers (Mp3 and Mp4), and one histogram for the x-y distribution of the pretrigger rate. The muon layers and chambers have been presented in detail in Section 2.3.1.

To evaluate the influence of bad channels on one of the main physics channels, 20,000 $J/\psi \rightarrow \mu^+\mu^-$ Monte Carlo (MC) events were processed using ARTE-04-01-r4 [HER03a]. For each event, artificial hot channels (i.e. extra hits in both Mt and Mp chambers) have been added before the event was passed through the ARTE track reconstruction chain. The generation of these artificial hot channels uses a tool provided in the ARTE software framework of HERA-B. The exact procedure is described in more detail in Section 4.4. Then the muon likelihood distributions were studied in order to determine the influence on muon multiplicity.

Several runs were discovered, which either did not have a corresponding ROOT file, or the ROOT file was inaccessible. These runs were excluded from the analysis. A list is given in Table 4.1. Here also the runs, which contain only a part of the histograms involving muon information, are shown. These runs were nevertheless passed through the analysis chain, since the histograms which where found could be analyzed.

Table 4.1: Runs with missing or incomplete data quality ROOT files.

Type of problem	List of runs
no DQ ROOT file	19931, 19933, 20040, 20521, 20631, 20636
	20828
incomplete DQ ROOT files	19890, 19897, 19924, 20153, 20158, 20161
	20544, 20757, 20959, 21191, 21217, 21219

4.2 Muon Tube System Analysis

In Fig. 4.1 examples of occupancy plots in the muon tube chambers are depicted. The histograms contain data obtained after hit preparation and masking. To compute the number of bad channels, the distributions were approximated with a Gaussian shape:

$$P(x) = \frac{1}{\sigma\sqrt{2\pi}} e^{-(x-\mu)^2/(2\sigma^2)}, \tag{4.1}$$

and fitted accordingly. Even though the real distributions are not Gaussian, this shape was chosen for simplicity. The deviation from an ideal Gaussian does not influence the result, as spikes of about a factor of 10 higher than the peak value are expected, well separated from the Gaussian fit result. A channel was considered bad, if the bin content was a factor of 4 higher than the value of the fit function in that point. In order to implement a stable method of fitting all the histograms in all runs, in an automatic procedure, the function was centered around 0, by fixing $\mu = 0$. Many spikes in the distributions tend to spoil the fit. By the procedure described above, these cases are kept to a minimum.

The values obtained in this way were plotted against the run number, such that the stability of each chamber could be followed over a range of many runs, as can be seen in Fig. 4.2.

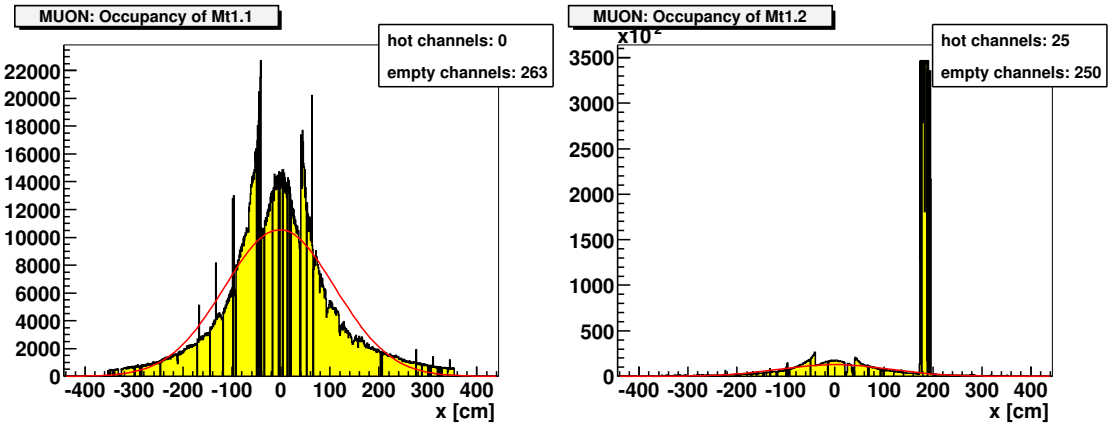

Figure 4.1: Examples of hit occupancy distributions of the muon tube chambers as a function of the x position: in layer Mt1.1, without hot channels (left), in layer Mt1.2 with a typical pattern of hot channels (right). The histograms were recorded for Run 20527. Each bin represents a readout channel. The entire set of histograms for all layers can be seen in Appendix A

.

Table 4.2: Average number of hot channels for every muon tube layer. For each time period between the access dates, the first and the last runs from the run list are given. Also the number of runs inside each time interval is shown.

Layer	19890–20242 (60 runs)	20333–20593 (68 runs)	20612–20757 (17 runs)	20826–21104 (108 runs)	21122–21304 (42 runs)
Mt1.1	2.8 ± 1.0	0.07 ± 0.4	130.6 ± 46.3	0.02 ± 0.1	0.1 ± 0.7
Mt1.2	22.3 ± 8.1	25.3 ± 3.0	28.4 ± 9.4	1.3 ± 4.7	10.6 ± 12.7
Mt1.3	4.6 ± 2.0	3.3 ± 1.0	4.8 ± 1.5	4.0 ± 0.8	5.9 ± 9.0
Mt1.4	2.0 ± 0.8	14.4 ± 4.4	14.7 ± 6.2	2.2 ± 3.2	4.3 ± 10.4
Mt1.5	0.6 ± 1.8	0 ± 0	2.7 ± 3.6	0 ± 0	2.2 ± 9.7
Mt1.6	49.3 ± 17.8	22.7 ± 7.3	47.8 ± 16.0	18.1 ± 4.1	19.3 ± 18.3
Mt2.1	1.0 ± 1.2	0.8 ± 0.6	0.9 ± 0.6	1.1 ± 3.9	3.9 ± 9.9
Mt2.2	1.8 ± 2.7	1.2 ± 0.7	1.5 ± 1.1	1.1 ± 4.1	3.9 ± 9.9
Mt2.3	0.4 ± 1.3	1.0 ± 0.7	1.1 ± 0.5	1.5 ± 3.8	2.7 ± 6.9
Mt2.4	0.2 ± 0.9	0.1 ± 0.6	0.1 ± 0.3	0.8 ± 3.2	4.0 ± 14.3
Mt2.5	0.1 ± 0.6	0.08 ± 0.3	0.8 ± 2.2	0.6 ± 3.6	4.3 ± 12.3
Mt2.6	6.2 ± 25.3	0.2 ± 0.7	0.4 ± 0.8	0.7 ± 3.2	9.4 ± 28.9
Mt3.1	3.4 ± 3.0	3.4 ± 1.6	2.0 ± 1.5	3.1 ± 5.5	7.6 ± 20.1
Mt3.2	2.4 ± 3.5	5.7 ± 2.1	6.7 ± 4.5	6.1 ± 4.4	10.3 ± 18.0
Mt4.1	2.1 ± 1.3	0.9 ± 0.7	0.7 ± 0.7	1.0 ± 1.8	2.3 ± 9.1
Mt4.2	7.4 ± 8.1	14.1 ± 7.1	4.7 ± 7.4	5.7 ± 7.9	6.4 ± 8.1

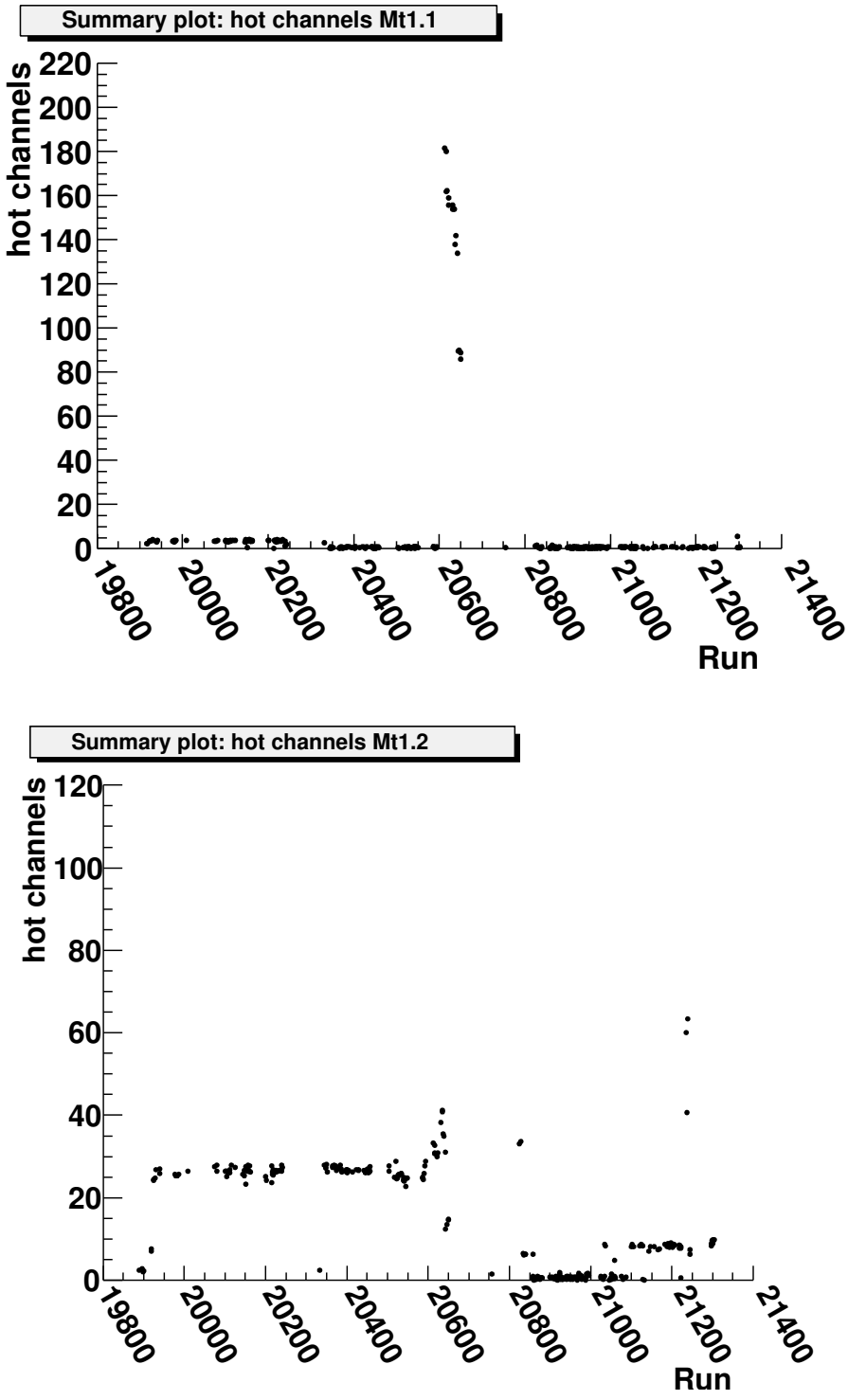

Figure 4.2: Examples for summary plots of the number of hot channels versus the run number: in Mt1.1 (top), and in Mt1.2 (bottom). In the top figure, several runs with a higher number of hot channels than the average can be seen. In the lower plot, the number of hot channels varies for runs belonging to different periods.

Studying the summary plots, it was observed, that the number of hot channels differs over periods of runs. These are the periods between the access dates, during which problematic channels have been repaired. Therefore the entire run range was divided in 5 periods, and for each period the corresponding mean number of hot channels was computed. These values can be found in Table 4.2.

It can be observed that for some periods, the standard deviations from the average values are quite high. This is obvious for periods, where the average number of hot channels has a small value and where the values corresponding to individual runs show a large spread around this value. The average percentage of hot channels generally varies between 0% and 4.5% depending on the period and on the layer. Only for a few runs high numbers of hot channels were observed ($\sim$ 130, which accounts for 11.9% of all readout channels), but only within one period and only for one layer (Mt1.1).

One reason, which caused high numbers of hot channels, is, that the occupancies recorded in several runs were very low due to low statistics, which influenced the quality of the fit. In reality, these values do not correspond to hot channels. Another reason is, that during some of the runs, the ASD-8 readout cards (see Section 2.3.1) changed their thresholds to the maximum value. This caused the occupancy histograms not to be filled in some runs. Because of the fit instability, all channels are then labeled as hot. This was found out by studying the online run logging [HER03b]. All such runs were excluded from determining the average value of hot channels. A list can be found in Table 4.3. In addition, three runs have been discovered, which are FLT efficiency test runs, and have been excluded from the physics run list.

Table 4.3: Runs, which caused problems in the data quality assessment of the tube chamber occupancies.

Type of problem	List of runs
low statistics	20152, 20215, 20350, 20375, 20544, 20862 20866, 20298
wrong thresholds of ASD-8 cards	21130, 21131
FLT eff. runs included in the physics run list	21236, 21237, 21238

4.3 Muon Pad System Analysis

A typical (x, y) hit distribution in the muon pad system can be seen in Fig. 4.3. A fit of the distribution in the 2D histogram is difficult to accomplish, since a stable fit result is hard to achieve for distributions corresponding to different runs and also because a parameterization is difficult to find.

Thus a different method than in the case of 1D histograms was used. This method involved computing the median. The statistical is defined such that half of the elements of a sample are smaller than the value of the median and half are larger. The median gives a robust method for calculating mean values. In order to use this method, the distribution had to be reweighted with a function, that would reflect the dependence of the distribution on the radial distance from the proton beam pipe, R. This dependence

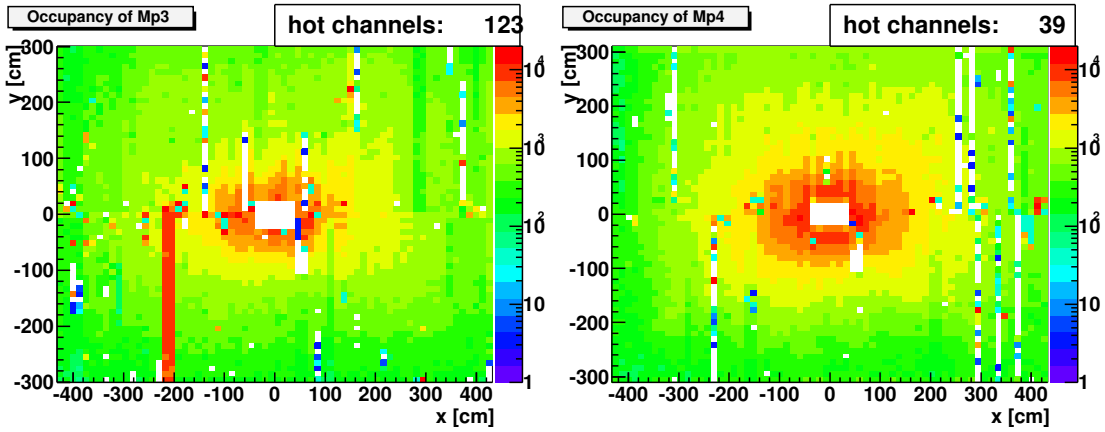

Figure 4.3: Example of hit occupancies in the pad chambers as a function of the x and y position of each readout channel, i.e. of each pad: in Mp3 (left), in Mp4 (right). The plots were recorded for Run 20527

can be parameterized as a function of R^{-a}. By dividing the muon occupancy by such a function, a flat distribution is expected. A value of $a = 1.9$ was used for the reweighting. This value was obtained by analyzing the occupancy distributions of one of the runs, as can be seen in Fig 4.4.

The bins (channels) with zero occupancies (the area corresponding to the proton and electron beams, which is not covered by the detector, as well as the masked channels) had to be disregarded from the computation because they alter the value of the median, and therefore the counting of spikes. Next, a threshold of four times the median was used to select hot channels. These numbers were plotted versus the run numbers, as shown in Fig. 4.5. It can be observed, that, for most of the runs, the maximum number of hot channels is about 100 (for Mp3) and 80 (for Mp4). Compared to the total number of readout channels of 3916 in Mp3 and 3784 in Mp4, this implies, that about 2.5% (for Mp3) and 2% (for Mp4) of all channels are hot.

In addition, a series of runs with two hot columns in the Mp3 occupancy was found, while there is no such pattern in Mp4 (see Fig. 4.3). Then the pretrigger coincidence rates for the same runs were studied (see Section 4.5). Since there is no match of the pattern of hot channels between MU3 and MU4, there is only a small influence on the pretrigger rate, so that the data can be considered as good data. A list of these runs can be found in Table 4.4.

Table 4.4: Runs, which caused problems in the data quality assessment of the pad chamber occupancies.

Type of problem	List of runs
dead quadrants	20980
pattern of hot channels in Mp3	20517, 20526, 20527,20586, 20587, 20588 20591, 20592, 20593, 20612, 20757

There is one run, in which one or two of the four quadrants of the muon pad sys-

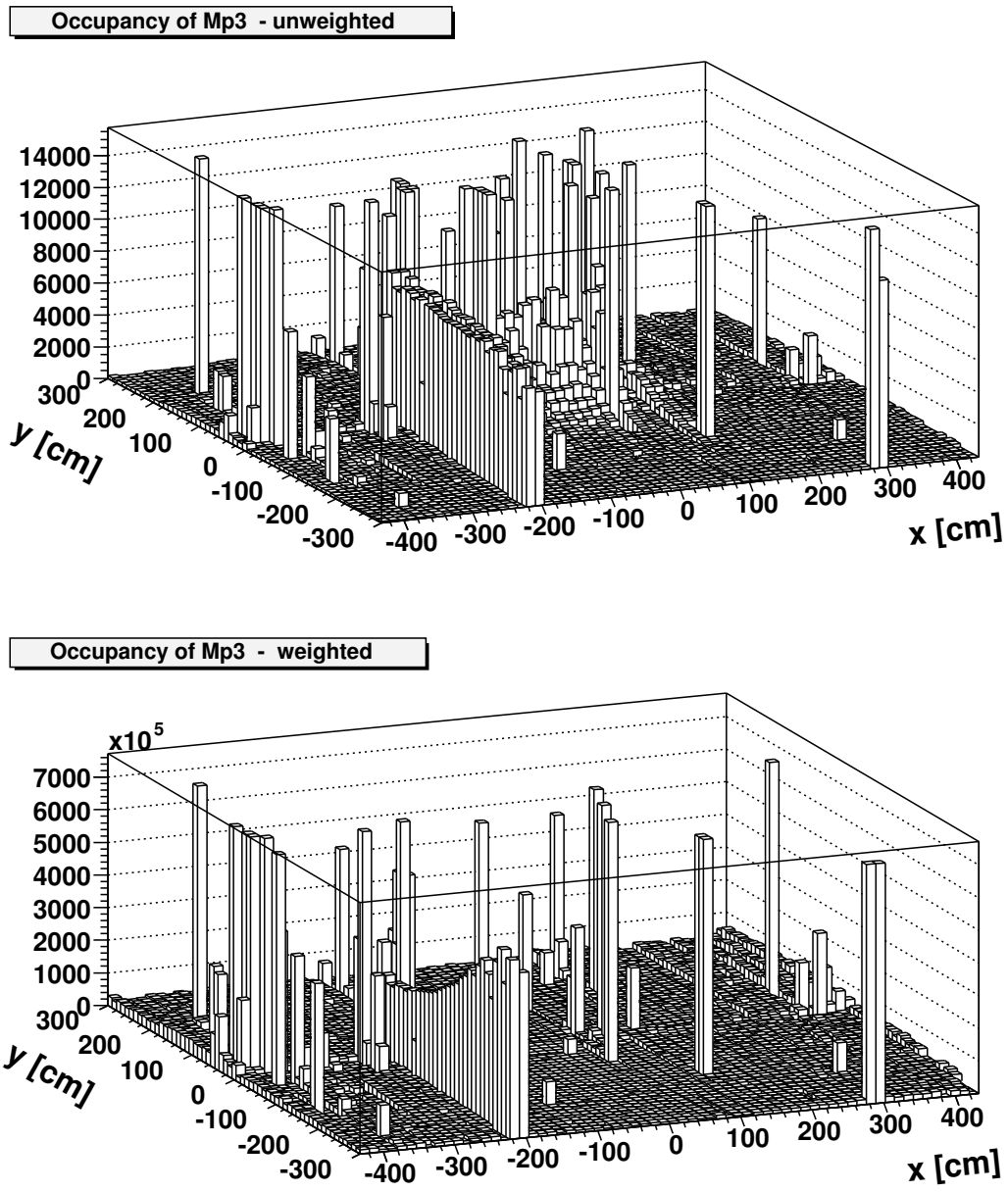

Figure 4.4: Example of weighting the muon pad occupancies. In the top figure the original hit distribution for Run 20527 can be seen. A typical pattern of hot channels can be observed. In the bottom figure, the same distribution after weighting with $R^{-1.9}$ is shown. It can be noticed, that the latter is a flat distribution, but the hot channels from the original distribution are still present.

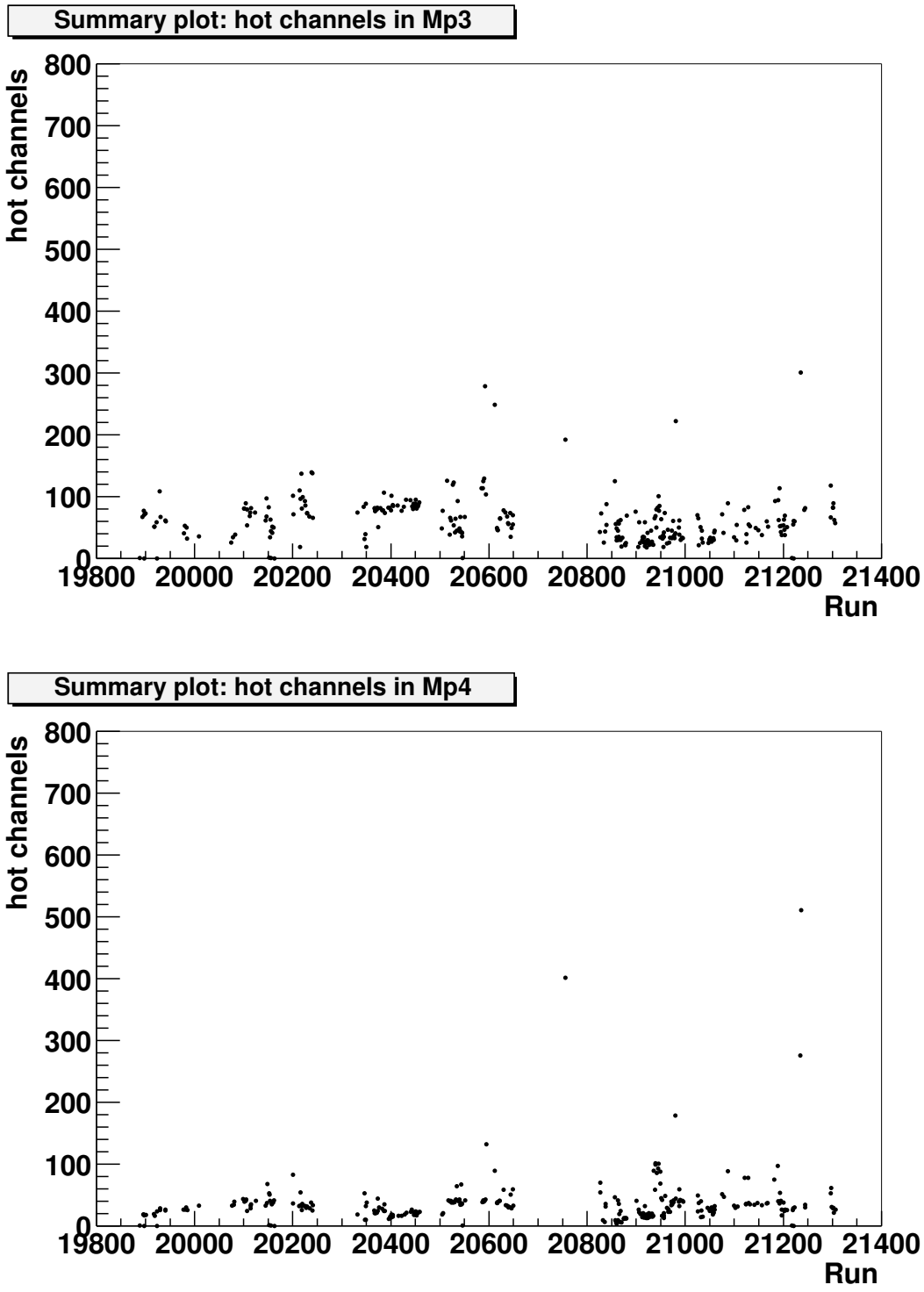

Figure 4.5: Summary plots of the number of hot channels versus the run number: in Mp3 (top) and in Mp4 (bottom).

tem are dead. These dead quadrants appear also on the pretrigger rate plots. The corresponding run, 20980, should be excluded from the analysis.

4.4 The Influence of Hot Channels on Muon Tracking

In order to understand the meaning of the results obtained so far and to judge the data quality of the muon detector in each run, the influence of the hot channels on muon tracking had to be established. The motivation is, that an increased number of hits in the muon subdetector leads to more combinatorial possibilities for the track reconstruction process. This means, that hot channels might result in more tracks to be reconstructed. Another motivation is, that more hits should influence the quality of the tracks, a measure of which is the muon likelihood, $lmmu$.

To study the effect of hot channels, a simulation was carried out. Monte Carlo data were passed through the track reconstruction chain, and the number of muon candidates was recorded (with the standard cut on the muon likelihood of $lmmu > 0.01$).

For 20000 events, 34088 muon candidate tracks were reconstructed. Then hot columns (i.e. entire chambers, each chamber containing 16 wires) were added. The software framework of HERA-B provides a tool to add artificial hits in a certain chamber. Before track reconstruction, artificial hits are added with a certain probability in all 16 wires of the respective chamber. The artificial noise induces also correlated noise in the neighboring chambers, but with a lower probability of receiving an artificial hit. By setting different values of the probability of adding a hit, the occupancy of the chamber can be tuned. In the present case, the probability was set to 90%. For the neighboring chambers the probability was only 10%. With this choice of the parameters a situation as in the real data has been achieved.

The muon likelihood distribution was studied including these hot channels, resulting in 34088 reconstructed muon tracks, exactly as in the case, when no hot channels were added. The ratio of the two muon likelihood distributions can be seen in Fig. 4.6 (left), suggesting that there is absolutely no influence. The list of hot columns, which were artificially added, are given in Appendix B.

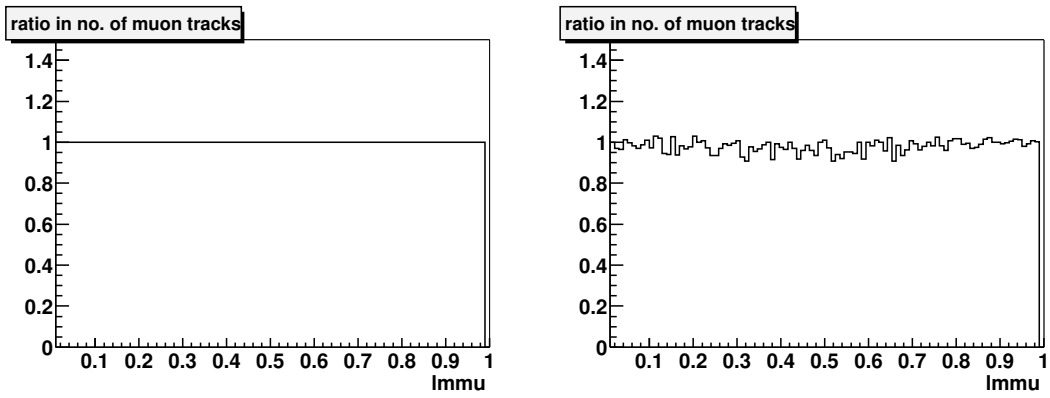

Figure 4.6: Ratio between the muon likelihood distributions in the case when no hot channels are present and artificial hot channels are added in about 2% (left), or 25% (right) of the detector channels. In the first case no change can be noticed, while in the second only a marginal influence is observed.

In a second simulation simulation, the extent, to which hot channels were added, covered about 25% of the detector. The list of all these channels can be found in Appendix B. The number of reconstructed tracks in this case was 34478, exceeding by 1.14% the number of muons in the case, when no hot channels were added. The ratio of the two muon likelihood distributions can be seen in Fig. 4.6 (right). The distribution is flat, suggesting that no shift in the muon likelihood has appeared. This means, that there is no influence on the track quality.

The marginal influence can be explained, on one hand, by the fact that a track is reconstructed, if it leaves hits both in the muon detector and in other detector components such as the outer tracker. On the other hand, a reconstructed track must leave hits in many layers of the muon detector. This leads to the conclusion, that hot channels in the muon tube and pad chambers alone do not affect the quality of the recorded data, and that no runs should be excluded.

4.5 Pretrigger Rate Analysis

In the case of the pretrigger coincidence rate distribution, which is a function of the column and pad numbers (see Fig. 4.7), a study similar to that of the muon pad occupancy has been performed.

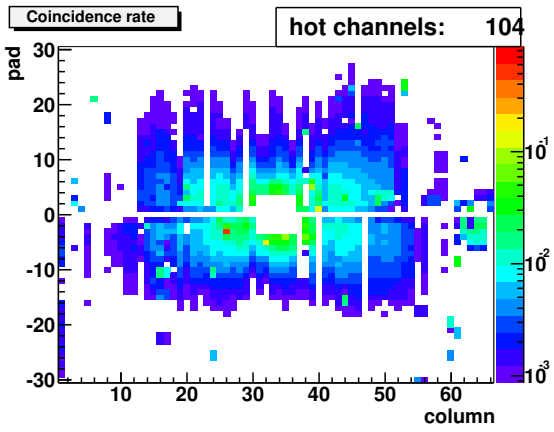

Figure 4.7: Muon coincidence rate of the pretrigger for Run 20527.

Again the median has been determined, but in a different way. Because of the magnet, the muon tracks are bent in the x direction and the distribution is smeared out along the x axis. This effect is stronger, if a coincidence in two superlayers is required. That is why the R^{-a} parameterization is no longer accurate. For reweighting the formula [Ada01a]:

$$R_{coincidence}(c,p) \propto \exp\left(- \left[\left(\frac{c-a}{c_1}\right)^2 + \left(\frac{p-b}{c_2}\right)^2 \right]^{d/2} \right) \tag{4.2}$$

was used, where c and p are the column and pad numbers. a, b, c_1, c_2, d are parameters, which were obtained by fitting the distribution obtained from a MC data sample with the above function. The values used are: $a = 33$, $b = 0.1$, $c_1 = 1$, $c_2 = 1$ and $d = 0.5$ [Ada01a]. As in the previous case, empty bins or channels had to be disregarded. A channel was considered hot, if the average coincidence rate recorded exceeded the threshold of four times the median. Then they were plotted vs. the run number, and

the stability over the entire period could be studied. The average number of hot channels was about 106 ± 32, which represents $2.6 \pm 0.8\%$ of all channels.

Two cases were found, where the pretrigger data might be wrong. In the first case the area surrounding the electron beam has a very high occupancy, caused by backscattering of electrons coming from the electron beam. This can be seen in Fig. 4.8 (left). In total six runs corresponding to this case were found. They are described in Table 4.5.

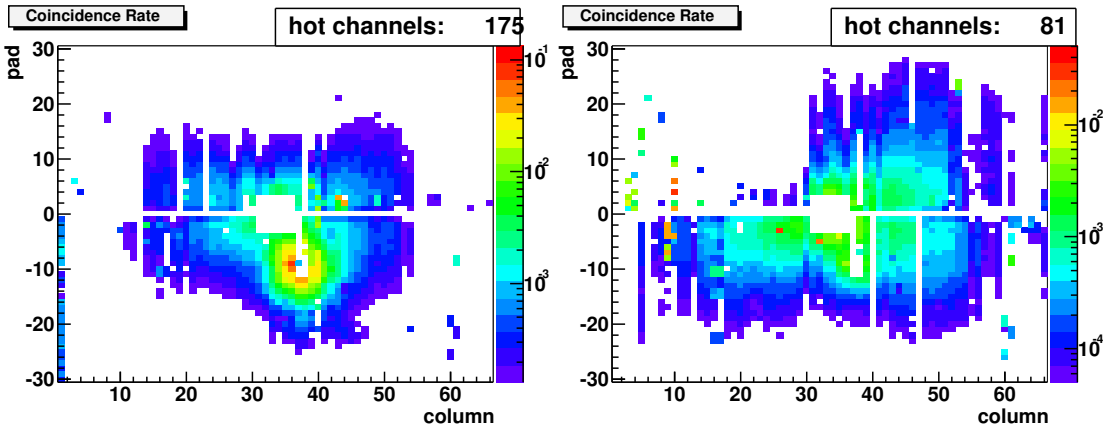

Figure 4.8: Runs with abnormal behavior of the pad coincidence rate: electron hits in the muon detector in Run 21237 (left), a dead quadrant in Run 20366 (right).

Table 4.5: Runs, where the electron beam causes hits in the muon detector.

Runs with electron hits	DQ files affected
20939	2/2
20959	1/1
20963	1/4
21050	1/1
21203	1/1
21237	2/2

In the second case one of the quadrants is dead or the distribution in that quadrant is much lower than in the other three. At the beginning of several runs, the coincidence rate in the $(-x, +y)$ - quadrant of the muon pretrigger system was reported to drop from the normal level to the level of random coincidences. This "missing quadrant" problem was due to a mis-synchronization of the corresponding FED systems in MU3 and MU4 and was usually solved by re-initializing the FED crates. Since this problem was not always realized immediately, the data quality of several runs was compromised by the "missing quadrant" problem. A typical example can be seen in Fig. 4.8 (right).

A list of the runs affected was produced by calculating the ratio of median occupancies for the "missing quadrant" and the working quadrants on the basis of the muon pretrigger data quality histograms [Hus03]. The data quality files, i.e. 30-minute parts of a run, in which the ratio of medians is less than 45%, are marked as "missing quadrant" periods, see Table 4.6. In total, 27 runs of two run periods (November 7–12, 2002 and January

2003) and approximately 6,300,000 events are affected. Note that for these events, also the FLT efficiency calculation is wrong, since averaging over neighboring cells in the FLT efficiency map fails for the missing quadrant.

Table 4.6: List of "missing quadrant" runs.

Runs with $(-x,+y)$ - dead quadrants	DQ files affected
20333	1/5
20346	1/1
20347	1/1
20348	2/2
20349	2/2
20365	2/18
20366	2/2
20367	1/2
20369	1/1
20370	16/16
20371	2/2
20372	5/5
20375	1/1
20377	1/2
20383	1/3
20385	5/6
20386	1/1
20387	2/5
20457	1/3
20593	1/9
20612	1/1
20826	2/2
20827	5/5
20832	2/2
20837	1/2
20975	1/5
Runs with $(-x,-y)$ - dead quadrants	DQ files affected
20980	2/2

4.6 Concluding remarks

A quality check of the data recorded during the HERA-B 2002/2003 data taking period has been performed. Hit occupancies recorded in all layers of the muon subdetector have been investigated for all runs accepted for physics analysis.

A simple, and yet reliable, method was developed, which, in an automatic procedure, performs a check of the data quality of each run. This check provides a quantitative measure of the hot channels in the detector. Then, these values are averaged for runs recorded over several time periods.

These values are then used in a simulation, which determines the influence of hot channels on the physics analysis. The influence on the muon track reconstruction has been investigated. Hot channels, at the rate, that was observed under normal conditions, have no observable effect on the investigated process, therefore no runs should be excluded on account of the observed hot channels.

The pretrigger coincidence rate distributions have also been studied. Problems have been identified in several runs, where "missing quadrants" were observed, or the electron beam produced hits in the detector area.

Chapter 5

Efficiency Study of the Muon Pretrigger System

In this chapter an efficiency study of the HERA-B muon pretrigger system is presented. As mentioned in the previous chapters, the muon pretrigger is one of the starting points of the trigger chain. Its role is the search for coincidences between muon hits in the two pad layers of MU3 and MU4, providing muon candidates, e.g. for $J/\psi \rightarrow \mu^+\mu^-$ decays.

To determine the efficiency of the muon pretrigger, three data samples have been analyzed. They were taken with a special setup, which allows the estimation of the efficiency. The setup is described in the second section of the chapter.

Then the software simulation of the pretrigger hardware is briefly presented. This simulation describes the behavior of the system. Its results, i.e. simulated pretrigger messages, can be compared to real pretrigger messages. From this comparison, the efficiency of the system can be determined.

The main methods for determining the efficiency are introduced next. Finally, the analysis of several data runs is presented, as well as a discussion of the results.

5.1 The Muon Pretrigger Efficiency

The muon pretrigger system is an important component of the trigger chain, and therefore of the data acquisition (DAQ) system. When a simulation of the behavior of the entire system is performed, in order to compare measurement results with theoretical predictions, the efficiency of the pretrigger should also be taken into consideration.

A first study of the muon pretrigger efficiency was realized for the data recorded in the HERA-B run in 2000 [Ada01a]. However, for the 2002/2003 data taking period, several changes have been performed. Among these changes, the optical links were repaired and optimized, and the connections to the first level trigger (FLT) were reorganized. Therefore, a new estimation of the efficiency is necessary. Since the pixel system was not used during this period, the efficiency will be studied only for the outer part of the detector, i.e. the pad system.

The main concept of this analysis is to check the number and contents of messages produced at the output of the pretrigger. The pretrigger receives muon hits in the pad system, processes these data by searching for coincidences of hits in MU3 and MU4 and generates messages for the higher trigger levels. The most important information, which is contained in these messages, regards the position of the coincidence and the slope of the resulting track candidate. The efficiency is calculated from a comparison between

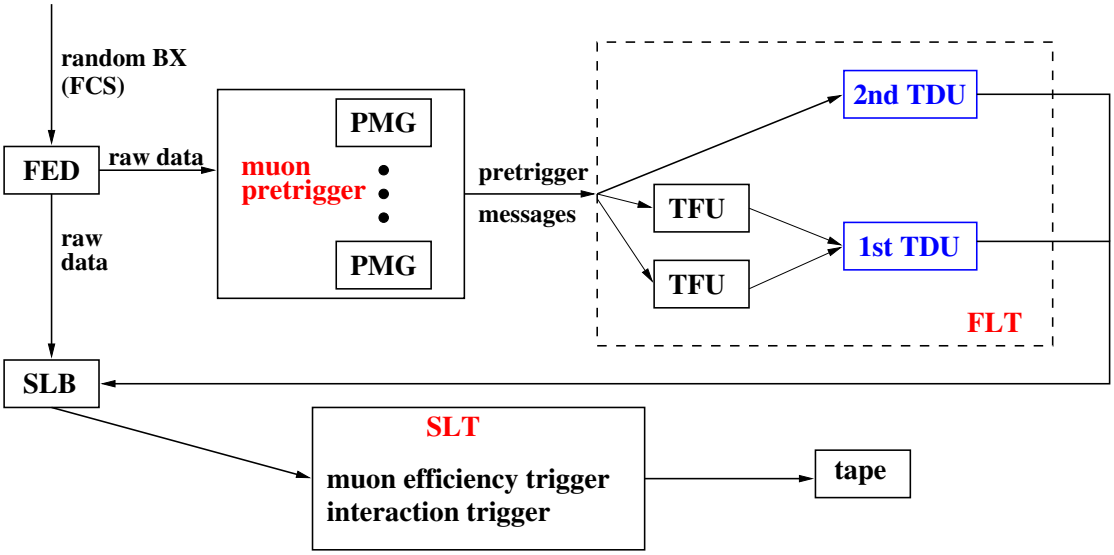

Figure 5.1: Trigger configuration for the muon pretrigger efficiency runs. The raw data are sent to the pretrigger, where messages are produced. They are sent to the 1st and 2nd TDU of the FLT, which runs in the "transparent mode". The event selection is implemented only in the SLT.

the real messages coming from the pretrigger, and messages produced in a detailed simulation of the pretrigger. The simulation performs the same operations as the muon pretrigger on the same input data. The simulated messages have the same format as real ones.

The input data must be recorded without the muon pretrigger actively selecting events. Therefore a special configuration of the trigger chain has been used. This is detailed in the next section.

5.2 The Trigger Configuration Used for the Data Taking

The configuration of the trigger in the di-lepton trigger mode has been described in Chapter 2. However, this setup is not suitable for recording data to be used for the efficiency estimation. This is due to the fact, that events must not be selected by the pretrigger, but yet the events have to contain messages generated by the muon pretrigger. Thus a special trigger setup was used, in which the muon pretrigger and the FLT were not used as triggers, i.e. for selecting events, but in "spy mode", i.e. the trigger output was saved in the data stream. A schematic view of this setup can be found in Fig. 5.1.

The data coming from the front end driver (FED) are passed as input to the muon pretrigger, which performs the coincidence search and produces messages. They are further transmitted to the FLT. Due to the fact that, the muon pretrigger hardware cannot record all the information of the several processing steps (see Chapter 3), only the output messages are kept. For this reason, in the 2000 run, the FLT had to be operated in the so-called "transparent mode". This mode does not perform track search and reconstruction, and no events are selected. Therefore, the input messages from the pretrigger have been directly copied to the trigger decision unit (TDU). In the 2002/2003 run, another TDU (called 2nd TDU) has been introduced, in which the pretrigger messages are directly written, without having to traverse the FLT. In this

setup, the original TDU (1st TDU) contains both the original pretrigger messages and messages from the FLT chain.

The events must still be triggered in order to reduce the huge amount of data to be processed and stored to tape. This is achieved by using a random trigger, which is provided by the fast control system (FCS). It supplies a random bunch crossing number (BX) to the FED, which is unique to each stored event (the FED contains a ring buffer memory which can store up to 128 events, each having a unique tag represented by the BX number). The randomly selected events are copied to the second level buffer (SLB) and from there to the second level trigger (SLT). Here the trigger decision is enhanced by applying additional trigger algorithms implemented in software. In the 2002/2003 data taking period, two types of SLT triggers were used for the pretrigger efficiency runs. One is a muon efficiency trigger, which selects only those events, which have a muon track with hits in all four wire layers of the muon detector along the path of the track. The other trigger mode is called "interaction trigger". It selects events which have at least 20 hits in the RICH or hits in the ECAL with a total deposited energy of at least 1 GeV. Provided that the event is accepted by the SLT, it is passed to the fourth level trigger (4LT) and then written to tape, together with the pretrigger messages from the TDUs.

For the muon pretrigger efficiency study, three runs were recorded during the 2002/2003 data taking period. The first run, 20582, was recorded on December 1st, 2002, with the muon efficiency trigger, at an interaction rate of 2.87 MHz. It contains about 500,000 events. Run 21012 and Run 21013 were recorded on January 30th, 2003, and contain about 750,000 and 4,600,000 events respectively. The last two runs were recorded with different trigger setups (muon efficiency trigger for Run 21012 and interaction trigger for Run 21013). In both cases the average interaction rate at the target was 4.86 MHz. Table 5.1 contains the list of runs used for the efficiency study.

Table 5.1: Runs used for the muon pretrigger efficiency study.

Run number	Date	Target rate [MHz]	Trigger mode	Number of events
20582	12/01/2002	2.87	muon efficiency trigger	507,245
21012	01/30/2003	4.86	muon efficiency trigger	756,631
21013	01/30/2003	4.86	interaction trigger	4,613,412

5.3 The Software Simulation of the Muon Pretrigger

In order to determine the efficiency of the muon pretrigger, it is necessary to compare the real messages, obtained as output from the pretrigger, with messages obtained as result of a simulation of the pretrigger hardware. A software package, called MUPRESIM [Ada01a, Ada01b], previously developed for the same study on the data recorded in 2000, has been used for this analysis. The program is integrated into ARTE, the standard online and offline reconstruction software used in HERA-B. Thus it can run in the same mode as the standard offline analysis, using as input the data files recorded for each run, under the trigger conditions mentioned in the previous section. The software simulates each hardware component of the muon pretrigger, such that all

internal processes, that take place in the real modules, are described in the software.

5.3.1 The Main Features of the Simulation Program

The main features of MUPRESIM are given below.

- Various versions of the geometry description of the muon detector, i.e. alignment specifications and masking of hot channels, can be set at the initialization of the program.

- The program follows a modular design. Hence, every component of the pretrigger system is individually represented inside the program. This is achieved by implementing the software in the C++ language, and by making use of the object oriented programming technique. Object oriented programming is an implementation method by which every entity is represented by an object, which is the instance of a class. A class is defined by a set of data members, which determine its properties, and by a set of functions, which determine its behavior. Several classes are designed for the simulation such, that the main hardware modules of the pretrigger system can be implemented in distinctive classes. By making use of the classes' functions, the operations performed by the pretrigger modules can be replicated inside the program. One of the advantages of the modular design is that the software could be easily adapted to the setup required for the 2002/2003 run.

- The MUPRESIM core can be used inside ARTE. This comprises an easy-to-use interface and allows access to various databases needed for the configuration of the muon pretrigger simulation. It also facilitates the access to the data used as input by MUPRESIM.

- The output of the simulation are pretrigger messages identical in construction to the real pretrigger messages, i.e. they contain the same parameters.

5.3.2 The Components of the Simulation Program

The simulation software is composed of several classes used to describe the pretrigger modules, to initialize the program with the correct settings (such as geometry and masking), and also to encapsulate the messages transmitted between various components. The classes forming the program can therefore be grouped according to their functionalities.

There are classes used to represent coincidences (containing the same parameters as described in Chapter 3) and messages generated by the pretrigger. The latter are the output of MUPRESIM and contain various parameters as shown in Table 5.2. These parameters are used by the FLT to determine the region of interest (RoI), in which a hit search is performed (see Section 2.3.2). For the muon pretrigger efficiency only the ξ and η parameters, denoting the x and y positions, are of importance.

Several classes are used for the setup of the program. There are classes describing the geometry of the detector needed for determining the coincidences. Such are classes for the pads and for the pixel cells. There are also classes denoting the cable links between the different components of the system. A master setup class initializes all instances of the classes mentioned above, as well as all the components of the program.

Table 5.2: The list of parameters contained in the muon pretrigger messages, together with their sizes, and the positions of the first bit of each parameter (after [Ada01a]).

Symbol	Parameter	Size in bits	Position of 1st bit
TDI	ID number of receiver	8	0
$n\xi$	multiple messages flag	1	8
ξ	x position	10	9
$d\xi$	slope of the track	8	19
$dd\xi$	size of the search window	8	27
η	y position	9	35
w	number of neighboring detector cells	2	44
all	hits in all TFU layers	1	46
BX	cross bunching number	8	47
ID	pretrigger identification number	2	55
P	momentum estimate	7	57
$flag$	unconditional forwarding	1	64
E^+	bremsstrahlung correction for positron	7	65
E^-	bremsstrahlung correction for electron	7	72
nc	not used so far	1	79

Another set of classes describes the main electronics components of the pretrigger system. Such are the classes needed for the pretrigger link board (PLB), for the pretrigger coincidence unit (PCU) and for the pretrigger message generator (PMG). They have the same functionalities as the real counterparts.

5.4 The Methods Used for Determining the Efficiency

To determinine the efficiency of the muon pretrigger system, a comparison must be carried out between the MUPRESIM result, and the real pretrigger data. The input data for the simulation software are raw events of the runs mentioned in Section 5.2, selected with the special trigger setup for the study of the pretrigger efficiency. The output data are software simulated pretrigger messages. They must be compared with messages generated by the real system, which are retrieved from the FLT record. A schematic view of the data flow in the efficiency study is presented in Fig. 5.2.

To obtain meaningful results, the simulation must be carefully set up. The same masking of defective readout channels of the pad system has been used as the one at the moment of data taking. The look-up tables (LUTs) used during the data taking correspond to the detector geometry at the time of their generation, i.e. version 02.0903. In order to generate identical messages in real data and simulation, this geometry has been chosen for the simulation.

The efficiencies of the pretrigger optical links (POLs), which transmit the data from the pretrigger link boards (PLBs) to the pretrigger coincidence units (PCUs), were not always 100%. Therefore they have to be taken into account by the simulation. A determination of the POL efficiencies was attempted by computing the failure rate at regular time intervals, based on external monitoring information from the muon pretrigger online software. However, this information is not accurate enough, and the computed

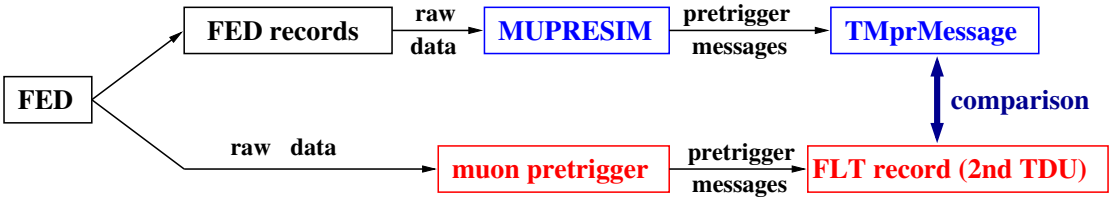

Figure 5.2: Schematic view of the method used for the pretrigger efficiency study. MUPRESIM receives as input raw events from the FED records and yields simulated messages. They are encapsulated into a class, and stored into an n-tuple. The same raw events are used by the muon pretrigger to produce messages. These messages are retrieved from the 2nd TDU of the FLT and stored into the same n-tuple as the simulated messages. In the efficiency analysis simulated and real messages are then compared.

efficiencies are not suitable for using them inside the simulation. Hence, the simulation was carried out without them. POL inefficiencies result in lower efficiencies of the entire affected columns. Another study has been performed to determine POL efficiencies of di-lepton triggered data, averaged over all the period of data taking [Hus04]. It is based on the same simulation software of the pretrigger, therefore also these values cannot be used in the pretrigger study. However, they can be used to cross-check channels where lower efficiencies are found.

Another important fact is that the RICH multiplicity veto was unintentionally not turned off during the data taking. The RICH veto system is used to inhibit events with a too high track multiplicity. When the number of hits in a part of the RICH exceeds a certain threshold, it delivers a veto signal to the pretrigger. This signal stops the transmission of data of the current event. As a consequence, a small fraction (about 5% at an interaction rate of 5 MHz) of the events is rejected in the real data. This cannot be simulated in the software, since the RICH FEDs were not recorded. As a result, for these events a non-zero number of simulated messages can be found, while no corresponding messages can be found in the real data. To overcome this, a cut is applied such, that all events with no messages in real data have been neglected.

The correlation between the number of real and simulated pretrigger messages in each event is shown in Fig. 5.3. In this correlation plot, a perfect match between simulated and real messages (i.e. maximum efficiency) is represented by a line, given by $n_{Sim} = n_{FLT}$. Here $n_{Sim}(n_{FLT})$ represents the number of simulated (real) messages recorded in each event. Any inefficiency of the pretrigger system causes a deviatin from the ideal line. However, for $n_{FLT} = 0$, the number of simulated messages is dominated by an uncorrelated contribution. This is due to the RICH veto, which suppresses real pretrigger messages. Only those events, for which

$$n_{FLT} \neq 0, \tag{5.1}$$

were accepted for the efficiency analysis.

Each muon pad represents an individual readout channel, of which the data are passed as input to the muon pretrigger. In the pretrigger, hits between MU3 and MU4 are matched and a search for coincidences is performed. In the case of coincidences, each message generated can be attributed to a MU3 pad. The total number of messages can be expressed as a function of the column and pad numbers c and p.

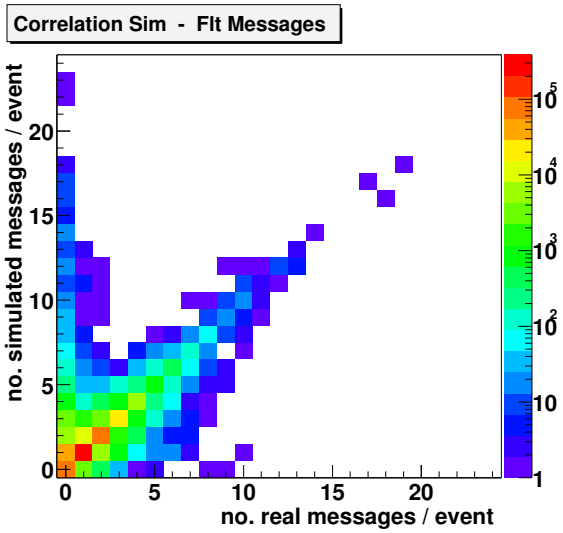

Figure 5.3: Correlation between the number of real messages and number of simulated messages in each event for Run 21012.

To determine the efficiency $\varepsilon(c,p)$ of each channel , the ratio

$$\varepsilon(c,p) = \frac{N_{FLT}(c,p)}{N_{Sim}(c,p)} \tag{5.2}$$

has been calculated. Here $N_{FLT}(c,p)$ represents the total number of messages found by the muon pretrigger system, as retrieved from the FLT record of the 2nd TDU. $N_{Sim}(c,p)$ represents the corresponding total number of messages obtained at the output of the simulation program.

The column and pad numbers can be obtained from the values of the ξ and η parameters contained in each message, which determine the x and y positions. ξ represents the x coordinate of the MU3 pad edge, which is fsrthest in the $+x$ direction. Therefore the x position of the center of the pad can be determined as

$$x[cm] = \xi - 6.2, \tag{5.3}$$

where 6.2 represents half a pad size in cm. The y position can be determined as

$$y[cm] = \eta \cdot 1888, \tag{5.4}$$

where 1888 represents the z position of MU3 in cm.

The average efficiency $\overline{\varepsilon}$ of the muon pretrigger can be expressed by the arithmetic mean, computed from the efficiency values corresponding to individual channels:

$$\overline{\varepsilon} = \frac{\sum\limits_{c,p \in S} \varepsilon(c,p)}{N}, \tag{5.5}$$

where S is the set of all pads in MU3.

The uncertainty of the computed efficiency has been determined applying the theory of binomial probability distributions. See e.g. [Cow98] for an introduction. N_{sel} messages from a channel are selected with a given probability from a total of N messages. This probability is determined as the efficiency $\tilde{\varepsilon}$ of the channel. Then the distribution

function, that describes the probability that N_{sel} messages are found in a total of N messages, in a channel with the efficiency $\tilde{\varepsilon}$ is given by:

$$P(N_{sel}, N; \tilde{\varepsilon}) = \frac{N!}{N_{sel}!(N - N_{sel})!} \cdot \tilde{\varepsilon}^{N_{sel}} \cdot (1 - \tilde{\varepsilon})^{N - N_{sel}}, \tag{5.6}$$

and the variance is given by:

$$V(N_{sel}) = N \cdot \tilde{\varepsilon} \cdot (1 - \tilde{\varepsilon}). \tag{5.7}$$

The efficiency is determined as the total number of real pretrigger messages divided by the total number of simulated messages: $\tilde{\varepsilon} = \varepsilon(c,p)$, $N_{sel} = N_{FLT}(c,p)$, and $N = N_{Sim}(c,p)$. The statistical uncertainty $\sigma_\varepsilon(c,p)$ of the efficiency measurement can be determined from the variance:

$$\sigma_\varepsilon(c,p) = \sqrt{\frac{\varepsilon(c,p) \cdot (1 - \varepsilon(c,p))}{N_{sim}(c,p)}}, \quad \text{for} \quad \varepsilon(c,p) \neq 0 \quad \text{and} \tag{5.8}$$

$$\sigma_\varepsilon(c,p) = 1 - 0.32^{1/(N_{sim}(c,p)+1)}, \quad \text{for} \quad \varepsilon(c,p) = 0, 1. \tag{5.9}$$

where $\varepsilon(c,p)$ is the pretrigger efficiency for a specific channel and $N_{sim}(c,p)$ is the total number of simulated messaged belonging to that channel. The uncertainty of finding a given efficiency in a channel increases with the decrease of the total number of simulated messages in that channel. For example, for a channel with $N_{Sim} = 10$, the uncertainty in determining an efficiency of 99% is 3%. Therefore a cut on the minimum allowed number of messages in a channel has to be imposed. In the analysis only those channels with at least 10 simulated messages are used:

$$N_{Sim}(c,p) \geq 10. \tag{5.10}$$

Another way to compute the average value of the efficiency is by weighting the average value according to the uncertainties computed in (5.8) and (5.9):

$$\bar{\bar{\varepsilon}} = \frac{\sum\limits_{(c,p)\in S} \frac{\varepsilon(c,p)}{\sigma^2_\varepsilon(c,p)}}{\sum\limits_{(c,p)\in S} \frac{1}{\sigma^2_\varepsilon(c,p)}}. \tag{5.11}$$

This equation takes the uncertainty of determining a given efficiency in a channel into account, which decreases with the increase of the number of messages in that channel.

Since the (x, y) - distribution of hits and coincidence messages shows a radial dependence on the distance from the proton beam, another way to compute the average efficiency is taking the occupancy of each channel into account for events containing interesting physics signals. Channels in the region closer to the beam pipe have much higher occupancies than the ones in the outer region. It can be argued that the efficiency of high occupancy channels is more "important" than that of the low occupancy channels. Hence, yet another way of computing the efficiency is by weighting the efficiency distribution, as computed from (5.5), with a function, which describes the radial dependence of muons from J/ψ decays. Such a function has been determined in [Ada01a]:

$$w_{J/\psi}(c,p) = \exp\left(- \left[\left(\frac{c - 33.28}{0.21} \right)^2 + \left(\frac{p - (-0.03)}{0.28} \right)^2 \right]^{\frac{0.44}{2}} \right). \tag{5.12}$$

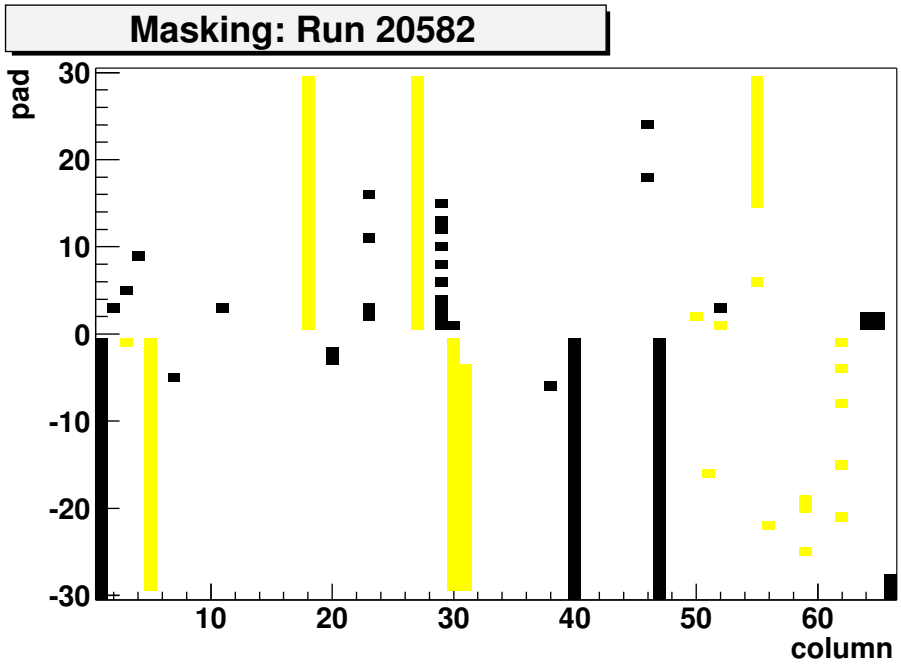

Figure 5.4: Masking of hot channels for Run 20582. The masked channels in MU3 are shown in black, while the ones in MU4 are shaded.

The mean efficiency, computed according to the equation given above reads:

$$\overline{\varepsilon}_{J/\psi} = \frac{\sum\limits_{(c,p)\in S} \varepsilon(c,p) \cdot w_{J/\psi}(c,p)}{\sum\limits_{(c,p)\in S} w_{J/\psi}(c,p)}. \tag{5.13}$$

5.5 Results for Run 20582

In this section, the results obtained for Run 20582 are presented and discussed. The masking of hot channels for Run 20582 can be seen in Fig 5.4. It was included in MUPRESIM such, that the channels, which are masked in the hardware, produce no simulated messages. In the distributions of real and simulated pretrigger messages as a function of the column and pad numbers (see Fig. 5.5), the channels masked in MU3 will appear empty, i.e. no messages are recorded in these channels. Since the coincidence scheme associates one MU3 column to three MU4 columns, the channels masked in MU4, will not appear as blank. In Table 5.3, the total number of masked channels in each superlayer is given.

Table 5.3: The number of masked channels in Run 20582.

Superlayer	total no. of channels	masked channels	masked channels in %
MU3	3916	123	3.1
MU4	3784	171	4.5

To compute the pretrigger efficiency the cuts mentioned in the previous section have been applied. First, those events, which were suppressed by the RICH veto, have been excluded by selecting only the events, which have a number of real messages different from zero ($n_{FLT} \neq 0$).

Each recorded event contains a variable number of messages. Each message comprises several parameters. The ξ and η parameters are used to identify the x and y positions of a hit in MU3. The column and pad numbers, c and p, can be determined from the x and y positions of the hit. Therefore, all messages can be assigned to the pads, where the coincidences have been found. In order to study the efficiency, the total number of messages in each channel, N_{Sim} and N_{FLT}, are taken into account. For each channel the efficiency $\varepsilon(c,p)$ is determined according to (5.2), and the uncertainty in measuring this efficiency is given by (5.8).

The values of the efficiency of each channel have been plotted with respect to the column and pad numbers, as in Fig. 5.6. Only channels containing at least 10 simulated messages have been taken into account ($N_{Sim} > 10$).

Another problem encountered is, that for several channels, the total number of real messages is higher than the number of simulated messages. Since this would result in an efficiency larger than 1, these channels have also been excluded from the analysis ($\varepsilon(c,p) \leq 1$). This aspect will be discussed in detail in Section 5.5.2.

Three different methods of computing the average value of the pretrigger efficiency have been described in Section 5.4. They provide the arithmetic mean $\overline{\varepsilon}$ (5.5), the mean weighted according to the uncertainty in determining the efficiency $\overline{\overline{\varepsilon}}$ (5.11), and the mean weighted according to the hit occupancies of muons from J/ψdecays in the pad system $\overline{\varepsilon}_{J/\psi}$ (5.13). Since the measurements of the efficiency in each channel are independent of each other, the uncertainty of $\tilde{\varepsilon}$ can be calculated as the standard deviation of the mean value:

$$\sigma_{\tilde{\varepsilon}} = \sigma_{\varepsilon}/\sqrt{N} = \sqrt{\frac{1}{N-1}\sum_{c,p}\left(\varepsilon(c,p) - \overline{\varepsilon}\right)^2}/\sqrt{N}, \tag{5.14}$$

where $\sigma_{\tilde{\varepsilon}}$ is the standard deviation of the mean, σ_{ε} is the standard deviation, and $\tilde{\varepsilon}$ represents each of the means mentioned above. More explanations on error computations can be found e.g. in [Tay97]. The results obtained and the corresponding uncertainties are given in Table 5.4. It can be noticed, that all values of the mean efficiency are larger than 0.965 ± 0.002, which is the value for $\overline{\varepsilon}_{J/\psi}$.

Table 5.4: Mean values of the pretrigger efficiency for Run 20582. The arithmetic mean $\overline{\varepsilon}$ is computed using (5.5). The mean weighted according to the uncertainty distribution $\overline{\varepsilon}_{J/\psi}$ is calculated from (5.11). The mean weighted with respect to the hit distribution is given by (5.13).

Mean	Mean value of the efficiency
$\overline{\varepsilon}$	0.967 ± 0.002
$\overline{\overline{\varepsilon}}$	0.999 ± 0.002
$\overline{\varepsilon}_{J/\psi}$	0.965 ± 0.002

Another way of describing the quality of the system, is to count the number of channels in which the value of the efficiency is above a certain threshold. The result is

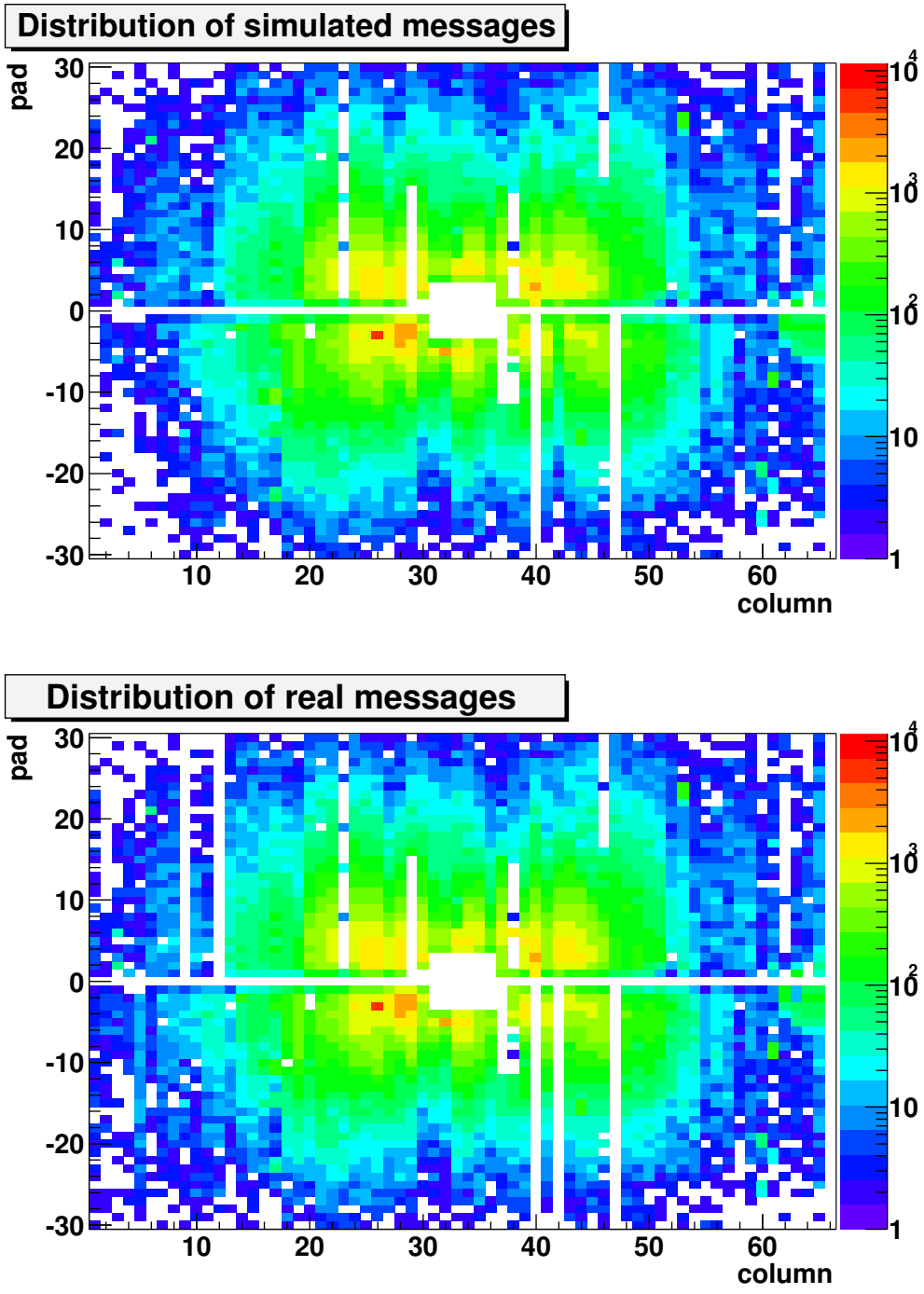

Figure 5.5: Distribution of messages in the muon pad system for Run 20582, in the case of simulated messages (top), and real messages (bottom).

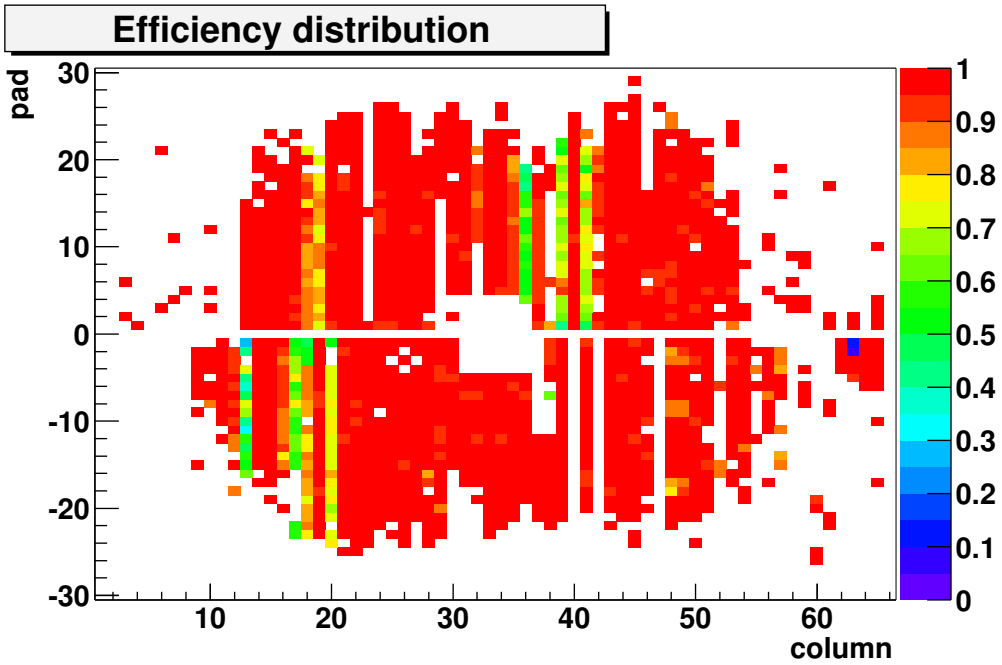

Figure 5.6: Efficiency distribution as a function of the column and pad numbers in Run 20582. The pads with efficiencies larger than 0.9 are displayed in red. Channels, where less than 10 messages were observed, were disregarded. Also the channels with $N_{FLT} > N_{Sim}$ have been excluded.

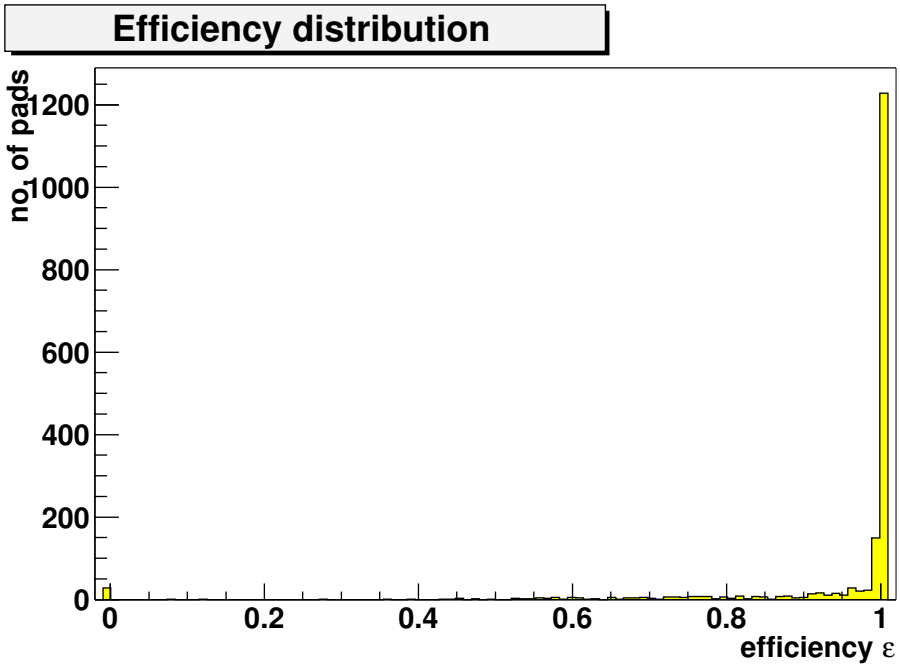

Figure 5.7: Distribution of the pad efficiencies for Run 20582.

given in Table 5.5. The ratio of channels in each interval is computed with respect to the total number of channels, for which the efficiency computation has been performed (i.e. 1679). 74.2% of all channels taken into account have an efficiency larger than 0.999, while only 10.1% have an efficiency smaller than 0.99.

Table 5.5: Number of channels with efficiencies above a certain threshold for Run 20582. Several lower limits for the efficiency have been chosen. The number of channels, used in computing the ratio, was the total number of channels which were considered for the efficiency study (i.e. 1679).

Efficiency larger than	No. of channels in absolute value	No. of channels in %
0.5	1666	99.2
0.9	1517	90.3
0.95	1455	86.6
0.99	1376	81.9
0.999	1246	74.2

This behavior is also illustrated in Fig. 5.7. In this histogram, the efficiency distribution is peaked at 1.

5.5.1 Influence of the Optical Links on the Efficiency for Run 20582

Since the efficiency of the pretrigger optical links was not included in the simulation, the channels for which this efficiency is less than one, have also a lower pretrigger efficiency. By studying these channels and their inefficiencies, defective optical links can be identified.

A first approach is to study the (x, y) - distribution of real messages, shown in Fig.5.5 (bottom). It can be compared with the masking of hot channels, depicted in Fig. 5.3. Since only the masking of the MU3 pads suppresses all messages in a channel, these channels can also be found in the plot showing the distribution of messages in the pad system. However, a few channels containing zero messages can be found, which do not correspond to the masking. This can be explained by the fact, that the corresponding POLs were not initialized, or that their efficiency was zero. The link efficiencies, obtained from the link efficiency study for Monte Carlo (MC) optimizations, have been used to check these columns. These are columns 9, 12, 66, in the $+y$ half, and columns 42 and 66, in the $-y$ half. All channels in these columns are empty. The POL efficiencies for all these columns have been found to be 0. In addition, a part of the channels in columns 23, 38 (lower half), and 56 (upper half) are also empty.

Another approach is based on the already computed pretrigger efficiencies (Fig. 5.6). The channels with lower efficiencies (i.e. the defective or the low link efficiency channels) can be identified in this distribution. It can be compared with another map, where only the simulated messages, which do not match with any real message, are plotted. A plot of such a distribution is shown in Fig. 5.8. While the former distribution of the efficiency has been filled with the ratio of the total numbers of real and simulated messages, the latter has been filled event by event. For each event, a simulated message, which did not find an identical message in the real data, was added to the histogram. This histogram describes the distribution of inefficiencies. The observed distribution is not a random

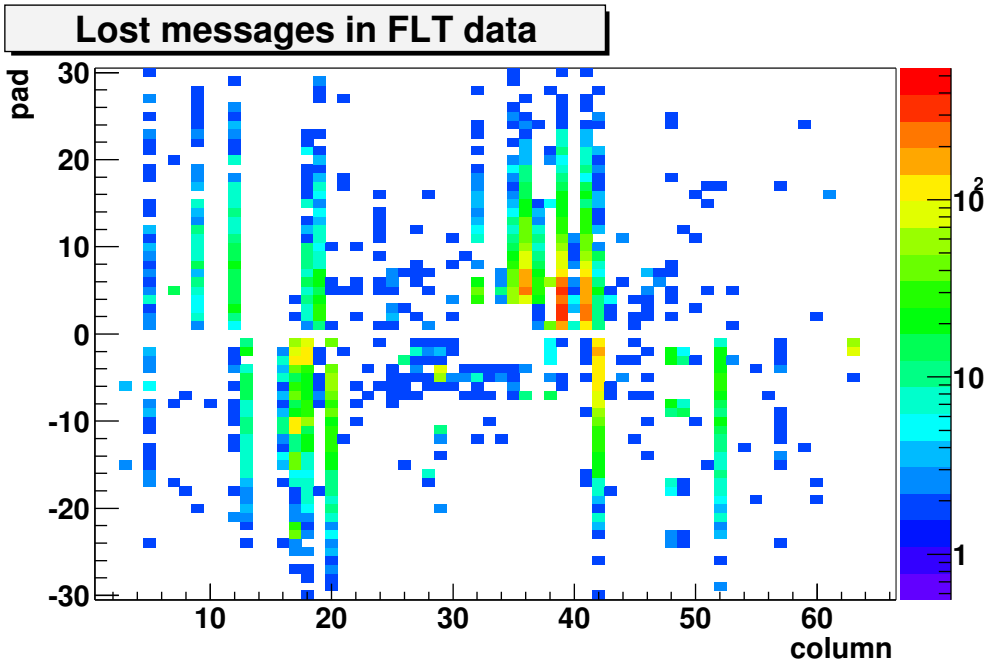

Figure 5.8: Distribution of messages which do not appear in real data in Run 20582.

distribution. The missing messages are located on specific columns of pads. Therefore, it is useful to identify defective channels, which lead to a lower efficiency of all pads of the column. In the following, it is used to spot the channels, where inefficiencies might have occurred, while the efficiency values are determined from the efficiency distribution plot.

In the $+y$ half, channels in the columns 18 and 19 have lower efficiencies. The values range between 0.7 and 0.95. The POL efficiencies used in MC, corresponding to the two columns have also been found to be less than 1. The two columns can be identified also in the plot, showing the lost messages in the real data. Here, three additional columns can be spotted, where inefficiencies have occurred, and which do not appear in the efficiency distribution. They are columns 5, 9 and 12. The columns 9 and 12 are not shown, since no messages have been recorded in the real data, as mentioned above. Column 5 was cut from the efficiency map due to the cut of low occupancy channels ($N_{Sim} > 10$). Three more columns with low efficiencies can be observed in both plots. They are columns 36, 39 and 41, where the efficiencies of individual channels vary between 0.45 and 0.7. For these three columns, the POL efficiencies used in MC were also found to be smaller (around 0.7 to 0.8). Three more columns, 32, 35 and 42 with efficiencies between 0.85 and 0.95 can be noticed.

Also in the $-y$ half, columns with problematic efficiencies can be observed. Columns 13, 16, 17, 18 and 20, whose efficiencies vary between 0.4 and 0.8, can be spotted. The lower efficiencies of columns 16, 17, 18 can be explained by a lower efficiency of the MU4 link of column 17. According to the coincidence scheme, it affects three neighboring columns. All five columns appear in both plots used for this study. However, in the plot showing the lost messages in the real data, one additional column can be observed, where real pretrigger messages are missing, suggesting a lower efficiency. This is column 5, and it is not shown in the efficiency distribution due to the cut of low occupancy channels. Another column, 42, can be seen in the former plot, but not in the latter.

This is again due to the fact, that no messages were recorded in the real data, and hence zero efficiency has to be assigned to the corresponding optical link.

All columns, where lower efficiencies have been observed, are listed in Appendix C, together with the corresponding optical links, which, in some of the cases, also featured an unstable behavior.

5.5.2 Influence of Channels with Efficiencies Larger than One for Run 20582

Since several channels were noticed, where the computed efficiencies were larger than one, the distribution of messages, which belong to events in real data, but not in simulated data, has been studied. As for the distribution of lost messages in real data, this histogram is filled on a event-by-event basis. The distribution can be seen in Fig. 5.9.

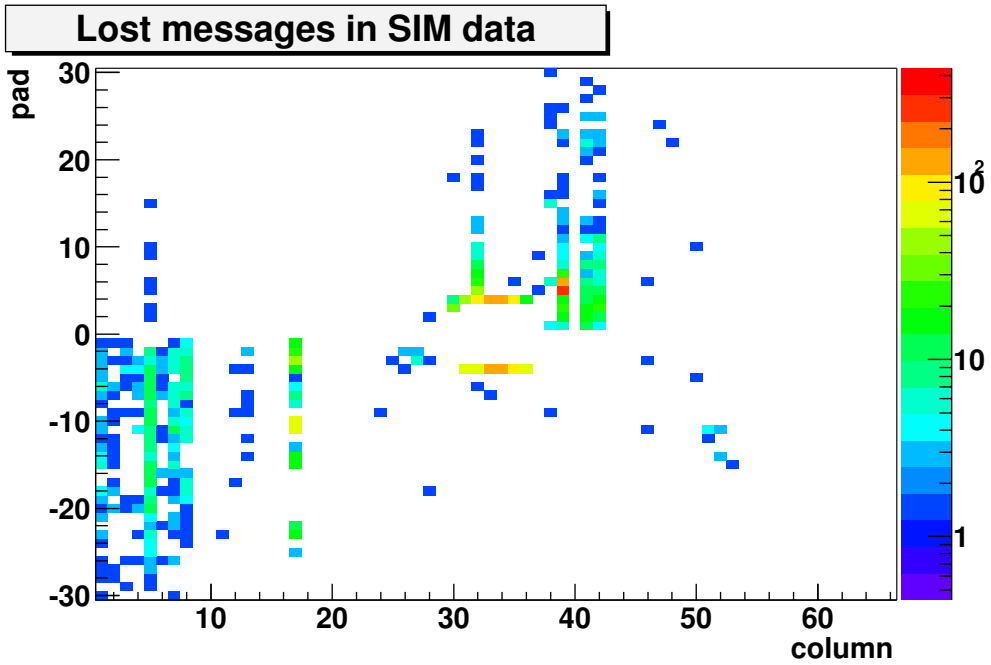

Figure 5.9: Distribution of messages, which do not appear in simulated data in Run 20582.

The message distribution is not random or radial dependent, the messages are produced by distinctive columns. The source of these extra messages in real data, which were not reproduced by the simulation, has to be further investigated.

Two distinct cases can be observed. In the first case, the first eight columns in the $-y$ half can be identified in the distribution. They all belong to a single PMG, suggesting that this board was defective. However, these channels do not affect the efficiency computation, because they are disregarded by applying the low occupancy cut ($N_{Sim} > 10$).

Another case is that of several columns, which are not connected to the same PMG. These columns are 17, in the $-y$ half, and 32, 39, 41 and 42, in the $+y$ half. Additional real messages might compensate part of the inefficiencies. In order to study this effect, the efficiency distribution has been recalculated, using the original distribution of simulated messages, and a new distribution of real messages. The latter has been determined by subtracting real messages, which do not match simulated ones, from the

original distribution of real messages. The new values for the mean efficiency can be found in Table 5.6. As expected, these values are smaller than the old values. However, the difference is of the same order of magnitude as the statistical uncertainty of the ε determination (0.001 lower for $\overline{\varepsilon}$).

Table 5.6: Mean values of the pretrigger efficiency for Run 20582 without channels having efficiencies larger than 1. The three different means were computed according to (5.5), (5.11) and (5.13).

Mean	Mean value of the efficiency
$\overline{\varepsilon}$	0.965 ± 0.002
$\overline{\overline{\varepsilon}}$	0.999 ± 0.002
$\overline{\varepsilon}_{J/\psi}$	0.965 ± 0.002

The number of channels, which have certain minimum efficiencies has also been recalculated, and can be seen in Table 5.7. The number of channels having certain minimum efficiencies is again slightly smaller, the difference being no more than about 1% (0.6% lower for the total number of channels having an efficiency of at least 0.999).

Table 5.7: Number of channels with efficiencies above a certain threshold for Run 20582, without the influence of channels having efficiencies larger than one. The number of channels, used in computing the ratio, was the total number of channels, which were considered for the efficiency study (i.e. 1723).

Efficiency larger than	No. of channels in absolute value	No. of channels in %
0.5	1699	98.6
0.9	1555	90.2
0.95	1492	86.6
0.99	1413	82.0
0.999	1269	73.6

5.6 Results for Run 21012

In this section the results obtained for Run 21012 are discussed. The run was recorded with the same trigger setup as Run 20582, i.e. the trigger was set in the "muon efficiency" mode. However, the interaction rate was set to a different value, at 4.86 MHz. The masking, which has been used for this run, can be seen in Fig. 5.10. The number of masked channels is given in Table 5.8.

Table 5.8: The number of masked channels in Run 21012 and Run 21013.

Superlayer	total no. of channels	masked channels	masked channels in %
MU3	3916	117	3.0
MU4	3784	173	4.5

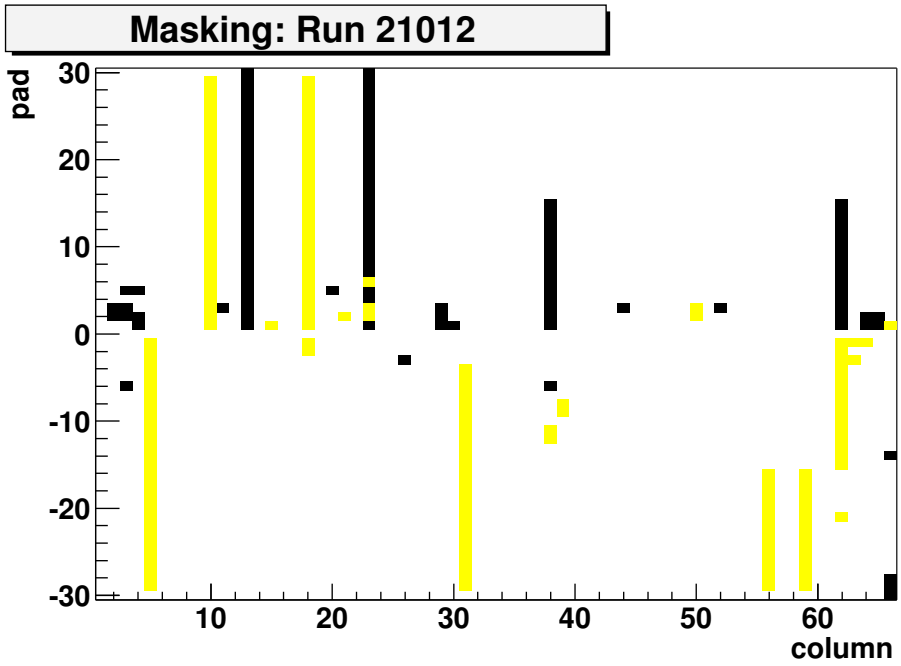

Figure 5.10: Masking of hot channels for Runs 21012 and 21013. The masked channels in MU3 are shown in black, while the ones in MU4 are shaded.

After applying the cut to exclude the events, which were suppressed by the RICH veto ($n_{FLT} \neq 0$), the two distributions of real and simulated messages, as a function of the column and pad numbers c and p, have been analyzed. They can be seen in Fig. 5.11.

To determine the efficiency distribution in the pad system, the additional cuts already used in Run 20582 have also been applied. These cuts exclude the low occupancy channels ($N_{Sim} > 10$), and the channels, where the efficiency was larger than 1 ($\varepsilon(c,p) \leq 1$). The resulting efficiency distribution can be seen in Fig. 5.12.

The values of the arithmetic mean, the mean weighted according to the uncertainty in computing the efficiency, and the mean weighted according to the muon hit occupancy function in the pad system were computed. They are shown in Table 5.9.

Table 5.9: Mean values of the pretrigger efficiency for Run 21012. The arithmetic mean $\overline{\varepsilon}$ is computed using (5.5). The mean weighted according to the uncertainty distribution $\overline{\overline{\varepsilon}}$ is calculated from (5.11). The mean weighted with respect to the hit distribution $\overline{\varepsilon}_{J/\psi}$ is given by (5.13).

Mean	Mean value of the efficiency
$\overline{\varepsilon}$	0.963 ± 0.002
$\overline{\overline{\varepsilon}}$	0.998 ± 0.002
$\overline{\varepsilon}_{J/\psi}$	0.968 ± 0.002

A comparison with the values obtained for Run 20582 shows, that the values obtained for this run are almost identical within the uncertainties. $\overline{\varepsilon}$ is smaller by 0.004, $\overline{\overline{\varepsilon}}$ by 0.001, while $\overline{\varepsilon}_{J/\psi}$ has a value larger by 0.003.

The number of channels, which belong to different intervals of the efficiency, deter-

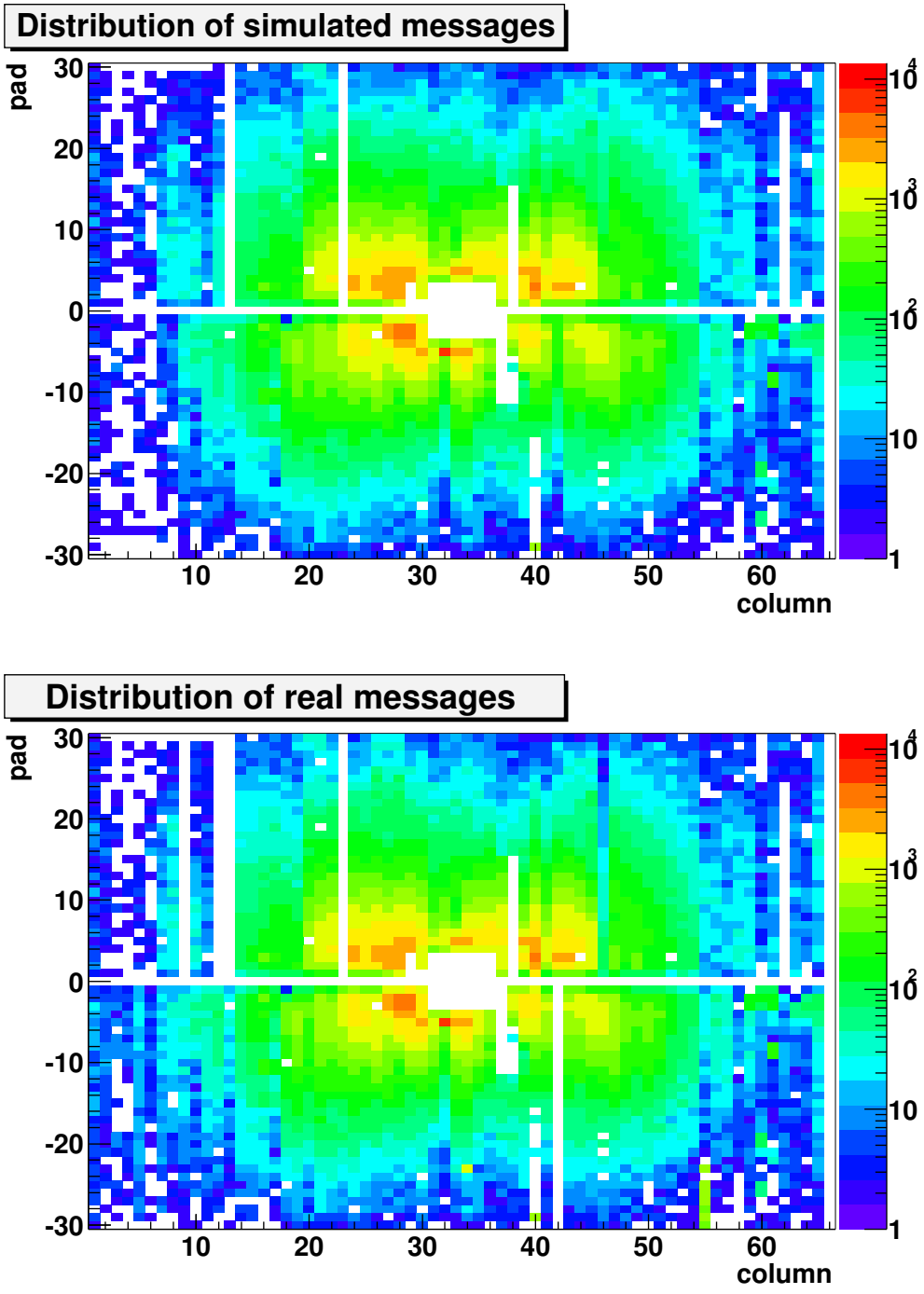

Figure 5.11: Distribution of messages in the muon pad system for Run 21012, in the case of simulated messages (top), and real messages (bottom).

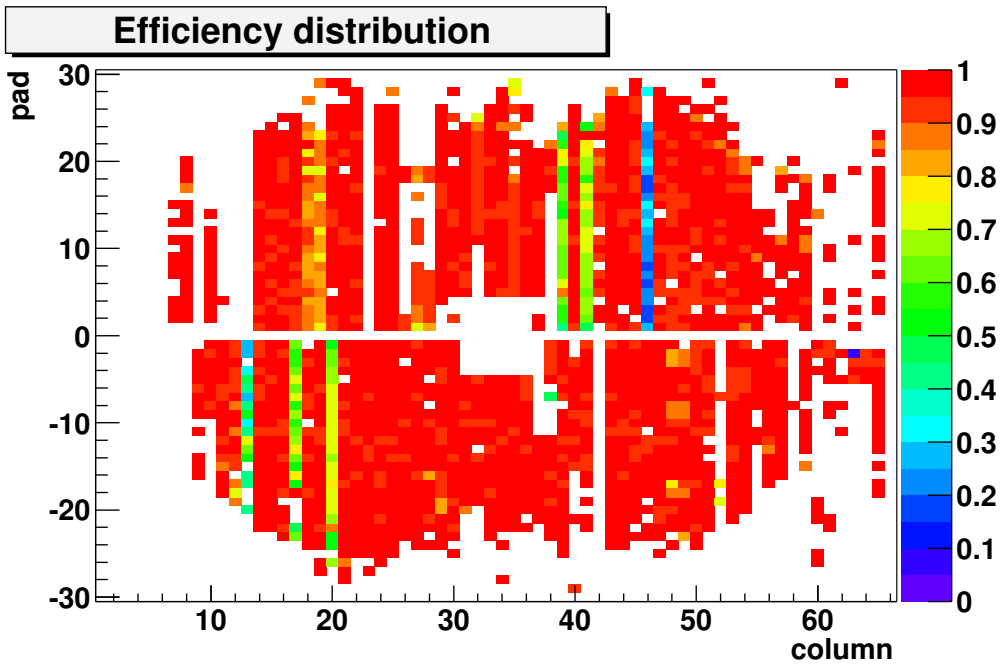

Figure 5.12: Efficiency distribution as a function of the column and pad numbers in Run 21012. The pads with efficiencies larger than 0.9 are displayed in red. Channels with less than 10 messages were disregarded, as well as channels with $N_{FLT} > N_{Sim}$.

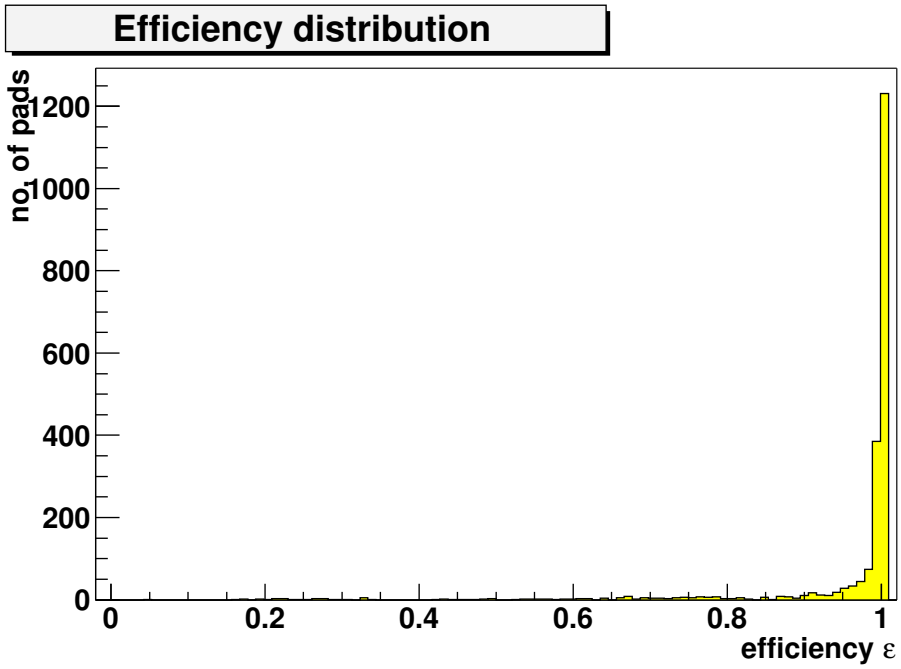

Figure 5.13: Distribution of the pad efficiencies for Run 21012.

mined by a lower limit, have also been computed. They can be found in Table 5.10. The total number of channels used in the computed ratios, which remained after all cuts, is 2039, i.e. 20% larger than in Run 20582.

Table 5.10: Number of channels with efficiencies above a certain threshold for Run 21012. Several lower limits for the efficiency have been chosen. The number of channels, used in computing the ratio, was the total number of channels, which were considered for the efficiency study (i.e. 2039).

Efficiency larger than	No. of channels in absolute value	No. of channels in %
0.5	1996	97.9
0.9	1861	91.2
0.95	1786	87.6
0.99	1605	78.7
0.999	1254	61.5

The distribution of efficiencies, computed for single channels in the pad system, can be observed in Fig. 5.13.

5.6.1 Influence of the Optical Links on the Efficiency for Run 21012

To check the observed inefficiencies in the pad system, the distribution of the simulated messages, which do not match with the real messages, was used. This distribution is shown in Fig. 5.14. There is a radial distribution of messages, which cause inefficiencies in the pads. These are real inefficiencies of the pretrigger system, but they represent only a small fraction compared to the total number of messages in those channels. If the inefficiency is computed as the ratio between the total number of lost messages in real data in a channel $N_{lostFLT}$, and the total number of simulated messages N_{Sim}, then its value would be around 0.005 in a rough approximation. This effect cannot be observed for Run 20582, due to the lower occupancy of messages. Therefore, they produce only a minor inefficiency in the computed mean values. However, most of the messages missing in real data are located mainly on entire columns. POL efficiencies used for the MC studies are used to check whether the columns, which are found to be defective, can be explained by low efficiencies of the optical links.

In a first approach, the distribution of real messages, shown in Fig. 5.11 (bottom), is studied. Empty columns are compared to the masking in the pad system, which can be seen in Fig. 5.10. Several columns, which contain no messages, and which do not match the masking in MU3, can be found. These columns are 9, 12 and 66, in the $+y$ half of the detector, and 42 and 66, in the $-y$ half. By checking the link efficiencies, it was found, that the efficiencies of the corresponding links are also zero. Therefore, it can be concluded, that the zero efficiencies of the pretrigger channels are caused by non-functioning optical links. These columns appear empty also in the case of Run 20582, suggesting that this problem was constant in time, and not an isolated incident.

A second check refers to the channels, in which a lower efficiency can be noticed. In the $+y$ half, columns 18 and 19, with pad efficiencies between 0.75 and 0.9 can be observed in the efficiency distribution, as well as in the distribution of lost messages in real data. The corresponding efficiencies in the POLs were also found to be smaller

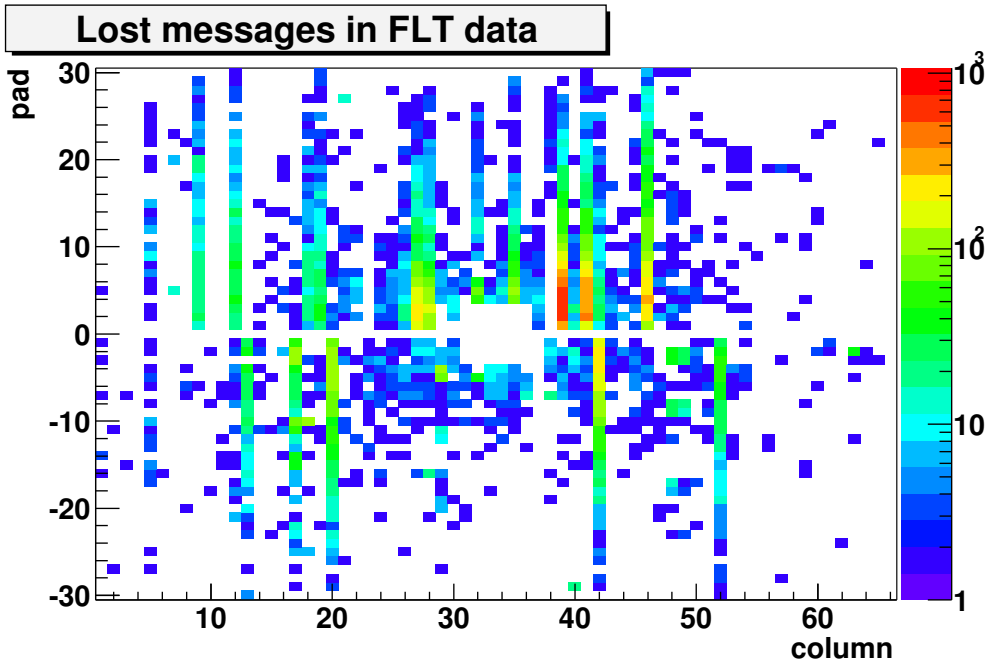

Figure 5.14: Distribution of simulated messages, which do not appear in real data, in Run 21012.

(0.92–0.95). Three columns, 26, 27 and 28, can be found in the latter distribution, but not in the former. This is due to the fact, that, while there are events containing less real messages than simulated ones, there are also a comparable number of events, in which the real messages are in excess. Overall they are compensated, so no inefficiencies can be noticed. A more detailed discussion regarding this aspect is presented in Section 5.6.2. Three additional low efficiency columns can be observed here, columns 39 and 41, with a pad efficiency ranging between 0.45 and 0.74, and column 46, with an efficiency less than 0.35. The first two columns have also lower POL efficiencies (0.77 to 0.80).

In the $-y$ half, columns 13, 17 and 20, were found in the two analyzed distributions, with efficiencies between 0.3 and 0.8. Only for the last column, the expected POL efficiency is lower (about 0.83). For the other two columns, the POL efficiencies were not much smaller than 1. This might be explained by the fact, that the link efficiencies are computed over a large time interval.

A list with all the columns mentioned above is given in Appendix C, together with the optical links, which showed inefficiencies in the pretrigger.

5.6.2 Influence of Channels with Efficiencies Larger than One for Run 21012

The same analysis of the influence of channels having efficiencies larger than 1 has been performed for Run 20582. The distribution of real pretrigger messages, which do not have a corresponding simulated message, is shown in Fig. 5.15.

Just as in the case of Run 20582, the first eight columns in the $-y$ half, can be noticed. But they do not affect the efficiency computation, since they are excluded by the cut of low occupancy channels ($N_{Sim} > 10$).

Another case is that of several columns in the $+y$ half, which have a larger number

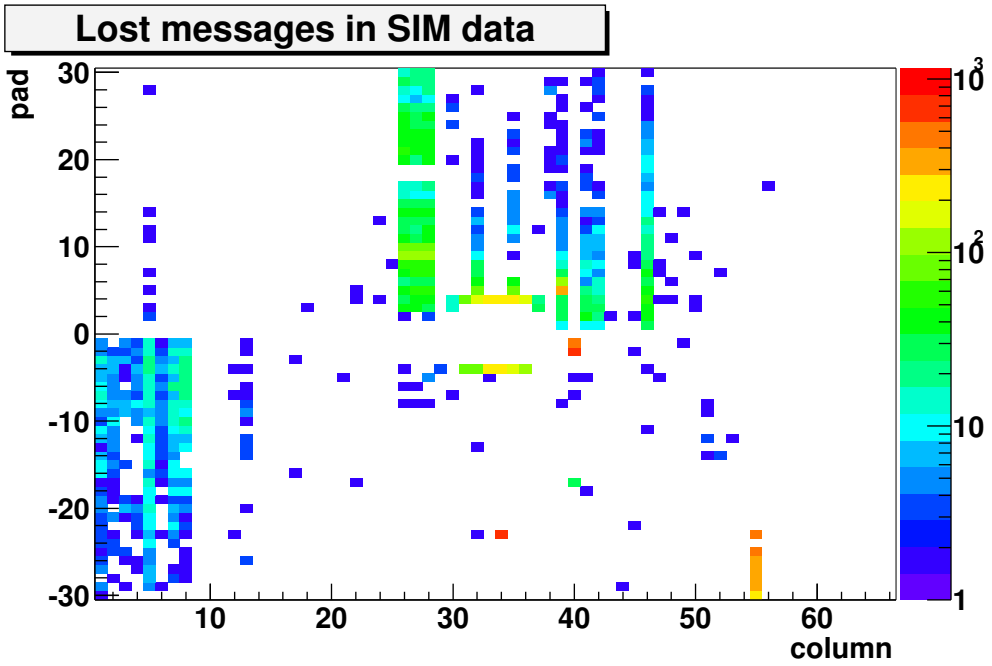

Figure 5.15: Distribution of messages, which do not appear in simulated data in Run 21012.

of real mesages than in the simulation results. These columns are 26, 27, 28, 32, 35, 39, 41, 42 and 46. The efficiency was recalculated, in order to study their influence. For several columns the efficiency was observed to decrease (e.g. for column 46, from about 0.25 to 0.15, and for columns 32 and 35 from about 0.95 to 0.9). The obtained values for the three computed mean efficiencies are given in Table 5.11. Comparing with the initial values, the new results are smaller, but still comparable within the uncertainties (e.g. by 0.003 smaller for $\overline{\varepsilon}$).

Table 5.11: Mean values of the pretrigger efficiency for Run 21012 without influence of channels having efficiencies larger than 1. The three different means were computed according to (5.5), (5.11) and (5.13).

Mean	Mean value of the efficiency
$\overline{\varepsilon}$	0.960 ± 0.002
$\overline{\overline{\varepsilon}}$	0.998 ± 0.002
$\overline{\varepsilon}_{J/\psi}$	0.967 ± 0.002

The number of channels having certain minimum efficiencies has also been recalculated, and is given in Table 5.12. These values are smaller than the originally computed ones (e.g. by 2.6% for the number of channels with efficiencies over 0.999).

5.7 Results for Run 21013

The trigger setup used for recording Run 21013 was the "interaction trigger", and the interaction rate was set at 4.86 MHz. The masking, which has been used for this run, is the same as that in Run 21012, since both runs were recorded in the same time period.

Table 5.12: Number of channels with efficiencies above a certain threshold for Run 21012, without influence of channels having efficiencies larger than 1. The number of channels, used in computing the ratio, was the total number of channels, which were considered for the efficiency study (i.e. 2151).

Efficiency larger than	No. of channels in absolute value	No. of channels in %
0.5	2106	97.9
0.9	1962	91.2
0.95	1864	86.6
0.99	1654	76.9
0.999	1268	58.9

It can be seen in Fig. 5.10. The number of channels covered by the masking is given in Table 5.8.

The same procedures as in the case of Run 20582 and Run 21012 were used. After all the cuts have been applied, the distributions of the real and simulated messages in the pad system were obtained. They can be seen in Fig. 5.16. The efficiency distribution can also be seen in Fig. 5.17.

The mean values of the $\overline{\varepsilon}$, $\overline{\overline{\varepsilon}}$ and $\overline{\varepsilon}_{J/\psi}$ were also computed and can be found in Table 5.13. The obtained values are larger than those computed for the previous runs ($\overline{\varepsilon}$ is larger than the value computed for Run 20582 by 0.012, and $\overline{\varepsilon}_{J/\psi}$ by 0.014). This can be explained by the much larger statistics of this run. The message occupancy is by a factor 2 larger. Therefore, the cut of low occupancy channels ($N_{Sim} > 0$) affects a much smaller number of channels than in the other two runs. For Run 21013, over 25% more pretrigger channels could be used for the efficiency study.

Table 5.13: Mean values of the pretrigger efficiency for Run 21013. The arithmetic mean $\overline{\varepsilon}$ is computed using (5.5). The mean weighted according to the uncertainty distribution $\overline{\overline{\varepsilon}}$ is calculated from (5.11). The mean weighted with respect to the hit distribution $\overline{\varepsilon}_{J/\psi}$ is given by (5.13).

Mean	Mean value of the efficiency
$\overline{\varepsilon}$	0.979 ± 0.002
$\overline{\overline{\varepsilon}}$	0.998 ± 0.002
$\overline{\varepsilon}_{J/\psi}$	0.979 ± 0.002

The distribution of channels, which have certain lower efficiency limits, has also been computed and is given in Table 5.14.

The efficiency distribution in the pad system can be seen in Fig. 5.18.

5.7.1 Influence of the Optical Links on the Efficiency for Run 21013

Low pretrigger efficiency channels can be studied using the distribution of lost messages in real data, which is shown in Fig. 5.19. In this case, it can also be observed that the missing messages, which cause real electronics inefficiencies, have only a marginal

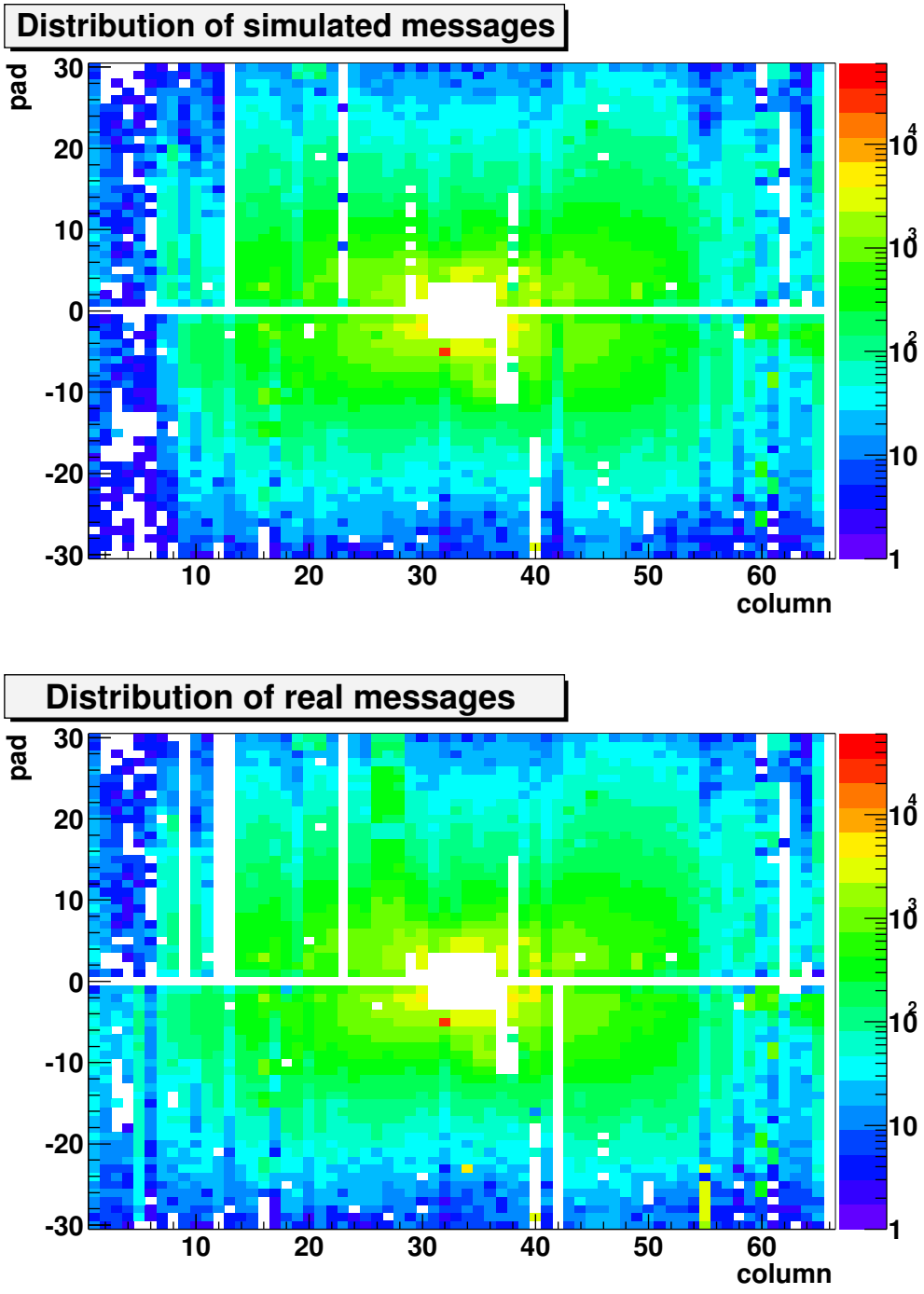

Figure 5.16: Distribution of messages in the muon pad system for Run 21013, in the case of simulated messages (top), and real messages (bottom).

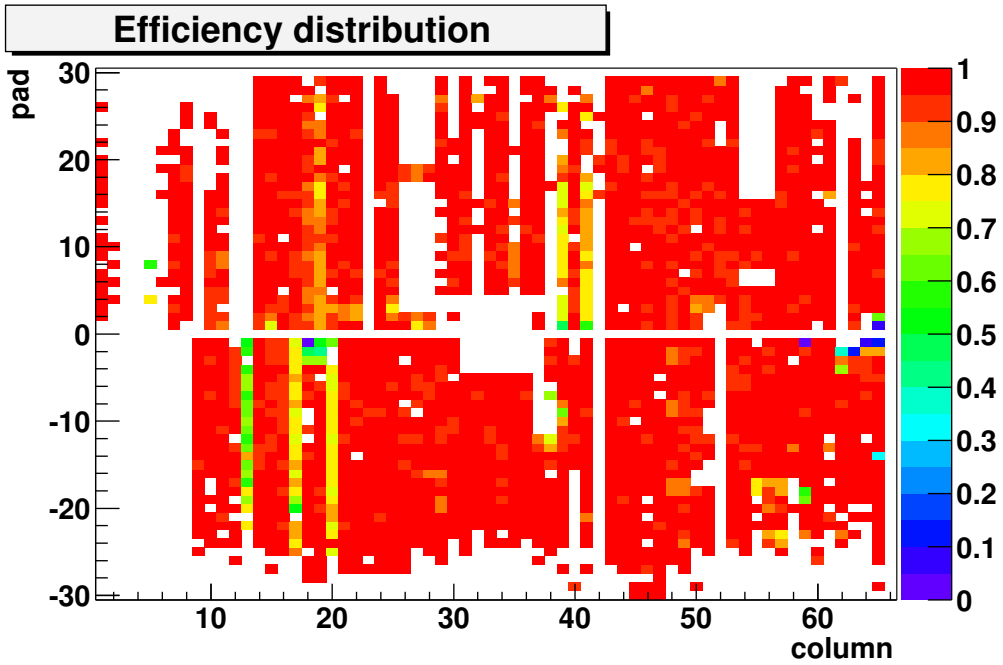

Figure 5.17: Efficiency distribution as a function of the column and pad numbers in Run 21013. The pads with efficiencies larger than 0.9 are displayed in red. Channels, in which less than 10 messages were observed, were disregarded, as well as channels with $N_{FLT} > N_{Sim}$.

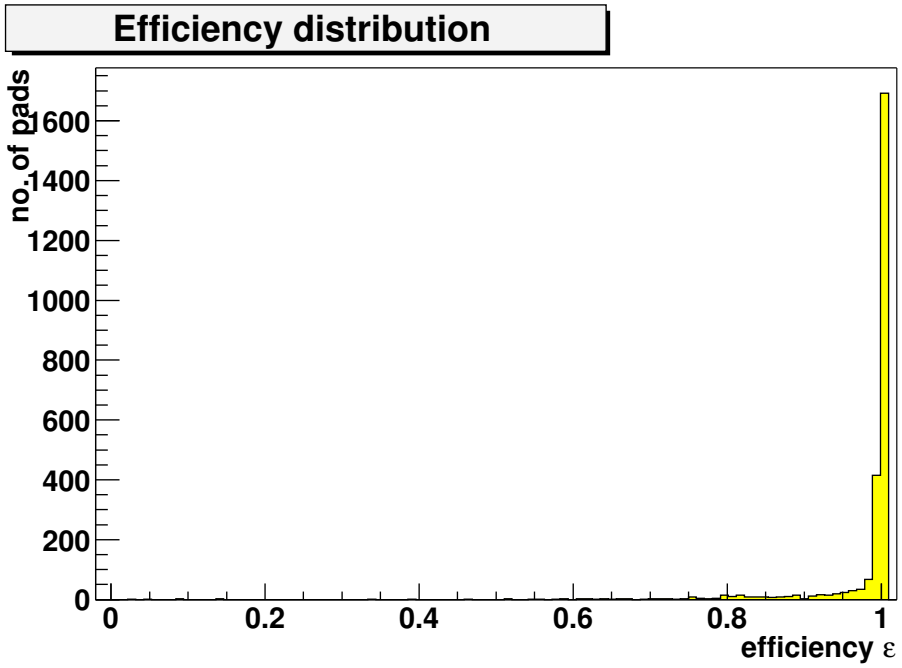

Figure 5.18: Distribution of the pad efficiencies for Run 21013.

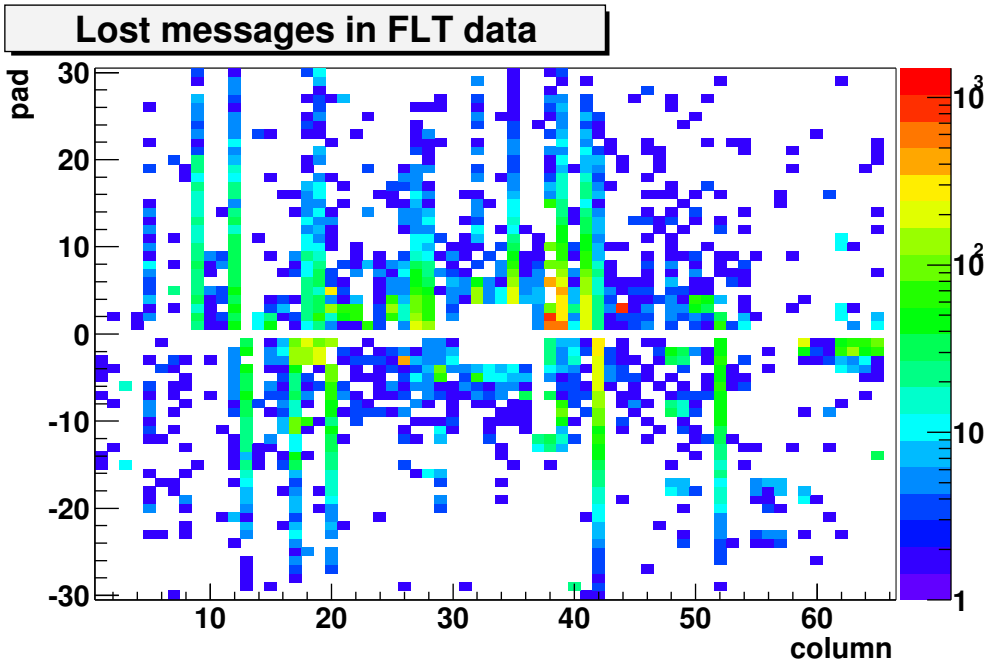

Figure 5.19: Distribution of simulated messages which do not appear in real data in Run 21013.

influence on the overall efficiency (i.e. they represent 0.005 from the overall efficiency). Most of the lost messages are also positioned on several columns, which correspond to low efficiency optical links. They are identical to the ones observed for Run 21012. This is expected, since the two runs were recorded in the same time period and the optical links are stable during this period. Both runs were recorded with the special setup for the pretrigger efficiency study. A detailed description of these low efficiency channels can be found in Section 5.6.1.

Table 5.14: Number of channels with efficiencies above a certain threshold for Run 21013. Several lower limits for the efficiency have been chosen. The number of channels, used in computing the ratio, was the total number of channels which were considered for the efficiency study (i.e. 2490).

Efficiency larger than	No. of channels in absolute value	No. of channels in %
0.5	2481	99.6
0.9	2322	93.2
0.95	2254	90.5
0.99	2096	84.1
0.999	1713	68.8

5.7.2 Influence of Channels with Efficiencies Larger than One for Run 21013

The distribution of messages, which appear in real data but are missing in the simulation, is given in Fig. 5.20. In the case of Run 21013, it was observed, that these mesages are again associated to several columns. They are identical to the ones in Run 21012. All these columns have been presented in detail in Section 5.6.2.

In order to determine their influence on the overall efficiency, the computations were repeated, after eliminating the messages in real data, which do not match the ones in simulation. The results for the efficiency are given in Table 5.15. As expected, the new values are smaller than the initial ones, but the difference is only marginal (i.e. $\overline{\varepsilon}$ is smaller by 0.003, and $\overline{\varepsilon}_{J/\psi}$ by 0.004).

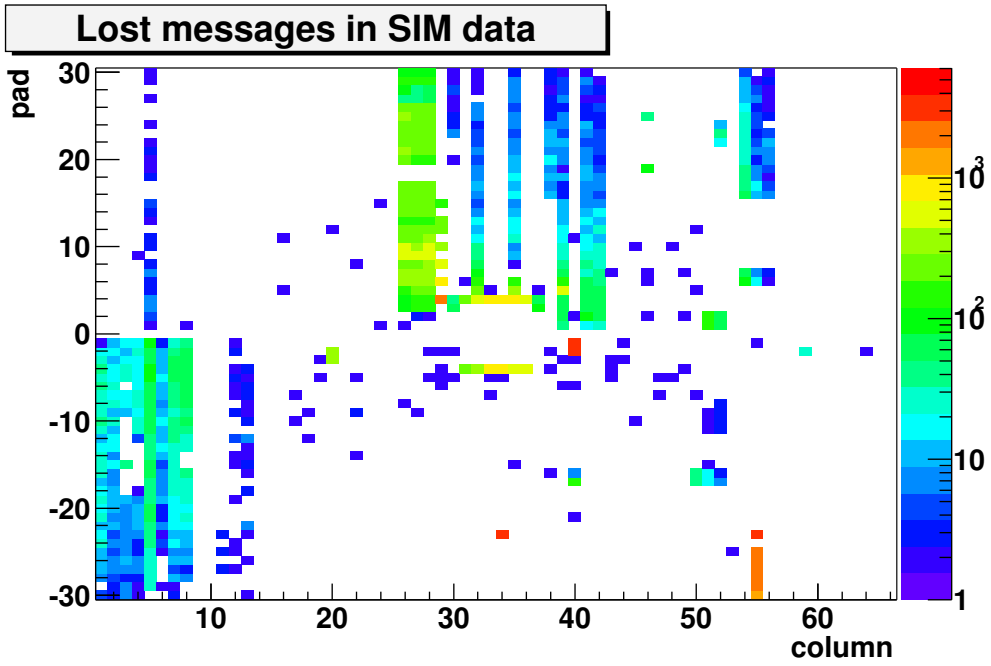

Figure 5.20: Distribution of messages which do not appear in simulated data in Run 21013.

The numbers of channels in given efficiency intervals were also recomputed, and can be found in Table 5.16. The percentage of channels is also smaller in this case, e.g. by 4.1% for the channels with efficiencies larger than 0.99, and by 3.6% for channels with

Table 5.15: Mean values of the pretrigger efficiency for Run 21013 without influence of channels having efficiencies larger than 1. The three different means were computed according to (5.5), (5.11) and (5.13).

Mean	Mean value of the efficiency
$\overline{\varepsilon}$	0.976 ± 0.002
$\overline{\overline{\varepsilon}}$	0.998 ± 0.002
$\overline{\varepsilon}_{J/\psi}$	0.975 ± 0.002

Table 5.16: Number of channels with efficiencies above a certain threshold for Run 21013, without the influence of channels having efficiencies larger than 1. The number of channels, used in computing the ratio, was the total number of channels, which were considered for the efficiency study (i.e. 2778).

Efficiency larger than	No. of channels in absolute value	No. of channels in %
0.5	2763	99.4
0.9	2580	92.9
0.95	2467	88.8
0.99	2240	80.6
0.999	1812	65.2

efficiencies larger than 0.999.

5.8 Comparison of the Pretrigger Efficiencies for all Three Data Samples

Having studied the performance of the muon pretrigger system for three different runs, recorded at two different dates (December 2002 and January 2002), with two trigger setups ("muon efficiency" and "interaction trigger" modes), it is possible to compare the results obtained for each run. In this way the stability of the pretrigger system can be investigated for the entire 2002/2003 data taking period. The results were also compared to the values obtained for the efficiency study realized for the 2000 data.

First, a comparison of the values for the mean efficiency in each case can be made. All these values for all three runs can be found in Table 5.17. The results are compatible within the uncertainties.

Table 5.17: Mean values of the pretrigger efficiency for all data samples and for Run 1704x (Run 17042 and Run 17044) from the data recorded in 2000.

Mean	Mean value of the efficiency			
	Run 20582	Run 21012	Run 21013	Run 1704x
$\overline{\varepsilon}$	0.965 ± 0.002	0.960 ± 0.002	0.979 ± 0.002	0.976 ± 0.003
$\overline{\overline{\varepsilon}}$	0.999 ± 0.002	0.998 ± 0.002	0.998 ± 0.002	0.998 ± 0.001
$\overline{\varepsilon}_{J/\psi}$	0.965 ± 0.002	0.967 ± 0.002	0.979 ± 0.002	0.975 ± 0.001

The percentage of channels, which have a minimum chosen efficiency, corresponding to the runs analyzed in this study as well as to Run 1704x from the 2000 data, can be seen in Table 5.18. The results are in agreement. In the 2002/2003 run, the number of channels having an efficiency larger than 0.999 is by about 20% larger than in the 2000 data, suggesting that the system was more stable.

The inefficiencies can be factorized into two components. The first is caused by real inefficiencies in the pretrigger electronics, and they have only a marginal influence on the mean value of the efficiency. The other is caused by the pretrigger optical links. They are the main factor, which determines the inefficiency of the system. The POLs are not very stable over larger time periods. In the cases of Run 21012 and Run 21013 (recorded in January 2003) more optical links were found to be unstable than in Run

Table 5.18: Number of channels with efficiencies above a certain threshold for all analyzed data samples, as well as for Run 1704x.

Efficiency larger than	No. of channels in % Run 20582	Run 21012	Run 21013	Run 1704x
0.5	98.6	97.9	99.4	97.7
0.9	90.2	91.2	92.9	91.8
0.95	86.6	86.6	88.8	86.0
0.99	82.0	76.9	80.6	55.3
0.999	73.6	58.9	65.2	42.9

20583 (recorded in December 2002), consequently their overall efficiencies were smaller. The number of channels having a certain efficiency is smaller in the case of the first two runs. For an efficiency larger than 0.999, the number of channels found for Run 20582 is 73.6%, compared to 68.8% for Run 21013, and only 58.9% for Run 21012.

5.9 Concluding Remarks

In this chapter, the efficiency of the muon pretrigger system has been investigated for the data recorded in the HERA-B 2002/2003 run. Three runs have been analyzed. They were recorded with a special trigger setup.

For each of the runs, values for the mean efficiencies have been computed. Also the distribution of the number of channels in intervals determined by a given minimum efficiency has been obtained.

Three problems have been discovered. The first two are sources of inefficiencies. There are real hardware inefficiencies, which have only a marginal influence on the overall result. In addition there are the inefficiencies caused by optical links, which are more important.

Another possible cause of errors are several channels where the number of real messages is larger than that of simulated messages. As this effect might cover some of the observed inefficiencies, the mean values of the efficiency had to be recomputed. Overall, the mean efficiency is estimated at 0.975, with over 65.2% of all channels included in the analysis, having an efficiency larger than 0.999. The results are also in agreement with values obtained for the 2000 data.

Chapter 6

Conclusions

In this thesis two studies have been performed, investigating the performances of the muon subdetector and of the muon pretrigger, during the HERA-B 2002/2003 data taking period.

For the determination of the quality of the data recorded by the muon subdetector, 294 runs were selected, from the runs accepted for physics analysis in HERA-B. A simple, but robust method was developed to count hot channels caused by defective readout electronics, and to determine their influence on the physics analysis.

An automatic procedure has been implemented, which analyzes every run and computes the number of hot channels in different components of the muon subdetector. Average values of the number of hot channels were determined for each case, and they were used for investigating the influence on the muon track reconstruction.

In the case of the muon tube chambers, the hit occupancies in each layer were checked. The number of hot channels was determined by approximating the shape of the distribution with a Gaussian distribution, and by counting the channels, which exceeded a certain threshold, compared to the fit function. The average values were computed for different time periods, corresponding to the periods between the access dates at the detector.

For the pad chambers a similar procedure was used to study the hit occupancies. In order to count the number of hot channels, the distributions were reweighted with a function to obtain a flat distribution. Mean values for the hot channels were computed using the median, which proved to be a robust method.

In order to study the influence of bad readout channels on the physics analysis, a Monte Carlo simulation was performed, in which "artificial" hot channels were implemented. The input data were hits in the muon tube and pad chambers. Additional hits were added in some of the channels to emulate the real distribution of hot channels. Then the influence on the number and quality of reconstructed muon tracks was determined resulting in no influence on the track multiplicity. Only when a very high proportion of the detector showed hot channels, a small influence could be observed.

The conclusion is, that hot channels, at the observed rate in the detector, do not cause fake muon tracks for physics analysis. This can be understood, since the reconstruction of a muon track requires hits also in the main tracker, and the hit information from the muon system is not sufficient. However, a number of runs were discovered, which should be excluded from the physics run list, due to various reasons. Several runs were recorded with a different trigger configuration than the one used for selecting events meaningful for the physics topics investigated in HERA-B. Another set of runs

which should be excluded is composed of runs, where either "missing quadrants" were observed, or the electron beam caused hits in the detector area.

In another study, the performance of the muon pretrigger system has been investigated for the data recorded in the HERA-B 2002/2003 run. The aim of the study is the determination of the efficiency of the pretrigger, as well as identifying defective components in the pretrigger hardware. For the analysis, three runs taken in two different run periods have been studied. These runs were recorded with a special setup of the trigger, which is unbiased by the muon pretrigger, such that the data is suitable for the efficiency investigation.

The pretrigger messages recorded for each run were compared with messages obtained from running MUPRESIM, a simulation program. The software describes the behavior of the pretrigger at the bit level. It uses as input raw data retrieved from the FED records, and performs a search for coincidences of muon hits in the pad system of the muon subdetector. The output are simulated pretrigger messages, which have the same data format as the real messages. A comparison between the two is possible.

The main concept for determining the efficiency of each pretrigger channel is the comparison of the total number of real messages to the total number of simulated messages belonging to a given pretrigger channel. The efficiency is determined as the ratio of the two numbers.

Two cases have been distinguished. The first case deals with channels having a low efficiency. The main source of inefficiencies are the pretrigger optical links, which are part of the pretrigger system. They show an unstable behavior, and some of them have an efficiency lower than 1. Since no reliable estimate of the optical link efficiencies is available from external sources, the efficiency could not be implemented in the simulation software. Hence, by detecting entire columns with smaller efficiency, a number of inefficient pretrigger optical links could be identified.

Another aspect of the efficiency analysis relates to the study of particular channels in which an efficiency larger than 1 could be observed. Low efficiencies in these channels are caused mainly by defective hardware components. Since the additional real messages can suppress inefficiencies, their influence on the efficiency computation has been studied, resulting only in a marginal decrease of the mean efficiency.

Finally, the pretrigger efficiencies were computed for all three runs, which were included in the analysis. The mean values of the efficiency have been computed in each case, as well as the distribution of channels according to their efficiency. The results are compatible with the results of a previous efficiency study for the 2000 data. A comparison between the values corresponding to each run was also done. As an overall conclusion, the pretrigger mean efficiency value is larger than 0.965 (including the channels with low link efficiencies). A high proportion of the pretrigger channels have a high efficiency, e.g. over 78% of all channels have efficiencies larger than 0.99, and over 61.5% show efficiencies larger than 0.999.

Appendix A

Plots used in the Data Quality Check of the Muon Subdetector

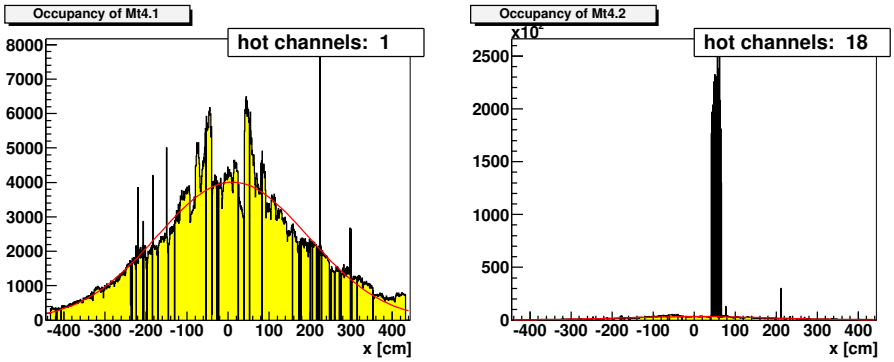

Figure A.1: Hit occupancy distributions in the two layers of MU4 as a function of the x position for Run 20527.

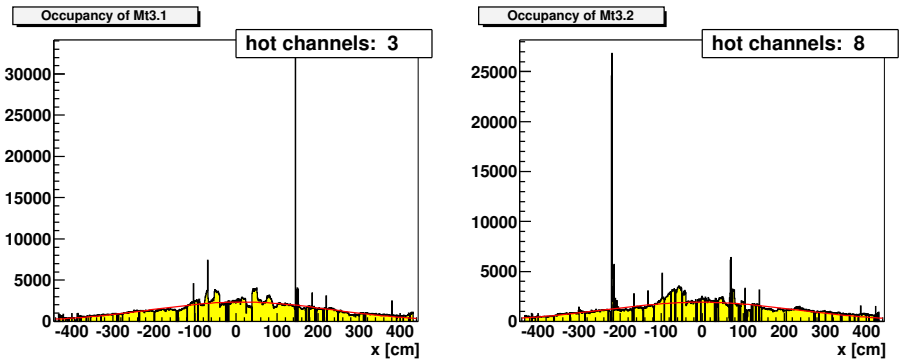

Figure A.2: Hit occupancy distributions in the two layers of MU3 as a function of the x position for Run 20527.

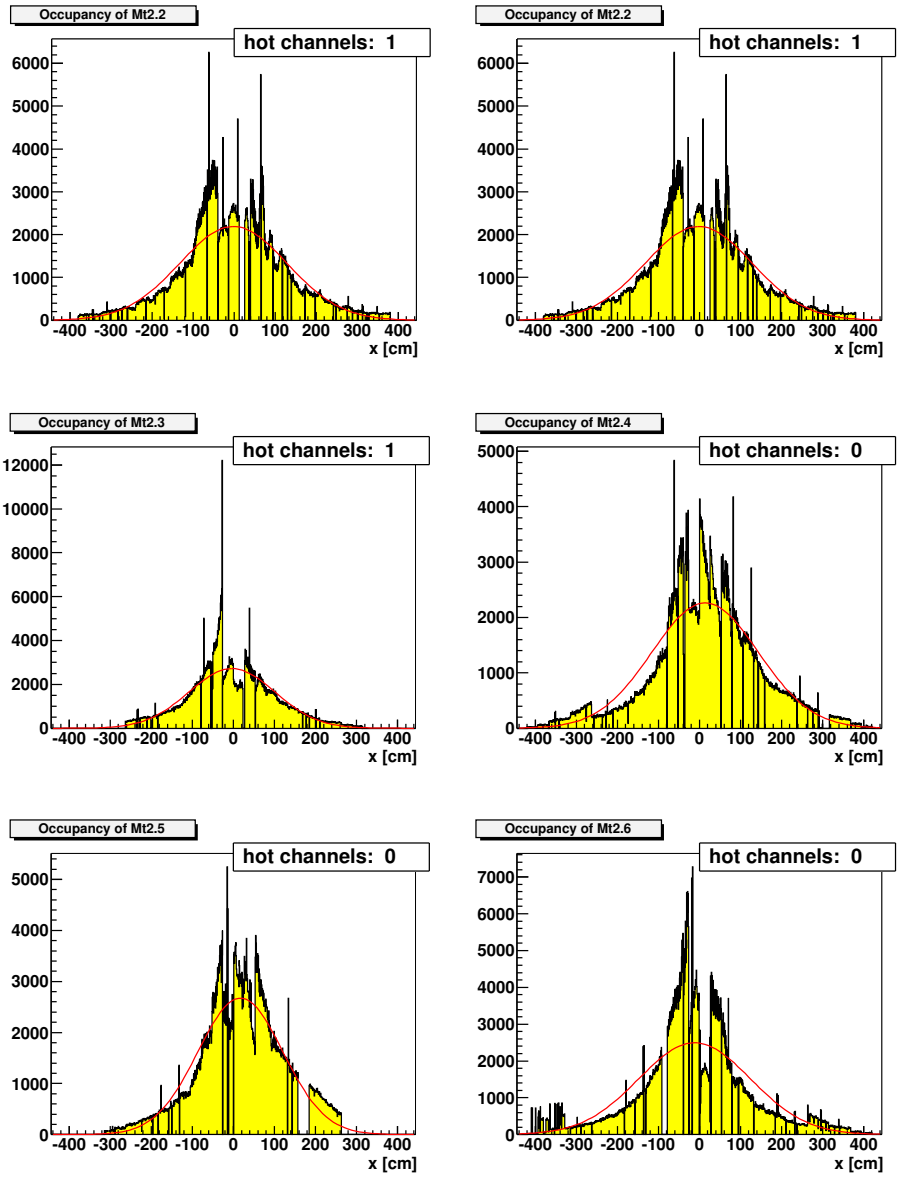

Figure A.3: Hit occupancy distributions in the six layers of MU2 as a function of the x position for Run 20527.

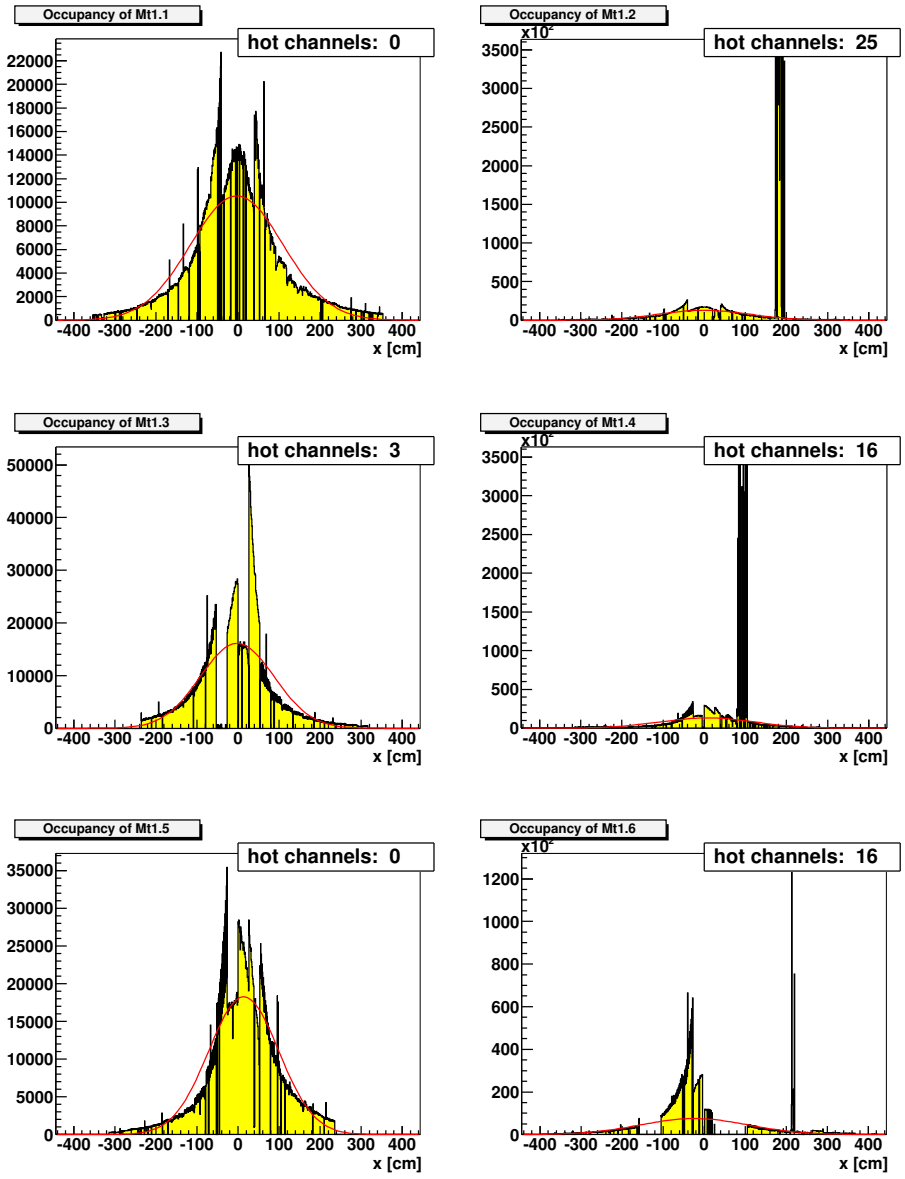

Figure A.4: Hit occupancy distributions in the six layers of MU1 as a function of the x position for Run 20527.

Appendix B

Hot Channels Used for the Track Multiplicity Study

In this section, the list of artificial hot channels used in the simulation of the influence of hot readout channels on track reconstruction is given. Table B.1 shows the hot columns corresponding to about 2% of the detector.

Table B.1: List of the artificial hot channels used in the simulation, corresponding to about 2% of the detector was made hot. This is compatible with the observed rate of hot channels in the detector. All artificial hot channels have an occupancy increased by a factor 10.

Muon layer	Channels made artificially hot
Mt1.1	Mt1.1-21 – Mt1.1-24
Mt1.2	Mt1.2.21 – Mt1.2-27
Mt1.3	–
Mt1.4	Mt1.4-16 – Mt1.6-18
Mt1.5	–
Mt1.6	–
Mt2.1	–
Mt2.2	–
Mt2.3	–
Mt2.4	–
Mt2.5	–
Mt2.6	–
Mp3.1	–
Mp3.2	Mt3.2-09
Mp4.1	–
Mp4.2	Mp4.2-08 – Mp4.2-10, Mp4.2-20 – Mp4.21

Table B.2 gives the list of hot channels corresponding to about 25% of the detector.

Table B.2: List of the artificial hot channels used in the simulation, correspondingto about 25% of the detector.

Muon layer	Channels made hot
Mt1.1	Mt1.1-21 – Mt1.1-24
Mt1.2	Mt1.2-10 – Mt1.2-27
Mt1.3	–
Mt1.4	Mt1.4-10 – Mt1.6-28
Mt1.5	Mt1.5-17
Mt1.6	Mt1.6-10 – Mt1.6.27
Mt2.1	–
Mt2.2	Mt2.2-10 – Mt2.2-28
Mt2.3	–
Mt2.4	Mt2.4-10 – Mt2.4-28
Mt2.5	–
Mt2.6	Mt2.6-10 – Mt2.6-28
Mp3.1	–
Mp3.2	Mp3.2-01, Mt3.2-10 – Mp3.2-27
Mp4.1	–
Mp4.2	Mp4.2-02, Mp4.2-10 – Mp4.2-27, Mp4.2-30

Appendix C

Channels with Low Efficiencies Observed in the Pretrigger Efficiency Study

In this appendix, the pad columns, in which a pretrigger efficiency lower than 0.9 was observed, are listed. In Table C.1 the low efficiency columns observed for Run 20582 are given, while in Table C.2 the low efficiency columns in Run 21012 and Run 21013 are presented.

Table C.1: List of low efficiency columns in the pad system for Run 20582. For each column, the corresponding defective optical link, if identified, is also given.

Pad column	Efficiency	Position	Optical link ID	optical link Efficiency
5	–	$+y$	3005	0.5
9	0	$+y$	3009	0.0
12	0	$+y$	3012	0.0
18	0.8–0.95	$+y$	3018	0.90
19	0.7–0.9	$+y$	3019	0.85
23	0	$+y$	–	–
32	0	$+y$	–	–
35	0.85–0.95	$+y$	3035	0.97
36	0.5–0.7	$+y$	3036	0.71
38	0	$+y$	–	–
39	0.6–0.8	$+y$	3039	0.78
41	0.6–0.8	$+y$	3041	0.83
42	0.85–0.95	$+y$	3042	0.98
56	–	$+y$	4122	0
66	0	$+y$	3066	0
5	–	$-y$	–	–
13	0.3–0.6	$-y$	–	–
16	0.75–.95	$-y$	4083	0.88
17	0.55–0.8	$-y$	4083	0.88
18	0.7–0.9	$-y$	4083	0.88
20	0.6–0.8	$-y$	3086	0.86
42	0	$-y$	3106	0
66	0	$-y$	3132	0

These channels have been identified by studying the efficiency distributions in the pad system and the distributions of simulated messages which do not match real pretrigger messages. Some of the channels can be identified only in the latter plots, since they were excluded by the low occupancy cut ($N_{Sim} > 10$). Therefore, the efficiencies of these channels have not been estimated.

The optical link efficiencies were determined in a separate study which used the same simulation software used to determine the link efficiencies. These values are used in Monte Carlo simulations. They are shown here only for cross-checking, if columns with lower pretrigger efficiency correspond to links well known for their unstable behavior.

Table C.2: List of low efficiency columns in the pad system for Run 21012 and Run 21013. For each column, the defective optical link, if identified, is also given.

Pad column	Efficiency	Position	Optical link ID	optical link Efficiency
9	0	$+y$	3009	0
12	0	$+y$	3012	0
18	0.8–0.95	$+y$	3018	0.95
19	0.75–0.9	$+y$	3019	0.92
26	–	$+y$	–	–
27	0.7–0.9	$+y$	–	–
28	0.85–0.95	$+y$	–	–
32	0.8–0.95	$+y$	–	–
35	0.8–0.95	$+y$	–	–
39	0.5–0.8	$+y$	3039	0.77
41	0.5–0.8	$+y$	3041	0.80
42	0.8–0.95	$+y$	–	–
46	0.1–0.4	$+y$	–	–
66	0	$+y$	3066	0
13	0.3–0.8	$-y$	–	–
17	0.55–0.8	$-y$	4082	0
20	0.5–0.8	$-y$	3086	0.83
42	0	$-y$	3108	0
66	0	$-y$	3132	0

List of Figures

List of Tables

Bibliography

[Ada99] M. Adams et al., *The Muon Pretrigger System of the HERA-B Experiment*, IEEE Trans. Nucl. Sci. **46** (1999), 1982–1988.

[Ada01a] M. Adams, *Entwicklung eines Simulationsprogrammes für das Myon-Pretrigger-System des HERA-B Expermentes und Untersuchungen zum Systemverhalten*, Ph.D. thesis, Universität Dortmund, 2001.

[Ada01b] M. Adams, *Muon pretrigger online software page*, 2001, `http://www.hep.physik.uni-siegen.de/herab/docs/mupresim/index.html` (retrieved: March, 2004).

[Ari04] I. Arino et al., *The HERA-B Ring Imaging Cherenkov Counter*, Nucl. Instrum. Meth. **A516** (2004), 445–461, hep-ex/0303012.

[Avo01] G. Avoni et al., *The Electromagnetic Calorimeter of the HERA-B Experiment*, Nucl. Instrum. Meth. **A461** (2001), 332–336.

[Bal02] V. Balagura et al., *The First-Level Trigger of the HERA-B Experiment: Performance and Expectations*, Nucl. Instrum. Meth. **A494** (2002), 526–534.

[Bau03] C. Bauer et al., *Performance of the HERA-B Vertex Detector System*, Nucl. Instrum. Meth. **A501** (2003), 39–48.

[Bea00] V. Balagura et al., *High-p_T Trigger for HERA-B Experiment*, Nucl. Instrum. Meth. **A453** (2000), 412–416.

[Boc00] R. K. Bock, H. Grote, D. Notz, M. Regler, and M. Regler, *Data Analysis Techniques for High-energy Physics Experiments*, Cambridge Monogr. Part. Phys. Nucl. Phys. Cosmol. **11** (2000), 1–434.

[Böc01] M. Böcker et al., *The Muon Pretrigger System of the HERA-B Experiment*, IEEE Trans. Nucl. Sci. **48** (2001), 1270–1275.

[Bru97] R. Brun and F. Rademakers, *ROOT: An Object Oriented Data Analysis Framework*, Nucl. Instrum. Meth. **A389** (1997), 81–86.

[Cow98] G. Cowan, *Statistical Data Analysis*, Oxford University Press, 1998.

[DES00] DESY, Abteilung Presse und Öffentlichkeitsarbeit, Hamburg, 2000.

[Ehr00] K. Ehret, *Commissioning of the HERA-B Internal Target: Using the HERA Proton Ring as a B-factory*, Nucl. Instrum. Meth. **A446** (2000), 190–198.

[Eig01] V. Eiges et al., *The Muon Detector at the HERA-B Experiment*, Nucl. Instrum. Meth. **A461** (2001), 104–106.

[Fla01] J. Flammer, *Entwicklung der Simulation des ECAL Pretrigger Systems für das Experiment HERA-B und Analyse der Effizienzen des Zerfalls* $J/\psi \rightarrow e^+e^-$, Ph.D. thesis, Universität Hamburg, 2001.

[Har99] R. Harr, *Muon Chamber and Channel Numbering*, HERA-B Note 99-117, DESY, Hamburg, 1999.

[HER03a] HERA-B, *Event Processing Software page: ARTE*, 2003, `http://www-hera-b.desy.de/subgroup/software/#ARTE` (retrieved: March, 2004).

[HER03b] HERA-B, *Online log book*, 2003, `http://www-hera-b.desy.de/htbin/herab/shift/slog/slog.pl` (retrieved: November, 2003).

[HER04a] HERA-B, *B-Bar working grop page*, 2004, `http://www.desy.de/~nedden/bbarruns_02.html` (retrieved: August, 2003).

[HER04b] HERA-B, *B-Bar working grop page*, 2004, `http://www.desy.de/~nedden/bbarruns_03.html` (retrieved: August, 2003).

[Hoh01] M. Hohlmann, *The Outer Tracker of HERA-B*, Nucl. Instrum. Meth. **A461** (2001), 21–24.

[Hus03] U. Husemann, Universität Siegen, private communication, December 2003.

[Hus04] U. Husemann, Universität Siegen, private communication, May 2004.

[Sch99] B. Schwenninger, *Mapping of Muon Pad Chambers to Pretrigger Coincidence Unit and Pretrigger Message Generator Channels*, 1999.

[Sch00] B. Schwenninger et al., *The Muon Pretrigger System of the HERA-B Experiment*, Proceedings of the Sixthh Workshop on Electronics for LHC Experiments, Cracow, Poland, 11-15 Sep 2000.

[Sch01] B. Schwenninger, *Das Myon-Pretrigger-System für das HERA-B Experiment*, Ph.D. thesis, Universität Dortmund, 2001.

[Spe02] J. Spengler, *HERA-B detector components*, 2002, `http://www-hera-b.desy.de/subgroup/detector/` (retrieved: February, 2004).

[Ste00] C. Stegmann (HERA-B Outer Tracker Group Collaboration), *The Outer Tracker for HERA-B*, Nucl. Instrum. Meth. **A453** (2000), 153–158.

[Tay97] J. R. Taylor, *An Introduction to Error Analysis*, University Science Books, 1997.

[Zeu00] T. Zeuner (HERA-B Collaboration), *The MSGC-GEM Inner Tracker for HERA-B*, Nucl. Instrum. Meth. **A446** (2000), 324–330.

Acknowledgement

First, I would like to thank Prof. Dr. Peter Buchholz for giving me the opportunity to work on a very interesting topic related to the HERA-B experiment. During the time that I worked in the group which he lead, I experienced both the feeling of hard work, as well as the great satisfaction of successfully accomplishing my tasks.

I would like to thank also Prof. Dr. Claus Grupen, for revising this thesis.

Special thanks to Ulrich Husemann, for guiding my steps during the analysis for this thesis, for sharing his expertise in technical details regarding the HERA-B experiment. Thanks also for always providing new ideas when no solutions seemed possible, for countless fruitful discussions and for all the new things which I have leared. And last, but not least, thanks for taking the time to revise this thesis and give useful suggestions.

I would like to thank all my friends and collegues from our group, for the nice time spent together and for their help whenever it was necessary, and especially: Victor George Andrei, Nadir Omar Hashim, Roxana Tomaida Lixandru, Florin Maciuc and Sven Over.

I would like to express my special thanks to Ewa Joanna Palusiak for showing me affection and encouraging me during the time spend working on this thesis.

Finally, I want to thank my mother Cleopatra Sipică and my sister Luciana Sipică for always showing me moral support and encouraging me, especially during the period of my studies in Siegen.

Erklärung

Erklärung

Hiermit erkläre ich, dass ich die vorliegende Masterarbeit selbständig verfasst und keine anderen als die angegebenen Quellen und Hilfsmittel benutzt, sowie Zitate und Ergebnisse Anderer kenntlich gemacht habe.

. . . .

(Ort) (Datum) (Unterschrift)